Analytical Modeling of a Novel Microdisk Resonator for Liquid-Phase Sensing: An All-Shear Interaction Device (ASID)

Mohamad Sadegh Sotoudegan
Marquette University

Recommended Citation
Sotoudegan, Mohamad Sadegh, "Analytical Modeling of a Novel Microdisk Resonator for Liquid-Phase Sensing: An All-Shear Interaction Device (ASID)" (2016). *Dissertations (2009 -)*. 666.
https://epublications.marquette.edu/dissertations_mu/666

ANALYTICAL MODELING OF A NOVEL MICRODISK RESONATOR FOR LIQUID-PHASE SENSING: AN ALL-SHEAR INTERACTION DEVICE (ASID)

by

Mohamad Sadegh Sotoudegan, B.S., M.S.

A Dissertation submitted to the Faculty of the Graduate School,
Marquette University,
in Partial Fulfillment of the Requirements for
the Degree of Doctor of Philosophy

Milwaukee, Wisconsin

August 2016

ABSTRACT

ANALYTICAL MODELING OF A NOVEL MICRODISK RESONATOR FOR LIQUID-PHASE SENSING: AN ALL-SHEAR INTERACTION DEVICE (ASID)

Mohamad Sadegh Sotoudegan, B.S., M.S.

Marquette University, 2016

Extensive research on micro/nanomechanical resonators has been performed recently due to their potential to serve as ultra-sensitive devices in chemical/biosensing. These applications often necessitate liquid-phase sensing, introducing significant fluid-induced inertia and energy dissipation that reduces the resonator’s performance.

To minimize the detrimental fluid effects on such devices, a novel microdisk resonator supported by two tangentially-oriented, axially-driven “legs” is investigated analytically and effects of the system parameters on the resonator/sensor performance are explored. Since the device surface vibrates primarily parallel to the fluid-structure interface, it is referred to here as an “all-shear interaction device,” or ASID.

Analytical modeling of the ASID includes a single-degree-of-freedom model, in which the leg mass and associated fluid resistance are neglected relative to their disk counterparts, and a generalized continuous-system, multi-modal model, in which inertial and fluid effects are included for the entire structure. The resulting analytical formulae along with the parametric studies predict that ASID designs with slender legs yield a global maximum in the quality factor (Q_{max}) at a “critical” disk radius approximately twice the device thickness, whereas stiffer legs correspond to Q_{max} occurring for the axial-mode microcantilever (the no-disk limit of the ASID). Additionally, the highest mass and chemical sensitivities $\left(S_m,\ S_c\right)$ and lowest mass limit of detection $\left(LOD_m\right)$ of an ASID-based sensor correspond to the axial-mode microcantilever limit, whereas the chemical LOD $\left(LOD_c\right)$ has a relative minimum at the critical disk size; thus, the “optimal-Q” disk size may be different than the “optimal-sensing” counterpart. The results also show that utilizing stiffer legs will improve Q, S_m, S_c, LOD_m, and LOD_c.

The theoretical results show both qualitative and quantitative agreement with existing experimental data on liquid-phase quality factor in heptane and in water, while the corresponding theoretical predictions for the fluid-induced resonant frequency shift (typically < 1%) indicate the effectiveness of this novel design. Moreover, the results suggest that appropriately designed ASIDs are capable of achieving unprecedented levels of liquid-phase quality factor in the 300-500 range or even higher. The new theoretical formulae also enable one to easily map experimental data on ASID performance in one liquid to behaviors in other media without performing additional experiments.

ACKNOWLEDGMENTS

Mohamad Sadegh Sotoudegan, B.S., M.S.

There are many individuals who have guided, supported and encouraged me along the way, without whom this dissertation would never have been made possible. I would like to specifically recognize and thank those who have been instrumental in the completion of this work.

First of all, I would like to thank the National Science Foundation (Grant ECCS-1128992 and Grant ECCS-1128554), the Marquette University Graduate School, and Marquette's Department of Civil, Construction and Environmental Engineering for the significant financial support they provided to carry out this dissertation research.

I would like to extend a special thank you to my advisor, Dr. Stephen M. Heinrich, for his guidance, patience, and encouragement throughout my graduate career. Dr. Heinrich's knowledge, dedication, enthusiasm, and integrity are truly remarkable and inspirational, and I am very proud to call him my mentor and fellow researcher.

I would also like to thank the members of our research group consisting of Dr. Fabien Josse, Dr. Isabelle Dufour, Dr. Oliver Brand, Dr. Chung Hoon Lee, and Dr. Nicholas Nigro (who has been and will always be missed) for sharing their knowledge and expertise from various technical areas along the way. It has been an amazing opportunity to collaborate with and learn from such a diverse group of researchers, teachers and students who have positively influenced my academic life to grow both as a researcher and as a student.

Finally, I must thank my family and friends whose continual support and encouragement always helped keep me focused and motivated whenever I felt discouraged. I am forever grateful to them.

TABLE OF CONTENTS

NOMENCLATURE

Symbols

A = cross-sectional area of legs

a = disk radius

$\bar{a} \equiv a/h$ = normalized disk radius

b = leg width

$\bar{b} \equiv b/h$ = normalized leg width

c_A = analyte concentration in ambient

c_2 = analyte concentration in coating layer (at chemical equilibrium)

$\bar{\bar{c}}_f$ = effective fluid damping coefficient per unit area

d = damping ratio

E = Young’s modulus of ASID resonator (base) material

E_{eff} = effective Young’s modulus of bi-layer ASID sensor

F = axial force at disk-leg junction

f_{res} = resonant frequency of the ASID (Hz)

h = ASID thickness

$h_1,\ h_2$ = base layer and coating thicknesses, resp., for a bi-layer ASID sensor

$h_{eff} \equiv h_1 + h_2$ = effective thickness of the bi-layer ASID sensor

I = second moment of area of the leg cross section

J = polar moment of inertia of the disk

$K \equiv c_2/c_A$ = partition coefficient of the analyte/coating pair (in gas or liquid)

L = leg length

$\bar{L} \equiv L/h$ = normalized leg length

$L_0 \equiv \sqrt{\dfrac{{\rho_f}^2\eta^2}{\rho^3 E}}$ = characteristic “material length”

$\bar{L}_0 \equiv L_0/h$ = normalized characteristic material length

LOD_m = mass limit of detection

LOD_c = chemical limit of detection

M = bending moment at disk-leg junction

m = total mass of the bi-layer ASID sensor

m_2 = total coating mass

$\bar{\bar{m}}_f$ = effective fluid mass coefficient per unit area

n = mode number

Q = quality factor

S_m = mass sensitivity

S_c = chemical sensitivity

T_{T+B} = fluid resistance torque on combined top and bottom surfaces of disk

T_L = fluid resistance torque on lateral surface of disk

t = time coordinate

$\bar{t} \equiv \omega_0 t$ = dimensionless time coordinate

$\bar{U}(\xi)$ = axial vibration amplitude in the leg

$u(x,t)$ = axial displacement in legs

$\bar{u}(\xi,\bar{t}) \equiv u/L$ = normalized axial displacement in legs

V_{eff} = volume of the ASID sensor

V_2 = volume of the coating

x = longitudinal coordinate

$\alpha \equiv \frac{a^2}{bL}$, $\bar{\alpha} \equiv \frac{\pi}{4}\alpha$ = normalized disk areas

$\beta \equiv \frac{2}{\sqrt{\pi}}\left(1+\frac{1}{\bar{b}}\right)\sqrt{\bar{L}_0 \bar{L}}$ = fluid resistance parameter for the continuous model

$\Delta \equiv \frac{1+2h/a}{1+h/b}$ = non-dimensional geometric parameter

δ = decay parameter

$\bar{\delta} = \delta / \omega_0$ = normalized decay parameter

δ_{axial} = static axial deflection of the leg end

$\delta_{trans.}$ = static transverse deflection of the leg end

$\varepsilon^*\left(\bar{t}\right)$ = externally applied harmonic eigenstrain in the legs

ε_0 = eigenstrain amplitude

$\zeta \equiv \left(1+\frac{1}{\bar{a}}\right)\sqrt{\bar{L}_0 \bar{L}}$ = fluid resistance parameter for the SDOF model

η = dynamic viscosity of the fluid

$\theta\left(\bar{t}\right)$ = total angle of disk rotation

θ_0 = disk rotation amplitude

$\bar{\theta}\left(\bar{t}\right) \equiv \frac{\theta(\bar{t})}{\varepsilon_0 L / a}$ = normalized disk rotation signal

$\xi \equiv x/L$ = dimensionless longitudinal coordinate

ρ = mass density of ASID material

ρ_1, ρ_2 = mass densities of the base layer and coating, resp., for bi-layer ASID sensor

$\rho_{eff} = \dfrac{\rho_1 h_1 + \rho_2 h_2}{h_1 + h_2}$ = effective (average) mass density of bi-layer ASID sensor

ρ_f = mass density of fluid

$\sigma(x,t)$ = axial stress in legs

τ = shear stress exerted by fluid on contacting surface

ϕ = phase shift

$\Omega = \omega + i\delta$ = complex natural frequency

$\omega_0 \equiv \dfrac{\pi}{2L}\sqrt{\dfrac{E}{\rho}}$ = in-vacuum fundamental axial frequency of an isolated leg (cantilever)

ω_{vac} = in-vacuum natural frequency

$\bar{\omega}_{vac} \equiv \omega_{vac} / \omega_0$ = normalized in-vacuum natural frequency

$\bar{\omega} \equiv \omega / \omega_0$ = normalized in-fluid natural frequency or frequency of excitation/steady-state response

CHAPTER 1:

INTRODUCTION

1.1. Microelectromechanical Systems (MEMS): History and Applications

The field of microelectromechanical systems (MEMS) encompasses the techniques and processes used to design and create miniaturized integrated devices or systems with embedded mechanical or electromechanical elements that integrate functionalities from different physical domains into one package. These systems have the ability to “merge the functions of sensing and actuation with computation and communication to locally control physical parameters at the microscale, yet cause effects at much grander scales.” [1] A brief history of MEMS technology illustrates its diversity, applications, and challenges that researchers have encountered and in many cases overcome in the past decades. According to Bogue [2], the origins of MEMS technology may arguably be traced back to 1954, when a paper by Smith [3] was published in the *Journal of Physical Review* in which the author described for the first time certain stress-sensitive effects in silicon and germanium, called piezoresistance. In 1957 Mason and Thurston [4] first reported silicon strain gauges for measuring displacement, force, and torque. These semiconductor strain gauges, with much higher sensitivity than conventional metal strain gauges, were considered a leap forward in sensing technology. At the annual meeting of the American Physical Society in 1959, Richard Feynman gave a keynote presentation at Caltech, entitled “There’s Plenty of Room at the Bottom,” a lecture that popularized the growth of micro and eventually nano technology. In his talk, Feynman issued a public challenge by offering $1000 to the first person to create a rotating electrical motor that can be controlled from outside and is only 1/64th of an inch in dimensions [5]. Following the early successes in physical sensing and the dramatic growing interest in silicon-based microscale sensor technology since then, the research community turned its attention toward the use of silicon technology in both gas- and liquid-phase sensing. The invention and development of atomic force microscopy (AFM) by IBM scientists in 1986 [6] was a milestone in this context. AFM maps the surface of an atomic structure by measuring the force acting on the tip (probe) of a microcantilever or by using the shift in frequency of the device that interacts with a sample. AFM microcantilevers usually made of silicon or silicon nitride were found to be sensitive (through observation of their deflection) to temperature, ambient humidity, and chemical vapor adsorption [7]. Coated micromachined resonators such as beams, cantilevers, and resonator arrays have since been fabricated from silicon for a wide range of applications, including chemical sensing in gas or liquid environments. These resonators can be extremely sensitive due to their small mass, since small amounts of sorbed mass (analyte) from the surroundings may cause a measurable shift in the device's resonant frequency. Varying degrees of partial selectivity can be achieved through the use of appropriate coatings (generally polymers) on the resonating device. MEMS resonators have attracted growing attention among scientists in recent years and novel sensing applications have been developed for such devices. Some have been developed to meet the demanding needs of, for example, the automotive industry (such as inertial MEMS sensors in airbags or gas sensors that detect and monitor certain gasses or unburned fuel in the vehicle exhaust system), monitoring indoor air quality by employing gas sensors that detect volatile organic compounds (toxic vapors at room temperature) in the workplace, or used in medical applications such as robotic surgery or medical implants, to name a few. The complex and interdisciplinary nature of MEMS today that is reflected in a broad spectrum of applications ranging from consumer electronics and automotive to medical, communications, and defense, relies on design, engineering and fabrication expertise from a wide range of technical areas. These include various fields of engineering, materials science, chemistry, biology, as well as solid and fluid mechanics, optics, and instrumentation. With the development and constant rise in the use of MEMS pressure sensors and accelerometers, the emergence of MEMS microphones and the massive use of these technologies today (e.g., in smartphones) [8], the novel use of microcantilever-based resonators as energy harvesters that convert the low level ambient vibrations into useful electrical power [9-13], and steady progress in gas- and liquid-phase chemical sensors and bio-MEMS [14-20], the investigation and applications of these devices continue to expand.

1.2. Motivation and Objectives of the Present Study

The evolution of MEMS technology has not only been outstandingly successful in creating high-performance devices, but it has also challenged engineers and scientists with the obstacles that often arise with MEMS devices of new designs and/or harsh environments in which they are required to operate. For example, miniaturization of MEMS sensors makes them extremely sensitive to thermal noise; therefore they have to be either massive enough or stiff enough to not be unduly influenced by the ambient [21]. Another example may be found in the case of microfluidics and bioMEMS, where blockage of microchannels has been observed due to liquid contamination or large biological samples [22]. In particular, investigations on liquid-phase MEMS resonators have been of research interest for years as they span a broad spectrum of applications today. Chemical sensing is one of the practical areas of sensing technology in which the resonator is (partially or fully) immersed in a viscous fluid medium (gas or liquid) to detect certain target substances or chemicals that are sorbed into/onto the device. Since many of these applications require the device to operate in a viscous fluid environment, the focus has been on reducing the detrimental (inertial and viscous) effects of the surrounding fluid on the performance of the device. In order to minimize such undesirable effects on the sensing and resonator performance of devices of more conventional designs, researchers have explored the use of unconventional vibration modes or alternative designs of the device as will be discussed in the literature review in Ch. 2.

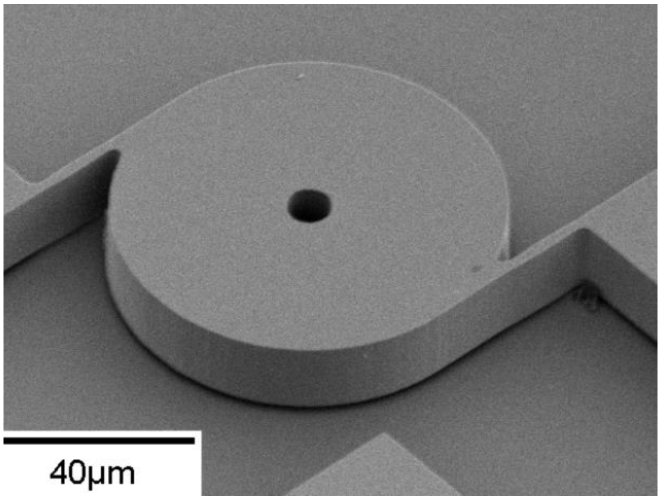

Fig. 1-1. Silicon-based MEMS microdisk resonator [23]

The present research deals with a particular MEMS resonator of a novel design: a disk-type device that oscillates in a viscous fluid environment. Such a device was introduced by Rahafrooz and Pourkamali [23, 24], who fabricated and tested their novel design to demonstrate unprecedented levels of quality factor (a performance metric that indicates how efficiently a damped dynamic system resonates) in a viscous liquid (Fig. 1-1). However, their results were limited to experimental data and finite element analysis (FEA) only, hence lacking a strong theoretical basis for the encouraging device performance. Therefore, the present work will include (a) detailed derivations of explicit analytical formulae for relating the resonator and sensing performance metrics of the system to the device's design parameters and the fluid properties; (b) a detailed parametric study of the device performance, in terms of both resonant characteristics and mass-sensing metrics; (c) recommendations for obtaining improved and optimal designs; and (d) validation of the analytical models using three-dimensional numerical (FEA) simulations and experimental data.

1.3. Problem Statement

A detailed analytical model of the micromechanical disk resonator (Fig. 1-1) operating in a viscous fluid is executed in this research. As noted earlier, the device consists of a central microdisk structure that is supported by two tangentially-oriented legs that are axially excited (e.g., through electrothermal actuation). Periodic axial strains in the legs, applied in an in-phase manner with one another, result in an in-plane rotational oscillation of the disk as shown in Fig. 1-2. This device is expected to exhibit potential advantages over liquid-phase MEMS devices of more conventional designs/vibration modes as it engages the surrounding viscous fluid through shearing action only, i.e., the device surface vibrates primarily parallel to the fluid-structure interface; hence we shall refer to such a device as an “all-shear interaction device” or

"ASID." The ASID concept enhances the performance of the resonator by reducing the fluid effects as the main source of energy dissipation in the system. The potentially large functionalized area afforded by the disk is another potential advantage of the ASID in liquid-phase sensing applications.

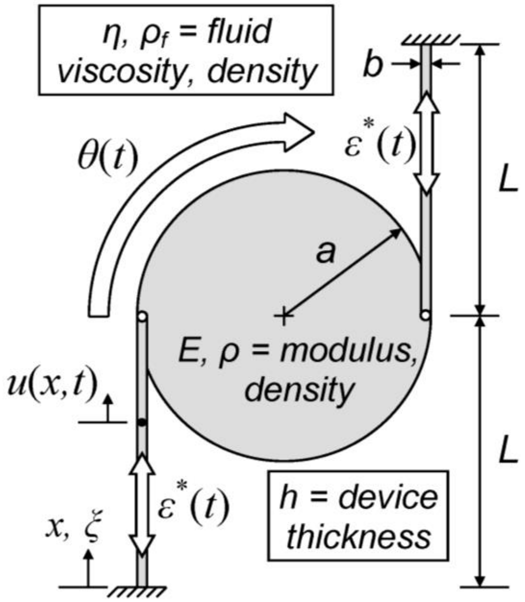

Fig. 1-2. Idealized schematic of an "all-shear interaction device" (ASID) actuated harmonically by imposed electrothermal axial strain in the legs. The legs and the disk interact with the fluid through shearing action only.

Since the existing experimental data on ASID-type devices [23, 24] was published with minimal theoretical support, the primary objective of the present research is to provide a detailed theoretical basis for the performance of the ASID in order to optimize its resonator performance and, for sensing applications, its performance metrics such as mass and chemical sensitivity and limits of detection. In particular, effects of the basic geometric and material parameters of the system on the in-fluid vibration characteristics of the device are to be explored through analytical modeling. These characteristics include the natural/resonant frequencies, the relative reductions in these frequencies in going from vacuum to a liquid medium, and the viscous quality factors of the system. While the modeling includes multi-modal behavior, the primary focus of the study will be on the fundamental in-plane rotational mode as it is the easiest to excite in practice.

To validate the new analytical models presented herein, theoretical results of the study will be compared with the existing experimental data on the mode-1 quality factor and with the results of FEA modal analyses on the fundamental natural/resonant frequency.

1.4. Organization of the Dissertation

After a brief introduction to the history and applications of MEMS, followed by a description of the problem to be addressed and the general objectives of the present study (Ch. 1), the main body of the dissertation begins in Ch. 2 with a literature review of MEMS resonators of various designs for applications in viscous fluid environments. These will include microcantilever-based geometries as well as less conventional non-cantilever designs, including that considered in this study.

In Ch. 3 a mechanics-based single degree-of-freedom (SDOF) (lumped-parameter) model of the ASID, used to describe the in-plane rotational vibration of the disk, is developed for the free-vibration and forced-vibration cases. The chapter opens with a discussion of several assumptions upon which the model is based, the most important being the use of a Stokes-type fluid resistance model on the disk, the assumption that the mass and fluid resistance associated with the legs are negligible, and the treatment of the legs as pure axial members (no bending). These assumptions permit the formulation of a relatively simple mathematical model that is subsequently solved for both the free- and forced-vibration cases. The simplicity of the SDOF model permits the derivation of relatively simple analytical estimates for the ASID response, including results for natural/resonant frequency and quality factor for the fundamental in-plane rotational mode. This model and the associated results will serve as valuable benchmarks for the remainder of the dissertation.

The SDOF model is subsequently generalized through the derivation of a more accurate, multi-model, continuous-system (distributed-parameter) model in Ch. 4 in which the leg mass and associated fluid resistance effects are included. The mathematical formulation of the continuous model leads to boundary value problems (BVPs) governing the (axial) free and forced vibrations of the legs in which the disk effects are incorporated via appropriate boundary conditions applied at the ends of the legs. The solution to the free-vibration case of the continuous model results in a complex-valued frequency equation whose solution yields the damped natural frequency and the decay parameter of the system for all modes of vibration involving axial leg vibration and in-plane disk rotation. Approximate analytical formulae for these two quantities and for the quality factors of the system are then obtained and expressed in terms of the device and fluid parameters. The free-vibration case of the continuous model also includes a separate section dedicated to the special no-disk case of the ASID (i.e., the in-fluid axial vibration of an isolated leg) in which the in-fluid eigenproperties of an axial-model microcantilever are derived analytically. For the forced-vibration case of the general ASID design, a separation of variables approach for the time- and space-dependent motion is used to derive the steady-state response of the system due to uniform, harmonic, electrothermal strains being imposed in an in-phase manner on the two actuated legs.

Chapter 5 presents and discusses the numerical results obtained from the SDOF and continuous models developed in the preceding chapters. The free-vibration results include the dependence of the damped fundamental frequency, the fluid-induced shift in the fundamental frequency, and the mode-1 quality factor of the ASID on the system parameters. The forced-vibration results include the frequency response of the system over a range of exciting frequencies from which the resonant characteristics of the system (fundamental resonant frequency and quality factor) are extracted and then compared with the results of the free-vibration case. For validation purposes, the analytical results are compared with the results of the FEA simulations as well as with the existing experimental data.

Chapter 6 focuses on the ASID performance metrics in mass-based sensing applications. The performance metrics of ASID-based resonant sensors are examined through the mass and chemical sensitivities and mass and chemical limits of detection (LOD) of the sensor and their dependence on the system parameters. Since these performance metrics depend on the resonant characteristics of the ASID, the analytical results of Chs. 3 and 4 for the SDOF and continuous models for the resonant frequency and quality factor are applied in this chapter to obtain analytical expressions relating the mass and chemical sensitivities and limits of detection to the ASID-based sensor's geometry and material properties and to the density and viscosity of the surrounding fluid.

Finally, the main conclusions of the present research are summarized in Ch. 7 and recommendations for future study of ASID-type devices are outlined in this chapter.

CHAPTER 2:

LITERATURE REVIEW

2.1. Conventional Microcantilever-Based Devices

The early studies of microcantilever-based resonators of transverse mode (out-of-plane flexure that we refer to as the “conventional” mode of vibration) operating in a viscous fluid environment may stem from the investigations of tapping-mode atomic force microscopy (AFM) in liquids in the early 1990’s [25-27] in which the vibrational response of the cantilever tip was used for topographic imaging of a sample (such as soft biological samples) in a fluid medium. Initial investigations – primarily based on experimental observations – of the impact of fluid effects on the AFM cantilevers found that, for example, the resonant frequency of the cantilever in water was 2 to 5 times lower than that in vacuum [28], and the quality factor of the AFM cantilever was significantly reduced due the effects of a surrounding viscous fluid [29, 30]. For example, Schäffer *et al*. [31] describes how purified water lowers the quality factor of the AFM cantilever to the order of unity compared to 10-100 in air, and how liquid resistance effects alter the frequency response of the system as opposed to the in-vacuum or in-air case.

It was not until 1998 when a detailed theoretical analysis of the vibrational characteristics of a transverse-mode cantilever immersed in a viscous fluid was presented by Sader [32]. In this paper, general analytical modeling for the frequency response of an in-fluid cantilever beam of arbitrary cross section excited by an arbitrary driving force was explored with several assumptions underlying the theory: the length of the cantilever must greatly exceed its nominal width, the vibration amplitude must be small, and the surrounding fluid must be incompressible. The effects of the fluid were incorporated into the model through the use of a frequency-dependent hydrodynamic function. While the theory is applicable to the case in which the geometry of the cantilever and the external force are arbitrary, Sader specialized the analytical results to the cases of a cantilever with rectangular cross section under the action of a thermal driving force (i.e., by Brownian motion of the molecules in the fluid) as they have been of significant practical importance in AFM applications. The fundamental-mode dynamic behavior of the transverse flexural-mode cantilever beam submerged in a viscous fluid was further extended by Green and Sader [33]. In that study the inertial and dissipative components of the hydrodynamic loading were rigorously calculated for the case of a cantilever oscillating in the vicinity of a solid surface.

The encouraging results achieved from experimental and theoretical investigations on the dynamic response of out-of-plane bending-mode microcantilevers have led to a vast and diverse use of these resonators in practical applications in recent years. Major areas of application include chemical and biological sensing [34-36] in which cantilever-based sensors are used, for example, to detect volatile organic compounds in gaseous or liquid media, to adsorb and detect bacteria (e.g., by coating the cantilever with specific antibodies), or to detect specific molecules bound to the surface of the device by monitoring the shift in resonant frequency of the cantilever. Transverse flexural-mode cantilevers have also been used for rheological measurement applications [39-44] in which the resonator is seen to have the capability of measuring the surrounding fluid properties such as density and viscosity. Energy harvesting is another application of cantilever-based devices, in which harvestable ambient energy in the form of heat, vibration, wind, electromagnetic waves, flowing water, or solar energy, can be converted to useful electrical power [9-13].

While the out-of-plane bending mode of vibration is still being used for microcantilever devices immersed in viscous fluid environments for various liquid-phase sensing applications, the viscous fluid poses significant challenges due to the drastic reduction in resonant frequency and quality factor of the device that is typically caused by the liquid's inertia and viscous energy dissipation [e.g., 32, 45-47]. These reductions in resonant frequency and quality factor usually translate into corresponding reductions in mass/chemical sensitivity and poorer limits of detection in sensing devices. (Details are provided in Ch. 6 of this dissertation for ASID-based sensors.) Therefore, as described in the subsequent sections of the present literature review, several researchers have focused their efforts on the exploration of alternative modes of resonant MEMS devices in order to overcome such challenges.

2.2. Microcantilevers Based on Unconventional Vibration Modes

One approach to improve the performance of microcantilever-based sensors in fluid environments has been the utilization of higher modes of transverse (out-of-plane) flexure as opposed to the fundamental mode. In a biosensing experiment, Braun *et al*. [48] used an array of micromechanical cantilevers to detect specific biomolecules bound to the functionalized surface of the sensor. They observed that the shift in resonant frequency of the cantilever due to the sorbed mass increases from the 11th mode of out-of-plane bending to modes 12 and 13, and that the corresponding mass sensitivity increases (improves) from 220 to 400 Hz/ng. By developing a finite element fluid-structure interaction model in which a three-dimensional linear elastic microcantilever interacts with the surrounding fluid that is modeled by using the three-dimensional incompressible Navier-Stokes equations, Basak *et al*. [45] explored the effect of hydrodynamic loading on the performance of liquid-phase microcantilever resonators vibrating at higher modes of transverse bending. The results for the first six modes indicate that higher-mode operation of the device reduces the added fluid mass coefficient significantly and also results in a higher quality factor as the mode number is increased. In an attempt to generalize and extend Sader's theoretical model presented in [32], Van Eysden and Sader [49] investigated the theoretical frequency response of cantilever beams immersed in viscous fluids for an arbitrary mode. In their article the hydrodynamic load on an oscillating thin blade of infinite length was used to account for the effects of the surrounding fluid on the out-of-plane bending vibration of the cantilever. The results indicate that driving the cantilever at its higher modes increases the quality factor of the device in gas and liquid media. The validity of the theoretical results of Van Eysden and Sader were confirmed by Ghatkesar *et al*. [50] in which experimental data for the eigenfrequency and quality factor of an array of eight microcantilevers immersed in water was presented for the first 16 modes, showing that the quality factor increases from 1 at the fundamental mode to 30 at the 16th mode. However, while operating the microcantilever at higher modes of transverse flexure may be desirable as it improves the performance (e.g., mass sensitivity) of the sensor in viscous fluids, there exist practical challenges such as the feasibility of excitation at higher frequencies or the weakness of output signals for detection purposes due to the small vibration amplitude at higher modes.

An alternative mode of vibration to the out-of-plane flexure of liquid-phase microcantilevers is the in-plane or lateral flexural mode in which the device vibrates in a manner corresponding to bending about the cross section's "strong axis" (i.e., the beam motion is parallel to its two wider lateral surfaces). Sharos *et al*. [51] performed an experiment in which they tested the performance of bending-mode microcantilevers to detect a target mass particle for both the transverse and lateral flexural modes, concluding that the quality factor and mass sensitivity obtained from the lateral-mode results are significantly higher than those obtained from the conventional transverse mode. Dufour *et al*. [52] theoretically compared the strong-axis or lateral bending mode with the weak-axis or transverse bending mode in microcantilever sensors for gaseous and liquid environments. The results show that switching from the transverse mode to the lateral mode improves the sensitivity and limit of detection of the sensor significantly (due to the larger stiffness of the cantilever in the lateral mode that results in a higher resonant frequency, and smaller viscous fluid effects in this mode that increases the quality factor). The study also indicated that the improvement in sensing performance of the device in the lateral mode (vs. the transverse mode) is more pronounced when the surrounding medium is liquid as opposed to gas. In an effort to derive simple closed-form expressions for the resonant frequency and quality factor of a lateral-mode microcantilever in fluid in terms of the basic geometric and material parameters, Heinrich *et al*. [53] employed a simple single degree-of-freedom (SDOF) model to predict the vibratory response of the cantilever in the fundamental lateral mode. The major assumptions on which that model is based are the following: (a) solution to Stokes's second problem [54] is used to incorporate the fluid effects in the model; (b) fluid effects are applied only to the larger faces of the device; hence this model is most applicable for thin microcantilevers vibrating in-plane; and (c) the cantilever is assumed to vibrate with a constant shape given by the first mode shape in vacuum. The SDOF model was extended by the same research group and presented in [55], in which a continuous-system model of the microcantilever based on Bernoulli-Euler beam theory yields more accurate results and shows certain advantages over the SDOF model (e.g., the ability to determine the resonant characteristics at higher modes of lateral flexure). General observations from the results of the aforementioned research studies on lateral-mode microcantilevers, along with other theoretical and experimental investigations on such devices by the same group [e.g., 56-60], show that using a wider and shorter cantilever improves the resonator and sensing performance of lateral-mode microcantilevers. These suggested geometries for a lateral-mode microcantilever sensor, however, will eventually violate the geometric limitations of the Bernoulli-Euler beam theory in which the width is assumed to be much smaller than the length. To overcome this modeling limitation, Schultz *et al*. [61-64] developed a new analytical model based on Timoshenko beam theory for lateral-mode microcantilever resonators operating in viscous fluids in which the “Timoshenko effects” (shear deformation and rotatory inertia) are seen to become important for microcantilevers of small slenderness ratios (i.e., the wide and short types that demonstrate higher quality factors in liquid).

Periodic axial (longitudinal) deformation of microcantilevers is another form of in-plane vibration that may be employed as an alternative to the classic out-of-plane bending mode in an attempt to improve liquid-phase sensor performance [58]. Recent experimental data show that axial-mode microcantilevers are capable of yielding relatively high quality factors in liquid for (bio)chemical sensing applications. For example, although their data correspond to a gaseous environment, Lakhmi *et al*. [65] achieved a quality factor of 300-400 for the longitudinal mode compared to Q values of 20-40 for the out-of-plane mode, suggesting that the axial-mode microcantilever is a potential high-Q sensor for liquid-phase applications. Castille *et al*. [66] measured a quality factor of 22 for an axial-mode microcantilever immersed in a 300-cP (0.3-Pa·s) liquid. In the present research, a theoretical model of an axial-mode cantilever is considered as a special case of the ASID device (corresponding to the limit as the disk radius approaches zero) due to its potential importance in liquid-phase sensing applications. Moreover, the resonant characteristics and sensing performance metrics for this device will be explored through a detailed parametric study.

In addition to the (transverse and lateral) bending and axial modes, researchers have also explored the torsional vibration of microcantilevers in fluids [45, 49, 51, 67-70]. Measurements from Sharos *et al*. [51] show that the quality factor results associated with the mode-1 torsional mode of the test microcantilevers are higher than those obtained from mode-1 lateral flexure and are also higher than those obtained from the first three modes of transverse flexure. In a theoretical analysis, Cai *et al*. [70] also found that the quality factor obtained from the torsional-mode microcantilever exhibits higher values compared to the transverse mode (as was also the case for cantilevers operated in the lateral flexural mode). The effect of the geometric parameters on the quality factor of the microcantilever was also examined in that study; in particular, the quality factor was found to increase as the length is decreased or as the thickness is increased for all three modes of vibration (transverse flexure, lateral flexure, and torsion). However, while the quality factor associated with transverse or lateral flexure tends to decrease as the width of the microcantilever decreases, the torsional-mode quality factor is seen to be relatively insensitive to this geometric parameter.

In an effort to improve the quality factor of (mode-1) transverse flexural-mode microcantilevers in viscous fluids, Linden and Oesterschulze [71] approached the problem by partially wetting the device. In their device only the top surface of the cantilever is placed into contact with the liquid so that the fluid-structure interaction is reduced. The measured data show a significant increase in the quality factor (79 in water) relative to a fully immersed device, a measured mass sensitivity of 2.77 fg/Hz after the adhesion of one latex bead (with a mass of 8.6 pg) to the cantilever, and a "conservative estimate" of the limit of detection on the order of 30 fg.

In a new class of liquid-phase microcantilever-based sensors, researchers have explored the implementation of cantilevers with embedded microfluidics whereby the viscous fluid flows through microchannels inside the cantilever that is surrounded by vacuum, thus minimizing the fluid effects that normally degrade the performance of the sensor. This concept has indicated a significant increase in the sensitivity and quality factor of the device for mass-based sensing applications [72-74]. Sader *et al*. [75] have rigorously investigated the fluid dynamics in microfluidic microcantilever resonators through a theoretical model that incorporates the elastic deformation of the cantilever (based on the Bernoulli-Euler beam theory) and the fluid flow inside the channel whose width is assumed to greatly exceed its thickness, finding that, unlike conventional microcantilevers immersed in liquid, the compressibility of the fluid in addition to the density and viscosity parameters may affect the flow dynamics. Moreover, it was found that the quality factor of the system does not vary in a monotonic fashion with respect to the fluid viscosity, and that it is feasible to miniaturize the device while simultaneously reducing the energy dissipation in the system.

2.3. MEMS Resonators of Novel Designs

Non-cantilever designs of MEMS resonators for mass sensing applications in gaseous or liquid environments have also been the focus of researchers in recent years. A new silicon-based, disk-shape resonator, consisting of two semicircular half-disks attached to a central anchor beam through two support beams, was fabricated and tested by Seo and Brand [76]. In their device they utilized electrothermal excitation by means of heating resistors embedded in the support beams, which resulted in an in-plane rotational vibration of the half-disks whose motion was detected by a piezoresistive Wheatstone bridge designed to be sensitive only to this mode of vibration. This device yielded measured quality factors of up to 5800 in air and 94 in water, indicating high-performance capabilities for chemical and biochemical sensing as an alternative to more conventional (microcantilever-based) sensors. Waggoner *et al*. [77] explored the performance of trampoline-shaped, 90-nm-thick nanomechanical resonators made of silicon nitride and mounted in a chamber in which the pressure could be varied. The measured data exhibits quality factors on the order of 2000 in air, even after depositing a relatively thick layer of polymer (10 nm) onto the device for chemical detection purposes, suggesting the resonator as a potential sensor for liquid-phase applications. In an attempt to extend the concept of partial wetting of the resonator that yielded promising results as mentioned in the previous section ([71]), Linden *et al*. [78] applied the concept to the case of a “suspended plate” device that vibrates in its own plane. The “shear-mode” resonator in their experiment (named as such due to the shearing interaction between the plate and a liquid droplet) consists of a suspended silicon plate supported by four beams. Due to the application of the two concepts at the same time, i.e., partial contact with a liquid droplet on one side of the plate (as opposed to the case of a fully immersed device), and operating the device in its in-plane mode rather than out-of-plane mode, a high quality factor of 490 and mass sensitivity of 80 Hz/pg were achieved for water, while a relatively high (undesirable) limit of detection on the order of 28 pg was primarily due to the large mass of the sensor.

Another example of a novel design for liquid-phase MEMS devices is the disk-type microresonator which has already been introduced in Sects. 1.2 and 1.3 of the previous chapter (described as an “all-shear interaction device” or ASID) as it is the focus of the present study. This resonator (Fig. 1-1), originally fabricated and tested by Rahafrooz and Pourkamali [23, 24], has shown a potentially high performance in viscous fluid environments relative to other devices that are fully immersed in liquid. In their experiments the device, consisting of a microdisk structure supported by two tangentially-oriented beams as shown in Fig. 1-1, is excited via the application of electrothermal axial strain in the support beams. Due to the high electrical resistance of the supporting beams, passing an electrical current from one support to the other results in a fluctuating temperature gradient and therefore fluctuating thermal strain in the beams, causing the disk to oscillate in its in-plane rotational mode. Since the support beams also serve as piezoresistive stress sensors (due to the piezoresistive effect), the periodic tensile and compressive stress in the beams results in periodic changes in their electrical resistance that can be measured through the output AC current signal whose amplitude is proportional to the vibration amplitude of the resonator. (References [79, 80] discuss in detail the thermal actuation and detection schemes of such high-frequency resonators. A more general discussion of thermally actuated resonators may be found in [81].) This type of device, by virtue of its interaction with the surrounding fluid primarily through shearing action (i.e., without stroking against the liquid) has shown unprecedented liquid-phase quality factors of 304 in heptane [24] and 284 in water [23], thus exhibiting the potential to serve as a platform for highly sensitive devices for biosensing applications [82], liquid viscosity measurements [83], and subatomic resolution force and displacement measurements in liquid media [84].

The literature review provided in this chapter has focused on the history of some major microcantilever and non-cantilever MEMS resonators for liquid-phase resonator/sensor applications, including several important theoretical, numerical, and experimental studies. The review has summarized the different approaches utilized in an attempt to enhance the performance of such devices in viscous fluid environments. While various types of microcantilever resonators have been extensively investigated in recent years, novel designs of MEMS devices and, in particular, the aforementioned ASID device, lack detailed analytical modeling aimed at a rigorous analysis of how their performance depends on device design parameters and fluid properties. The current research, therefore, seeks to establish detailed analytical modeling of an ASID resonator of arbitrary dimensions, fully immersed in a viscous liquid, since the proof-of-concept has already been demonstrated by the experimental data of [23, 24]. This analytical modeling will permit the derivation of explicit analytical expressions for frequency response, the resonant characteristics (resonant frequencies and associated quality factors) and sensing metrics (sensitivity and limit of detection) of the ASID sensor. This will enable one to determine the functional dependence of the ASID performance on the resonator’s geometric and material parameters and the fluid’s density and viscosity, results that will be exhibited via a detailed parametric study. These results will also serve as the basis of design guidelines for maximizing the device performance for a variety of applications.

CHAPTER 3:

SINGLE-DEGREE-OF-FREEDOM MODELING OF THE ASID

3.1. Introduction

In Ch. 3 vibration characteristics of a rotational mode disk resonator supported by two tangentially-oriented elastic microcantilevers or "legs" are to be studied by means of a simple single-degree-of-freedom (SDOF) model. Mathematical formulations are explicitly developed for both free- and forced-vibration cases in a viscous fluid. The equations of motions are derived in terms of the disk rotation angle by employing the direct equilibrium method on the disk. The primary objective of this chapter is to derive simple analytical expressions relating the in-fluid natural frequency and corresponding quality factor (for free-vibration case) as well as in-fluid resonant frequency and quality factor at resonance (for forced-vibration case) to the geometric and material parameters of the device/fluid system. (These results area also summarized in two recent publications for the free- [85] and forced-vibration [86] cases.) The analytical expressions based on the SDOF modeling will be useful for comparison purposes in later chapters when a more "exact" continuous-systems dynamic modeling approach will be employed.

3.2. Modeling Assumptions

The idealization of the device of interest, consisting of a micro-disk and two supporting legs, will enable us to treat its in-plane rotational vibration analytically through a simple single- degree-of-freedom (SDOF) model. The major assumptions upon which the final form of the SDOF model will be based are as follows:

1. The disk is rigid, solid, and homogeneous;
2. The supporting legs are homogeneous and made of a material that is linear elastic. In addition, the legs are assumed to be of rectangular cross section and prismatic, i.e., the cross section is uniform along the leg length;
3. Each leg is perfectly fixed at one end (i.e., zero displacement and bending slope) and tangentially attached to the disk at the other end.
4. The legs are much smaller than the disk so that their mass and fluid resistance are negligible relative to their disk counterparts;
5. The legs provide only axial force to the disk, i.e., no bending moment is transferred between the disk and each leg;
6. Fluid damping is the dominant source of energy dissipation in the system so that the overall quality factor can be estimated as that due to the viscous losses in the fluid;
7. The local fluid resistance on all surfaces of the disk is given by the classical solution of Stokes's second problem for a rigid plane oscillating harmonically in a viscous fluid [53-55, 61];
8. The vibration amplitude is sufficiently small so that nonlinear effects are negligible;
9. Regarding the forced-vibration case, the external input to the system is a thermal "eigenstrain," such as that associated with harmonic temperature changes generated by an AC electrical current applied to the legs. When the device is excited by imparting this harmonic axial strain to the legs, an in-plane rotational oscillation of the disk will ensue.

3.3. Mathematical Formulation and Solution for the Free-Vibration Case

The derivation of the ordinary differential equation governing the behavior of the system may be performed by considering moment equilibrium of the disk. In order to derive the equation of motion of the disk, the reactions at the junction points (i.e., where the legs are connected to the disk) as well as the inertial load and liquid resisting moment on the disk must be determined.

3.3.1. Derivation of the Reactions at the Disk-Leg Junctions

The static relationships between the deflection of a beam and the end actions (forces and moments) enable us to determine the reaction forces shown in Fig. 3-1. (The utilization of statics is valid here since the legs are treated as massless springs in the SDOF model.) These reactions, consisting of an axial force (*F*), a shear force (*V*), and a bending moment (*M*), can be related to the disk rotation as will now be shown.

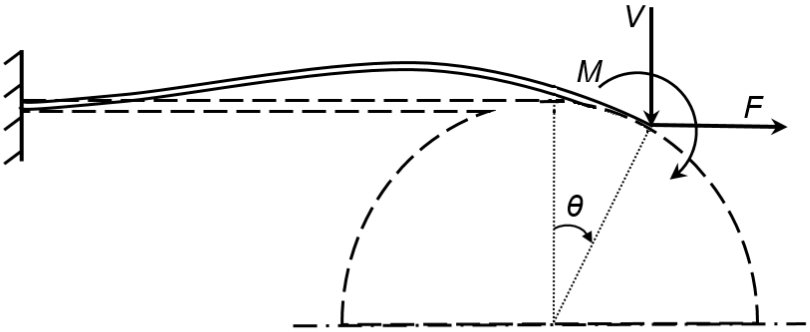

Fig. 3-1. Deflection and end loads of a supporting leg due to the rotation of the disk

Assuming that the axial and bending deformations are uncoupled, the axial deflection of the beam shown in Fig. 3-1 is expressed as follows [87]:

$$\delta_{axial} = \frac{FL}{EA} \tag{3-1a}$$

where *E* is the modulus of elasticity of the material, *A*= *bh* is the area of the leg's rectangular cross section of width *b* and thickness *h* (the latter being perpendicular to the plane of Fig. 3-1), and *L* is the length of the leg. The transverse deflection and bending slope at the end of the leg are related to the end shear force and moment by the following expressions [87]:

$$\delta_{trans.} = \frac{VL^3}{3EI} + \frac{ML^2}{2EI} \tag{3-1b}$$

$$\theta = \frac{VL^2}{2EI} + \frac{ML}{EI} \tag{3-1c}$$

in which *I* is the second moment of area of the cross section. Assuming that the disk rotates by a small angle, θ, the axial and transverse deflections can be related to the disk rotation angle in a simple manner:

$$\delta_{axial} = a\ \sin\theta = a\ \theta + O\left(\theta^3\right) \text{as } \theta \to 0 \tag{3-2a}$$

$$\delta_{trans.} = a\left(1 - \cos\theta\right) = \frac{a\,\theta^2}{2} + O\left(\theta^4\right) \text{ as } \theta \to 0 \tag{3-2b}$$

with *a* being the radius of the disk. The axial reaction can be related directly to the rotation angle θ by substituting Eq. (3-2a) into Eq. (3-1a):

$$F = \frac{EAa}{L}\theta - \frac{EAa}{6L}\theta^3 + O\left(\theta^5\right) \quad \text{as} \quad \theta \to 0 \tag{3-3a}$$

The transverse force and moment reactions are determined by solving Eqs. (3-1b) and (3-1c) and using Eq. (3-2b):

$$V = -\frac{6EI}{L^2}\theta + \frac{6EIa}{L^3}\theta^2 + O\left(\theta^4\right) \quad \text{as} \quad \theta \to 0 \tag{3-3b}$$

$$M = \frac{4EI}{L}\theta - \frac{3EIa}{L^2}\theta^2 + O\left(\theta^4\right) \quad \text{as} \quad \theta \to 0 \tag{3-3c}$$

3.3.2. Fluid Resistance on the Surfaces of the Disk

The derivation of the fluid resistance on the motion of the disk is based on the results from “Stokes’s second problem” [54] for the steady-state in-plane translational oscillation of an infinite flat plane in a viscous liquid. Assuming that the plane experiences a non-decaying oscillation in the viscous fluid, the shear stress exerted by the liquid on the surface of the plane is expressible as a linear combination of the velocity, $\dot{D}$, and acceleration, $\ddot{D}$, of the surface, where D is the displacement of the surface and dots denote differentiation with respect to time *t*:

$$\tau = \bar{\bar{m}}_f \ddot{D} + \bar{\bar{c}}_f \dot{D} \tag{3-4a}$$

where

$$\bar{\bar{m}}_f = \sqrt{\frac{\rho_f \eta}{2\omega}} \tag{3-4b}$$

$$\bar{\bar{c}}_f = \sqrt{\frac{\omega \rho_f \eta}{2}} \tag{3-4c}$$

are the effective fluid mass per unit area and effective fluid damping coefficient per unit area, while ω is the oscillation frequency of the plane. (Note that the fluid mass and damping coefficients may be related to their mass-per-unit-length counterparts, often denoted by g_2 and g_1, respectively. See, e.g., [42].) Despite the fact that the Stokes solution is for the translational movement of a rigid plane, we shall assume that, when a circular disk oscillates about its center with small amplitude, the local fluid resistance is the same as that for a plane translating with a velocity history identical to the local velocity on the rotating disk surface. This assumption, analogous to that employed in modeling fluid-resistance on lateral-mode cantilevers [53, 55, 61], will permit us to estimate the resisting torques associated with the shear stresses acting on the circular surfaces and on the lateral surface of the disk, as indicated schematically in Fig. 3-2.

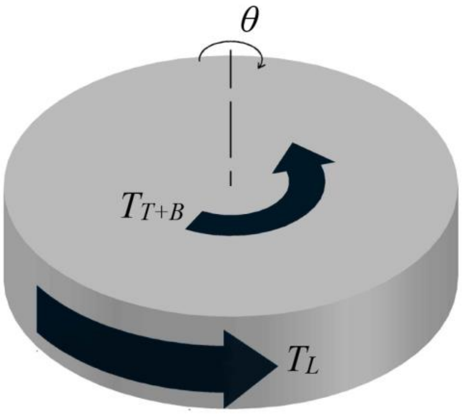

Fig. 3-2. Torques associated with fluid resistance on the top/bottom surfaces (T_{T+B}) and the lateral surface (T_L) of the disk

Let *r* be the radial distance of any element of the disk measured from the axis of rotation of the disk and θ the angle through which the disk has turned from the neutral position at which the legs are unstrained. Noting that $D = r\theta$ gives the displacement of any point on the disk surface and using the Stokes result, Eqs. (3-4a-c), leads to the following expression for the shear stress exerted by the liquid on all surfaces of the disk (τ being taken positive in the counterclockwise direction of Fig. 3-2):

$$\tau = \sqrt{\frac{\omega \rho_f \eta}{2}} \left(r\dot{\theta} + \frac{r}{\omega} \ddot{\theta} \right) \tag{3-5}$$

Parameter ω is the (circular or angular) frequency at which the disk oscillates rotationally, while ρ_f and η are the density and dynamic viscosity of the surrounding fluid, respectively. (Symbol f will be used at times to represent frequency in units of Hz.)

For the top and bottom surfaces of the disk, the moment of the shear stress distribution on those surfaces gives the corresponding resisting torque:

$$T_{T+B} = 2\int_0^{2\pi}\int_0^{a} r\tau \left(r dr d\theta \right) = \pi a^4 \sqrt{\frac{\omega \rho_f \eta}{2}} \left(\dot{\theta} + \frac{1}{\omega} \ddot{\theta} \right) \tag{3-6}$$

To determine the liquid resistance torque on the lateral surface of the disk, the moment of the uniform shear stress on that surface is easily determined:

$$T_L = \tau \left(2\pi a h \right) a = 2\pi a^3 h \sqrt{\frac{\omega \rho_f \eta}{2}} \left(\dot{\theta} + \frac{1}{\omega} \ddot{\theta} \right) \tag{3-7}$$

where *h* is the uniform thickness of the device.

3.3.3. Derivation of the Dimensional Equation of Motion of the Disk

The following is the derivation of the disk equation of motion with all leg reactions and fluid effects incorporated using the Stokes resistance model. Figure 3-3 shows the disk rotating a small angle, θ, with all the forces and moments acting on it. The inertial force in Fig. 3-3 is denoted by

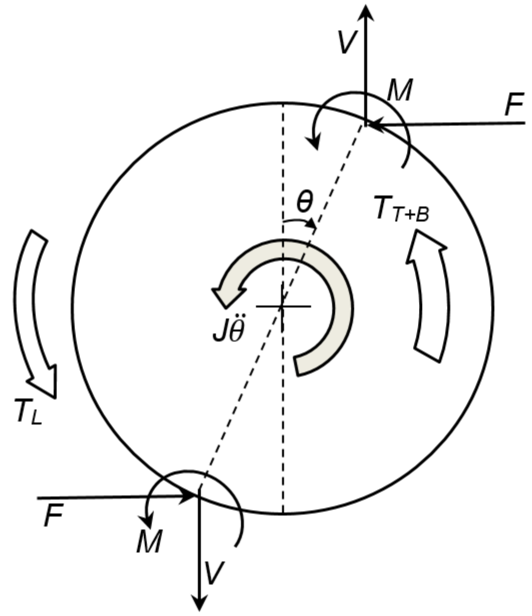

Fig. 3-3. Free body diagram of the disk for equation of motion derivation

$J\ddot{\theta}$ in which $J = \dfrac{\rho\pi a^4 h}{2}$ is the polar moment of inertia of the disk, with ρ being the density of the disk material. Other relevant notation in Fig. 3-3 has already been defined in the previous sections. Moment equilibrium of the disk will lead to the following equation of motion in which all terms up to and including the third order have been included:

$$\left(\frac{\rho\pi a^4 h}{2}+\pi a^4\sqrt{\frac{\rho_f\eta}{2\omega}}+2\pi a^3 h\sqrt{\frac{\rho_f\eta}{2\omega}}\right)\ddot{\theta}+\left(\pi a^4\sqrt{\frac{\omega\rho_f\eta}{2}}+2\pi a^3 h\sqrt{\frac{\omega\rho_f\eta}{2}}\right)\dot{\theta}$$
$$+\left(\frac{2EAa^2}{L}+\frac{8EI}{L}\right)\theta-\frac{18EIa}{L^2}\theta^2+\left(\frac{12EIa^2}{L^3}-\frac{4EAa^2}{3L}\right)\theta^3=0 \qquad \text{(3-8a)}$$

By neglecting the nonlinear terms in view of the assumption that the vibration amplitude is small and using the assumption that the cross section is rectangular, Eq. (3-8a) takes the following linearized form:

$$\pi a^4\left[\frac{\rho h}{2}+\left(1+\frac{2h}{a}\right)\sqrt{\frac{\rho_f\eta}{2\omega}}\right]\ddot{\theta}+\pi a^4\left(1+\frac{2h}{a}\right)\sqrt{\frac{\omega\rho_f\eta}{2}}\dot{\theta}+\frac{2AEa^2}{L}\left[1+\frac{1}{3}\left(\frac{b}{a}\right)^2\right]\theta=0 \qquad \text{(3-8b)}$$

The term $(b/a)^2$ can be neglected, provided that $b \ll a$, yielding

$$\pi a^4\left[\frac{\rho h}{2}+\left(1+\frac{2h}{a}\right)\sqrt{\frac{\rho_f\eta}{2\omega}}\right]\ddot{\theta}+\pi a^4\left(1+\frac{2h}{a}\right)\sqrt{\frac{\omega\rho_f\eta}{2}}\dot{\theta}+\frac{2AEa^2}{L}\theta=0 \qquad \text{(3-8c)}$$

Eq. (3-8c) is the dimensional equation of motion of the idealized model described earlier with the assumptions outlined in Sect. 3.2. In the following section this dimensional equation of motion will be converted to a more convenient non-dimensional form.

3.3.4. Non-Dimensional Equation of Motion of the Disk

The dimensional form of the disk equation of motion can be written in non-dimensional form by introducing the following dimensionless parameters:

$\theta \equiv \theta(\bar{t})$ = total angle of disk rotation as a function of dimensionless time (3-9a)

$\bar{t} \equiv \omega_0 t$ = dimensionless time (3-9b)

$$\bar{\varpi} \equiv \omega / \omega_0 = \text{normalized natural frequency} \tag{3-9c}$$

$$\omega_0 \equiv \frac{\pi}{2L}\sqrt{\frac{E}{\rho}} = \text{in-vacuum fundamental axial frequency of a single leg} \tag{3-9d}$$

$$\zeta \equiv \left(1+\frac{2h}{a}\right)\left(\frac{L^2}{h^4}\frac{{\rho_f}^2\eta^2}{E\rho^3}\right)^{1/4} = \text{fluid resistance quantity} \tag{3-9e}$$

$$\alpha \equiv \frac{a^2}{bL} = \text{normalized disk area} \tag{3-9f}$$

Applying (3-9a) through (3-9f) to (3-8c) and now letting dots denote differentiation with respect to $\bar{t}$ results in the following non-dimensional equation of motion for the SDOF model:

$$\left(1+\frac{2\zeta}{\sqrt{\pi}}\frac{1}{\sqrt{\bar{\varpi}}}\right)\ddot{\theta}+\frac{2\zeta}{\sqrt{\pi}}\sqrt{\bar{\varpi}}\dot{\theta}+\frac{16}{\pi^3\alpha}\theta=0 \tag{3-10}$$

Equation (3-10) indicates that the system can be described completely by two dimensionless parameters: ζ (fluid resistance) and α (normalized disk area).

3.3.5. Frequency Equation and Quality Factor

Assuming that $\bar{\varpi}$ is insensitive to the damping term in (3-10), the stiffness and $\bar{\varpi}$ -dependent mass in (3-10) dictate that $\bar{\varpi}$ must satisfy

$$\left(\sqrt{\bar{\varpi}}\right)^4+\frac{2\zeta}{\sqrt{\pi}}\left(\sqrt{\bar{\varpi}}\right)^3-\frac{16}{\pi^3\alpha}=0 \tag{3-11}$$

which may easily be solved numerically for general values of α and ζ . In practice, however, ζ is often so small that the truncated Taylor's series solution to (3-11) may be used. We therefore write ϖ in the form

$$\varpi(\zeta)=\varpi(0)+\varpi'(0)\zeta+O\left(\zeta^2\right) \text{ as } \zeta\to 0 \tag{3-12a}$$

Coefficients $\varpi(0)$ and $\varpi'(0)$ can be determined using (3-11), then subsequently substituted into (3-12a), resulting in an approximate analytical expression for the normalized natural frequency:

$$\varpi\approx\frac{4}{\sqrt{\pi^3\alpha}}\left[1-\frac{(\pi\alpha)^{1/4}\zeta}{2}\right]=\frac{4}{\sqrt{\pi^3}}\left(\frac{bL}{a^2}\right)^{1/2}\left[1-\frac{\pi^{1/4}}{2}\left(\frac{L}{bh^2}\frac{\rho_f{}^2\eta^2}{E\rho^3}\right)^{1/4}\left(\frac{2+a/h}{\sqrt{a/h}}\right)\right],\ \zeta\ll 1 \tag{3-12b}$$

Figure 3-4 shows how the analytical approximate formula (3-12b) begins to deviate from the exact natural frequency [i.e. the numerical solution to (3-11)] as the fluid parameter increases, but gives an excellent approximation at sufficiently small values of the fluid resistance parameter, ζ .

The analytical expression for the natural frequency enables us to calculate the damping ratio of the system, *d*, and thus the quality factor, *Q*, by placing (3-12b) into (3-10). More specifically, using the effective mass ("*M*"), damping ("*C*"), and stiffness ("*K*") coefficients implied by (3-10), we have

$$Q\equiv\frac{1}{2d}=\frac{2\sqrt{KM}}{2C}\approx\frac{1}{(\pi\alpha)^{1/4}\zeta}=\frac{1}{\pi^{1/4}}\left(\frac{bh^2}{L}\frac{E\rho^3}{\rho_f{}^2\eta^2}\right)^{1/4}\frac{\sqrt{a/h}}{2+a/h},\qquad \zeta\ll 1 \tag{3-13}$$

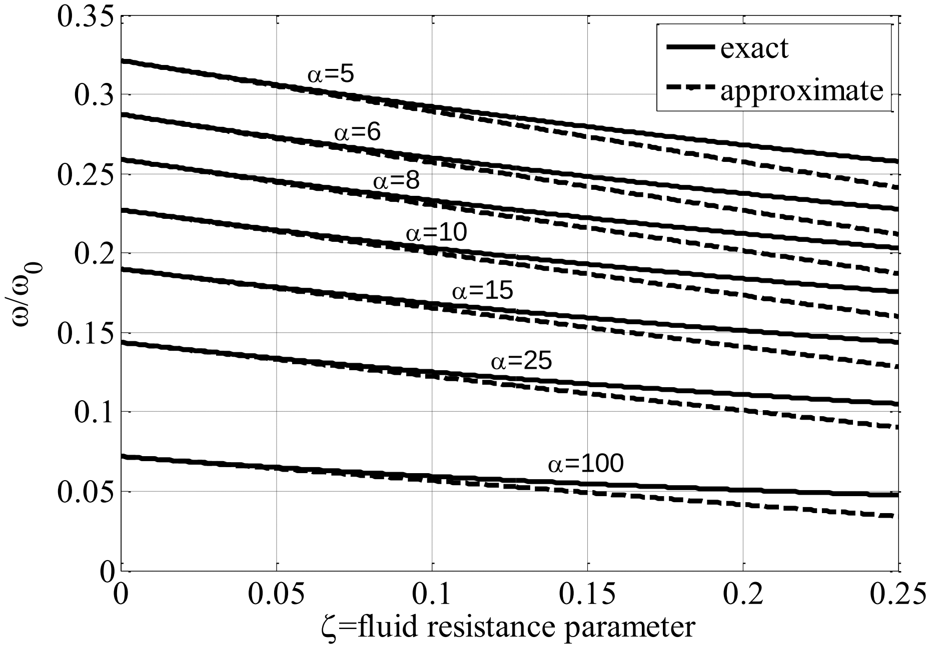

Fig. 3-4. Normalized natural frequency of SDOF model vs. fluid resistance parameter: comparison of approximate formula, Eq. (3-12b), and exact solution of Eq. (3-11).

From (3-12b) and (3-13) the relative drop in ω (with respect to vacuum) is

$$\left|\frac{\Delta\omega}{\omega}\right| \equiv \left|\frac{\omega-\omega_{vac.}}{\omega_{vac.}}\right| = \frac{1}{2Q} \qquad (3\text{-}14)$$

The simple relationship between the relative fluid-induced drop in natural frequency and the quality factor of the ASID, given by (3-14), may be useful in the sense that knowing one of these quantities permits an estimation of the other. Equations (3-12b)-(3-14) are explicit analytical results for the in-fluid values of the natural frequency, the quality factor, and the relative decrease in natural frequency of the ASID in the fundamental rotational mode considered. Equation (3-13) implies the existence of a relative maximum for Q with respect to the disk size [and (3-14) a relative minimum for $\left|\Delta\omega/\omega\right|$] at the theoretically optimal value of $a/h = 2$:

$$Q_{\max} = Q\big|_{a/h=2} = \frac{\sqrt{2}}{4\pi^{1/4}}\left(\frac{bh^2}{L}\frac{E\rho^3}{{\rho_f}^2\eta^2}\right)^{1/4} \tag{3-15a}$$

$$\left|\frac{\Delta\omega}{\omega}\right|_{\min} = \left|\frac{\Delta\omega}{\omega}\right|_{a/h=2} = \frac{1}{2Q_{\max}} \tag{3-15b}$$

3.4. Mathematical Formulation and Solution for the Forced-Vibration Case

The focus in this section is the development of a simple theoretical model of the ASID’s forced-vibration response to determine its in-fluid resonant characteristics. (Details have recently been published [86].) The derivation of the governing equation of motion follows the procedure described earlier in Sect. 3.3. In this case, however, the supporting legs undergo imposed eigenstrains of the type that would be caused, for example, by periodic temperature changes generated by an electrical AC current applied to them.

3.4.1. Derivation of the Equation of Motion

The external input to the system is described as a harmonic eigenstrain, ε^*, that causes axial deformations (periodic expansion and contraction) in the legs. The total leg extension, equal to the displacement at the end of a single leg and relatable to the disk rotation via $u_{tot} \approx a\theta$, has two components: one that is associated with the stress-free eigenstrain, $\varepsilon^* L$, and the other that is associated with the elastic deformation of the leg,

$u_e = \frac{FL}{EA}$, where F is the axial force in the leg. Only the elastic part of the leg deformation is associated with axial stress in the leg and, thus, with an axial force and a resulting resisting moment on the disk. The elastic displacement can therefore be written as follows:

$$u_e = a\theta - \varepsilon^* L \tag{3-16}$$

in which we have assumed that the disk rotation is small, resulting in the first term on the right-hand side being linear in θ. The axial force in the leg may then be expressed as

$$F = \frac{EA}{L}\left(a\theta - \varepsilon^* L\right) \tag{3-17}$$

Employing all the assumptions outlined in Sect. 3.2 and a similar procedure as was adopted for the free-vibration case in Sect. 3.3, the equation of motion for the forced-vibration case may be derived in the following form:

$$\left(1 + \frac{2\zeta}{\sqrt{\pi}}\frac{1}{\sqrt{\bar{\omega}}}\right)\ddot{\theta} + \frac{2\zeta}{\sqrt{\pi}}\sqrt{\bar{\omega}}\dot{\theta} + \frac{16}{\pi^3\alpha}\theta = \frac{16L/a}{\pi^3\alpha}\varepsilon^*\left(\bar{t}\right) \tag{3-18}$$

where the system is excited by imparting the stress-free axial strain, $\varepsilon^*\left(\bar{t}\right) = \varepsilon_0 e^{i\bar{\omega}\bar{t}}$, to the legs, in which the parameter ε_0 is the amplitude of the imposed eigenstrain and $\bar{\omega} \equiv \omega / \omega_0$, with ω being the circular frequency of the imposed eigenstrain. (For a thermally induced eigenstrain $\varepsilon_0 = \Delta T \times CTE$, where ΔT is the temperature change amplitude in the legs and CTE is the coefficient of thermal expansion of the leg material along the axial direction of the leg.)

3.4.2. Solution Due to Imposed Harmonic Leg Strain

The steady-state solution to (3-18) is achieved by assuming a harmonic response of the form

$$\theta\left(\bar{t}\right)=\theta_0 e^{i\bar{\omega}\bar{t}} \tag{3-19}$$

resulting in the complex disk rotation amplitude

$$\theta_0=\frac{L\varepsilon_0 / a}{1-\frac{\pi^{5/2}}{8}\alpha\bar{\omega}^2\left(\frac{\sqrt{\pi}}{2}+\frac{\zeta}{\sqrt{\bar{\omega}}}-i\frac{\zeta}{\sqrt{\bar{\omega}}}\right)} \tag{3-20}$$

The modulus (absolute value) of θ_0 gives the magnitude of the disk rotation amplitude, while the argument of θ_0 gives the phase shift. The latter may be shown to satisfy

$$\tan\phi=\frac{1}{\frac{\sqrt{\pi\bar{\omega}}}{\zeta}\left(\frac{1}{2}+\frac{\zeta}{\sqrt{\pi\bar{\omega}}}-\frac{8}{\pi^3\alpha\bar{\omega}^2}\right)} \tag{3-21}$$

where $\phi\in[-\pi,0]$; thus, $-\phi$ physically represents the angle by which the response lags the excitation.

3.4.3. Analytical Estimates for Resonant Frequency and Quality Factor

The free-vibration solution corresponding to the homogeneous form of (3-18) was derived in Sect. 3.3.5 where explicit equations relating the in-fluid natural frequency, quality factor, and relative decrease in natural frequency (from vacuum to fluid) to the system parameters were obtained. Assuming that the resonant frequency f_{res} (i.e., the driving frequency in Hz causing peak response amplitude), the quality factor at resonance, and the relative decrease in resonant frequency (from vacuum to fluid) may be approximated by the corresponding free-vibration results, one may use the previously derived analytical estimates [Eqs. (3-12b)-(3-14)] for the harmonically excited device:

$$f_{res} \approx \sqrt{\frac{Eb}{\pi^3 \rho a^2 L}}\left[1-\left(1+\frac{2h}{a}\right)\left(\frac{\pi}{16}\frac{a^2 L}{bh^4}\frac{\rho_f^2 \eta^2}{\rho^3 E}\right)^{1/4}\right] \tag{3-22a}$$

$$Q \approx \left[\frac{1}{\pi}\left(\frac{\rho^3 E}{\rho_f{}^2 \eta^2}\right)\left(\frac{bh^2}{L}\right)\right]^{1/4} \frac{\sqrt{a/h}}{2+a/h} \tag{3-22b}$$

$$\left|\frac{\Delta f_{res}}{f_{res}}\right| \approx \frac{1}{2Q} = \frac{1}{2}\left[\pi\left(\frac{\rho_f{}^2 \eta^2}{\rho^3 E}\right)\left(\frac{L}{bh^2}\right)\right]^{1/4} \frac{2+a/h}{\sqrt{a/h}} \tag{3-22c}$$

In the results section of the dissertation (Ch. 5) the validity of these approximations will be confirmed via comparison with the values extracted from the frequency response curves of both the SDOF model [Eq. (3-20)] and the continuous forced-vibration model (Ch. 4) and, in some cases, with experimental data.

CHAPTER 4:

MULTI-MODAL CONTINUOUS-SYSTEM MODELING OF THE ASID

4.1. Introduction

Chapter 4 is devoted to a more general and more accurate analytical approach to the dynamic modeling of the ASID through the use of a continuous-system (distributed-parameter) model. This generalized continuous-system modeling approach is capable of simulating multi-modal response which, unlike the SDOF modeling described in Ch. 3, enables one to explore higher modes of vibration of the ASID. The mathematical formulations in this chapter involve the derivation of the boundary value problems (BVPs) governing the in-fluid axial vibration of the support legs for free- and forced-vibration cases, taking into account the disk effects via a boundary condition on each leg. Solutions of the BVPs lead to the frequency equation (free-vibration case) and steady-state response (forced-vibration case [88, 89]) of the system, from which one may determine, respectively, the eigenproperties and resonant characteristics of the ASID. These results will include the natural and resonant frequencies and the free- and forced-vibration quality factors for modes 1 and higher which can be related to the geometric and material parameters of the system, including the fluid properties.

4.2. Modeling Assumptions

In the continuous-system model the supporting legs are treated as axial members (i.e., bending and twisting are neglected) as was the case in the SDOF model. However, in the present model the distributed nature of the mass, stiffness, and fluid resistance associated with the legs will be accounted for, i.e., assumption 4 of Sect. 3.2 will be relaxed. The fluid resistance on the legs will be modeled by utilizing the Stokes results of Eqs. (3-4a-c). All other assumptions of Sect. 3.2 remain unchanged.

4.3. Mathematical Formulation and Solution for the Free-Vibration Case

The boundary value problem governing the axial, free vibration of the leg, with the disk (inertial and fluid) effects incorporated into a boundary condition as a frequency-dependent axial force exerted on the leg, may be derived by performing a force balance on an infinitesimal element of the leg. The governing equation of motion is accompanied by two boundary conditions associated with the fixed condition at one end and the axial force exerted by the disk at the other end.

4.3.1. Derivation of the Dimensional BVP Governing the Free Vibration of the Legs Including Disk Effects

An equilibrium analysis of an infinitesimal element of length *dx* of an individual leg, shown in Fig. 4-1, results in a partial differential equation that governs the axial vibration of the leg in fluid:

$$\left[\rho bh+2\bar{\bar{m}}_f\left(b+h\right)\right]\ddot{u}\left(x,t\right)+2\bar{\bar{c}}_f\left(b+h\right)\dot{u}\left(x,t\right)-bh\sigma'(x,t)=0 \qquad (4\text{-}1)$$

where $u(x,t)$ and $\sigma(x,t)$ are the axial displacement and axial stress in the leg and the prime notation indicates differentiation with respect to *x*, where the coordinate *x* is defined in Fig. 4-1. The fluid resistance terms in (4-1) involving $\bar{\bar{m}}_f$ and $\bar{\bar{c}}_f$ are obtained through the direct application of the resisting shear stress exerted by the fluid expressed

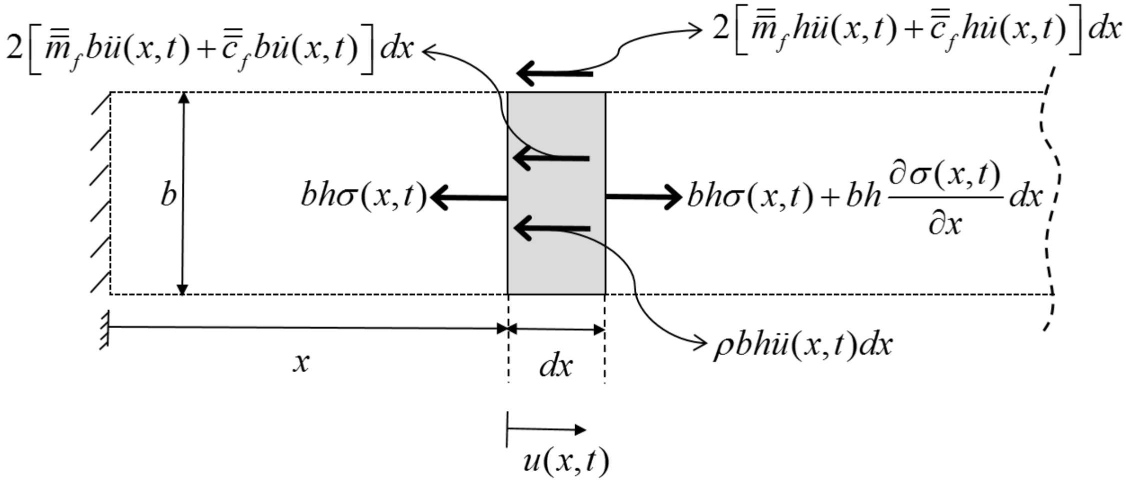

Fig. 4-1. Free body diagram of an infinitesimal element of the leg vibrating in fluid

in (3-4a). The axial stress in the leg is related to the strain through Hooke's law:

$$\sigma(x,t)=E\varepsilon(x,t)=Eu'(x,t) \tag{4-2}$$

By substituting (4-2) into (4-1), the equation of motion governing the axial deformation of the leg in a viscous fluid takes the following form:

$$\left[\rho bh+2\bar{\bar{m}}_f\left(b+h\right)\right]\ddot{u}\left(x,t\right)+2\bar{\bar{c}}_f\left(b+h\right)\dot{u}\left(x,t\right)-Ebhu''\left(x,t\right)=0 \tag{4-3}$$

Two boundary conditions reflecting the physical conditions at the ends of the leg must accompany the equation of motion (4-3). The fixed condition at $x=0$ is given by

$$u\left(0,t\right)=0 \tag{4-4}$$

and the second boundary condition (at $x=L$) is associated with the axial force, *F*, exerted by the disk on the leg at the disk-leg junction. In terms of axial stress at that location, we have $\sigma(L,t)=F/bh$, which may be written in terms of the axial strain in the leg using (4-2):

$$u'(L,t) = \frac{F}{Ebh} \tag{4-5}$$

A detailed expression for the axial force F exerted by the disk on the leg can be obtained by performing a moment equilibrium analysis of the disk in liquid, as indicated in Fig. 3-3, ignoring the transverse force and moment reactions as they were found in Sect. 3.3.3 to be of higher order. Using the kinematic relationship between the (small) disk rotation and the axial displacement at the end of the leg, i.e., $\theta(t) = u\left(L,t\right)/a$, and rotational equilibrium of the free-body diagram of Fig. 3-3, this force may be expressed as follows:

$$F = -\frac{\pi}{4}\rho h a^2 \left\{ \left[1 + \left(1 + \frac{2h}{a}\right)\sqrt{\frac{2\rho_f \eta}{\rho^2 h^2 \omega}} \right] \ddot{u}\left(L,t\right) + \left(1 + \frac{2h}{a}\right)\sqrt{\frac{2\rho_f \eta \omega}{\rho^2 h^2}} \dot{u}\left(L,t\right) \right\} \tag{4-6}$$

The explicit form of the second boundary condition can therefore be obtained by placing (4-6) into (4-5):

$$\frac{\pi}{4}\frac{\rho a^2}{Eb} \left\{ \left[1 + \left(1 + \frac{2h}{a}\right)\sqrt{\frac{2\rho_f \eta}{\rho^2 h^2 \omega}} \right] \ddot{u}\left(L,t\right) + \left(1 + \frac{2h}{a}\right)\sqrt{\frac{2\rho_f \eta \omega}{\rho^2 h^2}} \dot{u}\left(L,t\right) \right\} + u'(L,t) = 0 \tag{4-7}$$

Equations (4-3), (4-4), and (4-7) constitute the governing BVP for the free vibration of the continuous-system model. The frequency-dependent terms in (4-7) that are proportional to $\ddot{u}(L,t)$ and $\dot{u}(L,t)$ correspond, respectively, to the portions of the end force due to (a) the rotational inertia of the fluid dragged by the disk and (b) the viscous torque exerted by the fluid on the disk. (See Fig. 3-3.)

4.3.2. Dimensionless BVP Governing the Free Vibration of the Legs Including Disk Effects

The dimensional boundary value problem obtained in the previous section may be written in terms of the normalized axial displacement, $\bar{u} \equiv u/L$, as a function of the dimensionless axial coordinate, $\xi \equiv x/L$, and dimensionless time, $\bar{t} \equiv \omega_0 t$, in which the reference frequency ω_0 is defined by (3-9d):

$$\bar{u}''(\xi,\bar{t}) - \frac{\pi^{3/2}}{2}\sqrt{\bar{L}_0\bar{L}}\left(1+\frac{1}{\bar{b}}\right)\sqrt{\bar{\omega}}\;\dot{\bar{u}}(\xi,\bar{t}) - \frac{\pi^2}{4}\left[1+\frac{2}{\sqrt{\pi}}\sqrt{\bar{L}_0\bar{L}}\left(1+\frac{1}{\bar{b}}\right)\frac{1}{\sqrt{\bar{\omega}}}\right]\ddot{\bar{u}}(\xi,\bar{t}) = 0, \tag{4-8a}$$

$$\bar{u}(0,\bar{t}) = 0, \tag{4-8b}$$

$$\bar{u}'(1,\bar{t}) + \frac{\pi^3}{16}\frac{\bar{a}^2}{\bar{b}\,\bar{L}}\left\{\frac{2}{\sqrt{\pi}}\sqrt{\bar{L}_0\bar{L}}\left(1+\frac{2}{\bar{a}}\right)\sqrt{\bar{\omega}}\;\dot{\bar{u}}(1,\bar{t}) + \left[1+\frac{2}{\sqrt{\pi}}\sqrt{\bar{L}_0\bar{L}}\left(1+\frac{2}{\bar{a}}\right)\frac{1}{\sqrt{\bar{\omega}}}\right]\ddot{\bar{u}}(1,\bar{t})\right\} = 0. \tag{4-8c}$$

Primes and dots denote differentiation with respect to ξ and $\bar{t}$, respectively, and the following dimensionless parameters are defined:

$\bar{\omega} \equiv \omega / \omega_0$ = normalized natural frequency (4-9a)

$\bar{a} \equiv a / h$ = normalized disk radius (4-9b)

$\bar{b} \equiv b/h$ = normalized leg width (4-9c)

$\bar{L} \equiv L/h$ = normalized leg length (4-9d)

$$\bar{L}_0 \equiv L_0/h \equiv \sqrt{\rho_f{}^2\eta^2 / E\rho^3}\Big/h = \text{normalized “characteristic material length”} \qquad \text{(4-9e)}$$

Parameter L_0 incorporates all of the model’s material properties and its normalized counterpart, $\bar{L}_0$, is the only material-dependent system parameter appearing in the BVP (4-8a-c).

Note that the equation of motion (3-10) of the SDOF model can also be derived directly from the boundary condition (4-8c), so that the SDOF model may be viewed as a special case of the continuous-system model. For the SDOF model the disk rotation, $\theta = \theta(\bar{t})$, is the only degree of freedom of the system, and the displacement field in the legs is given by

$$\bar{u}(\xi, \bar{t}) = \frac{a\theta(\bar{t})}{L}\xi \qquad \text{(4-10)}$$

Substituting (4-10) into (4-8c) and rewriting the results in terms of the dimensionless parameters introduced in Ch. 3 results in the SDOF equation of motion (3-10).

4.3.3. In-Fluid Solution to the Governing BVP: Damped Natural Frequency, Decay Parameter, and Quality Factor

In order to obtain the solution of the general in-fluid BVP described by (4-8a-c) the following solution form is considered:

$$\bar{u}\left(\xi, \bar{t}\right) = X\left(\xi\right)T\left(\bar{t}\right) \qquad \text{(4-11)}$$

The dimensional time-dependent component is assumed to be of the harmonic form of $T(t) = e^{i\Omega t}$, where $\Omega = \omega + i\delta$ is the (unknown) complex natural frequency, in which ω and δ are the oscillation frequency (i.e., the damped natural frequency) and the decay parameter of the system, respectively. This dimensional time-dependent function may be converted into the following non-dimensional form:

$$T\left(\bar{t}\right) = e^{i\bar{\Omega}\bar{t}} \tag{4-12}$$

where

$$\bar{\Omega} = \bar{\omega} + i\bar{\delta} \tag{4-13}$$

is the normalized complex natural frequency and $\bar{\omega} = \omega / \omega_0$ and $\bar{\delta} = \delta / \omega_0$ are scaled by the reference frequency defined by (3-9d). Placing (4-12) and (4-13) into (4-11), and then substituting the result into the BVP (4-8a-c) yields the following ordinary differential equation and its two boundary conditions:

$$X'' + \lambda_1^2 X = 0 \tag{4-14a}$$

$$X\left(0\right) = 0 \tag{4-14b}$$

$$X'\left(1\right) - \lambda_2 X\left(1\right) = 0 \tag{4-14c}$$

where

$$\lambda_1 = \frac{\pi}{2}\left[\left(\bar{\varpi}^2 + \beta\bar{\varpi}^{3/2} + \beta\sqrt{\bar{\varpi}}\bar{\delta} - \frac{\beta}{\sqrt{\bar{\varpi}}}\bar{\delta}^2 - \bar{\delta}^2\right) + i\left(-\beta\bar{\varpi}^{3/2} + 2\bar{\varpi}\bar{\delta} + 2\beta\sqrt{\bar{\varpi}}\bar{\delta}\right)\right]^{1/2},$$

$$\lambda_2 = \frac{\pi^3}{16}\alpha\left[\left(\bar{\varpi}^2 + \Delta\beta\bar{\varpi}^{3/2} + \Delta\beta\sqrt{\bar{\varpi}}\bar{\delta} - \frac{\Delta\beta}{\sqrt{\bar{\varpi}}}\bar{\delta}^2 - \bar{\delta}^2\right) + i\left(-\Delta\beta\bar{\varpi}^{3/2} + 2\bar{\varpi}\bar{\delta} + 2\Delta\beta\sqrt{\bar{\varpi}}\bar{\delta}\right)\right],$$

$$\beta \equiv \frac{2}{\sqrt{\pi}}\left(1 + \frac{1}{\bar{b}}\right)\sqrt{\bar{L}_0\bar{L}}\ ,$$

$$\alpha = \frac{\bar{a}^2}{\bar{b}\bar{L}},$$

$$\Delta = \frac{1 + 2/\bar{a}}{1 + 1/\bar{b}}.$$

$$\text{(4-15a-e)}$$

Solving (4-14a) and imposing the first boundary condition (4-14b) leads to the following form of the free-vibration response of the system in fluid:

$$\bar{u}\left(\xi, \bar{t}\right) = A\sin\left(\lambda_1\xi\right)e^{-\bar{\delta}\bar{t}}\left(\cos\bar{\varpi}\bar{t} + i\sin\bar{\varpi}\bar{t}\right) \tag{4-16}$$

where *A* is an arbitrary constant. Imposing the second boundary condition (4-14c) on the ξ–dependent component of (4-16) results in the in-fluid frequency equation governing the unknown values of $\bar{\varpi}$ and $\bar{\delta}$:

$$\lambda_1\cos\lambda_1 - \lambda_2\sin\lambda_1 = 0 \tag{4-17}$$

where $\lambda_1 = \lambda_1\left(\bar{\varpi}, \bar{\delta}\right)$ and $\lambda_2 = \lambda_2\left(\bar{\varpi}, \bar{\delta}\right)$ are complex-valued functions expressed in (4-15a) and (4-15b), respectively. Numerical solution of (4-17) yields the roots $\bar{\varpi}_n$ and $\bar{\delta}_n$

for the n^{th} mode, where the mode-1 pair ($\bar{\omega}_1$ and $\bar{\delta}_1$) is defined to be that corresponding to the smallest (positive) value of the in-fluid natural frequency ($\bar{\omega}_1$), the mode-2 pair ($\bar{\omega}_2$ and $\bar{\delta}_2$) to be that corresponding to the next highest value of the in-fluid natural frequency ($\bar{\omega}_2$), and so on. Details regarding how to calculate the roots of (4-17) will be given in Ch. 5.

Once the damped natural frequency and the decay parameter are determined for the modes of interest, one may calculate the corresponding damping ratios and quality factors. Comparing the time-dependent portion of (4-16) with the free-vibration response of a damped SDOF oscillator having a damped natural frequency ω and a damping ratio *d*, one may relate *d* and thus *Q* to the roots $\bar{\omega}_n$ and $\bar{\delta}_n$ for mode *n* of the continuous-system model:

$$Q_n \equiv \frac{1}{2d_n} = \frac{1}{2\left[\dfrac{\bar{\delta}_n/\bar{\omega}_n}{\sqrt{1+\left(\bar{\delta}_n/\bar{\omega}_n\right)^2}}\right]} = \frac{\sqrt{1+\left(\bar{\delta}_n/\bar{\omega}_n\right)^2}}{2\bar{\delta}_n/\bar{\omega}_n} \tag{4-18}$$

4.3.4. In-Vacuum Solution to the Governing BVP: Natural Frequency

A special case of the BVP (4-8a-c) for the general in-fluid model is the in-vacuum vibration of the ASID whose governing BVP can be deduced from (4-8a-c) by eliminating the terms that involve the fluid effects. Thus, the in-vacuum results of interest may be obtained directly from the in-fluid results of Sect. 4.3.3 by setting both the fluid resistance parameter, $\bar{L}_0$, and the decay parameter, $\bar{\delta}$, equal to zero. This leads to the in-vacuum frequency equation [from Eq. (4-17)],

$$\tan\left(\frac{\pi}{2}\bar{\omega}_{vac}\right)=\frac{2}{\pi}\frac{1}{\bar{\alpha}}\frac{1}{\bar{\omega}_{vac}},$$
$$\bar{\alpha}\equiv\frac{\pi}{4}\alpha. \tag{4-19a,b}$$

Equation (4-19a) may be solved numerically for specific values of $\bar{\alpha}$, yielding the roots, $\bar{\omega}_{n,vac}$ in terms of the single system parameter $\bar{\alpha}$. Having determined the normalized natural frequencies, the in-vacuum free-vibration response for the n^{th} mode becomes [see Eq. (4-16)]

$$\bar{u}_n\left(\xi,\bar{t}\right)=A_n\sin\left(\frac{\pi}{2}\bar{\omega}_{n,vac}\xi\right)e^{i\bar{\omega}_{n,vac}\bar{t}} \tag{4-20}$$

A_n being the arbitrary multiplier for mode *n*.

Analytical expressions for the natural frequencies may also be obtained by curve-fitting the exact in-vacuum natural frequency results, which are determined numerically. Note that, based on (4-19a), $\bar{\omega}_{\mathrm{n},vac}=2n-1$ at $\bar{\alpha}=0$, and $\bar{\omega}_{\mathrm{n},vac}\to 2\left(n-1\right)$ as $\bar{\alpha}\to\infty$ for an arbitrary mode *n*. These two conditions lead to the following proposed forms for $\bar{\omega}_{n,vac}$ as functions of $\bar{\alpha}$ and *n*:

$$\begin{cases}\bar{\omega}_{n,vac}=\dfrac{1}{\sqrt{1+c_n\bar{\alpha}}}, & n=1\\[2ex] \bar{\omega}_{n,vac}=2\left(n-1\right)+\dfrac{1}{\sqrt{1+2(2n-1)\bar{\alpha}+c_n\bar{\alpha}^2}}, & n>1\end{cases} \tag{4-21a, b}$$

where c_n is the mode-*n* fit parameter whose value is to be determined by curve-fitting. It should be noted that the proposed form for $\bar{\omega}_{n,vac}$ for modes 2 and higher, given by (4-21b), satisfies the correct slope condition at $\bar{\alpha}=0$ in addition to the aforementioned conditions at $\bar{\alpha}=0$ and as $\bar{\alpha}\to\infty$. Utilizing Eq. (4-19a), it may be easily shown that the initial slope of $\bar{\omega}_{\mathrm{n},vac}$ with respect to $\bar{\alpha}$ is $\left.\frac{d\bar{\omega}_{n,vac}}{\bar{\alpha}}\right|_{\bar{\alpha}=0}=-\left(2n-1\right)$ for an arbitrary mode. (Simply substitute the linearized form of $\bar{\omega}_{\mathrm{n},vac}=\left(2n-1\right)+k\bar{\alpha}$ into (4-19a) and take a derivative of the equation with respect to $\bar{\alpha}$ in order to obtain the initial slope, k.)

Values of the best-fit parameters for the first three modes over the range of $\bar{\alpha}=\left[0,500\right]$ are $c_1=2.466$, $c_2=23.71$, and $c_3=87.23$. Substituting these parameters into (4-21a, b) leads to the following approximate expressions for the normalized in-vacuum natural frequency of the ASID for the first three modes:

$$\begin{cases} \bar{\omega}_{1,vac}=\dfrac{1}{\sqrt{1+2.466\bar{\alpha}}}, \\ \bar{\omega}_{2,vac}=2+\dfrac{1}{\sqrt{1+6\bar{\alpha}+23.71\bar{\alpha}^2}}, \\ \bar{\omega}_{3,vac}=4+\dfrac{1}{\sqrt{1+10\bar{\alpha}+87.23\bar{\alpha}^2}}. \end{cases} \tag{4-22a-c}$$

A comparison of the curve-fitting results and the exact results for the first three modes is shown in Fig. 4-2 in which the in-vacuum natural frequency of the ASID is normalized by the in-vacuum natural frequency of a single leg of the corresponding mode (i.e., $\frac{\omega_{\mathrm{n},vac}}{\omega_{\mathrm{n},vac,leg}}=\frac{1}{2n-1}\frac{\omega_{\mathrm{n},vac}}{\omega_{1,vac,leg}}=\frac{1}{2n-1}\bar{\omega}_{\mathrm{n},vac}$).

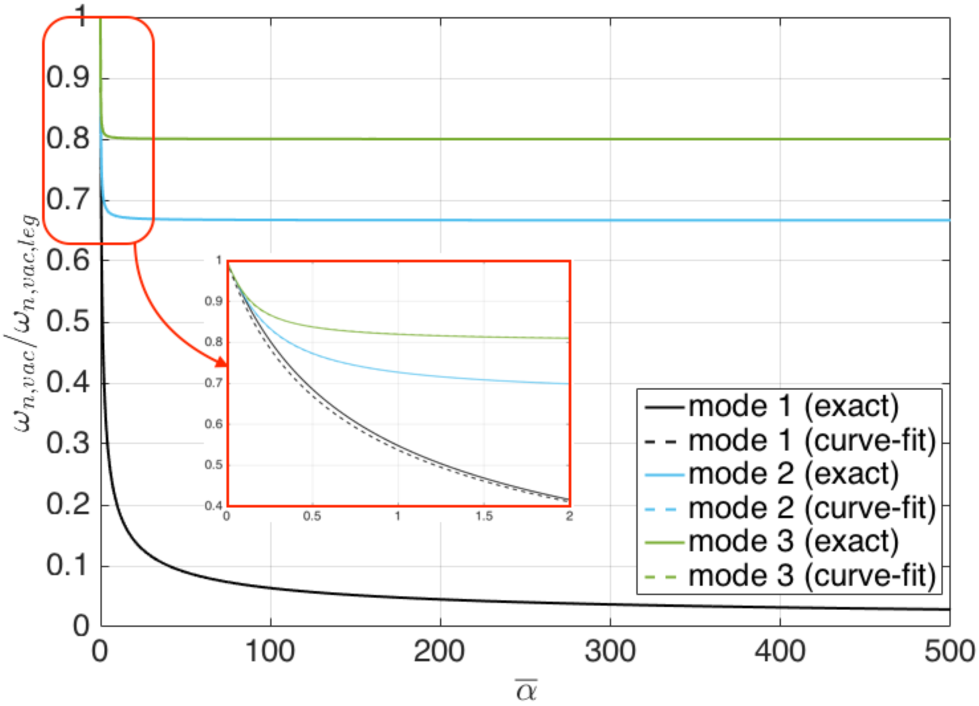

Fig. 4-2. Variation of the normalized in-vacuum natural frequency of the ASID with respect to the normalized disk area ($\bar{\alpha} \equiv \frac{\pi}{4}\frac{a^2}{bL}$): exact vs. curve-fit

Based on Fig. 4-2, the curve-fitting for the in-vacuum natural frequency of the ASID matches very well with the exact results with the maximum relative error being ~2.4% (occurring for mode 1 at $\bar{\alpha} \simeq 0.4$); therefore we will employ Eqs. (4-21a, b) in the following section to obtain an analytical solution to the general in-fluid frequency equation for the case of small fluid resistance.

4.3.5. Analytical Solution of the In-Fluid Frequency Equation Based on Small Fluid Resistance

Since in practical cases the fluid resistance parameter, β, defined in Eq. (4-15c), is much smaller than unity, one may wish to obtain an approximate analytical solution to the in-fluid frequency equation (4-17) by using Taylor series expansions of $\bar{\omega}$ and $\bar{\delta}$ in powers of β:

$$\bar{\omega} = \bar{\omega}_{vac} + a_1\beta + O\left(\beta^2\right) \quad \text{as} \quad \beta \to 0 \tag{4-23}$$

$$\bar{\delta} = b_1\beta + O\left(\beta^2\right) \quad \text{as} \quad \beta \to 0 \tag{4-24}$$

where a_1 and b_1 are unknown coefficients to be determined and the forms chosen reduce to the exact in-vacuum results when $\beta = 0$. Substituting (4-23) and (4-24) into (4-15a, b) yields

$$\begin{aligned} \lambda_1 &= \lambda_{1,0} + \lambda_{1,1}\beta + O(\beta^2) \quad \text{as} \quad \beta \to 0, \\ \lambda_2 &= \lambda_{2,0} + \lambda_{2,1}\beta + O(\beta^2) \quad \text{as} \quad \beta \to 0. \end{aligned} \tag{4-25a, b}$$

where

$$\begin{aligned} \lambda_{1,0} &= \frac{\pi}{2}\bar{\omega}_{vac}, & \lambda_{1,1} &= \frac{\pi}{2}\left[a_1 + \frac{\sqrt{\bar{\omega}_{vac}}}{2} + i\left(b_1 - \frac{\sqrt{\bar{\omega}_{vac}}}{2}\right)\right], \\ \lambda_{2,0} &= \frac{\pi^2}{4}\bar{\alpha}\bar{\omega}_{vac}{}^2, & \lambda_{2,1} &= \frac{\pi^2}{4}\bar{\alpha}\left[2\bar{\omega}_{vac}a_1 + \Delta\bar{\omega}_{vac}{}^{3/2} + i\left(2\bar{\omega}_{vac}b_1 - \Delta\bar{\omega}_{vac}{}^{3/2}\right)\right]. \end{aligned} \tag{4-26a-d}$$

Also, by using the Taylor series expansions for the sine and cosine functions about $\lambda_{1,0}$, we have

$$\begin{aligned} \cos\lambda_1 &= \cos\lambda_{1,0} - \lambda_{1,1}\beta\sin\lambda_{1,0} + O(\beta^2) \quad \text{as} \quad \beta \to 0, \\ \sin\lambda_1 &= \sin\lambda_{1,0} + \lambda_{1,1}\beta\cos\lambda_{1,0} + O(\beta^2) \quad \text{as} \quad \beta \to 0. \end{aligned} \tag{4-27a, b}$$

Substituting (4-25a, b) and (4-27a, b) into the frequency equation (4-17) results in

$$\begin{aligned}&\left(\lambda_{1,0}\cos\lambda_{1,0}-\lambda_{2,0}\sin\lambda_{1,0}\right)+\\&\left(-\lambda_{1,0}\lambda_{1,1}\sin\lambda_{1,0}+\lambda_{1,1}\cos\lambda_{1,0}-\lambda_{2,0}\lambda_{1,1}\cos\lambda_{1,0}-\lambda_{2,1}\sin\lambda_{1,0}\right)\beta+O(\beta^2)=0\end{aligned}\tag{4-28}$$

Setting the β - independent term (first term in parentheses) equal to zero results in the in-vacuum frequency equation that has already been derived and solved in the previous section [Eq. (4-19a)]. Setting the coefficient of the linear term in β equal to zero results in a complex-valued equation from which the unknown coefficients a_1 and b_1 may be determined by considering the real and imaginary parts, respectively:

$$\begin{cases}-\lambda_{1,0}\operatorname{Re}\left(\lambda_{1,1}\right)\sin\lambda_{1,0}+\operatorname{Re}\left(\lambda_{1,1}\right)\cos\lambda_{1,0}-\lambda_{2,0}\operatorname{Re}\left(\lambda_{1,1}\right)\cos\lambda_{1,0}-\operatorname{Re}\left(\lambda_{2,1}\right)\sin\lambda_{1,0}=0\\-\lambda_{1,0}\operatorname{Im}\left(\lambda_{1,1}\right)\sin\lambda_{1,0}+\operatorname{Im}\left(\lambda_{1,1}\right)\cos\lambda_{1,0}-\lambda_{2,0}\operatorname{Im}\left(\lambda_{1,1}\right)\cos\lambda_{1,0}-\operatorname{Im}\left(\lambda_{2,1}\right)\sin\lambda_{1,0}=0\end{cases}\tag{4-29a, b}$$

Placing (4-26a-d) into (4-29a) yields

$$a_1=-\frac{\sqrt{\bar{\omega}_{vac}}}{2}\,\frac{1-\dfrac{\pi}{2}\bar{\omega}_{vac}\tan\left(\dfrac{\pi}{2}\bar{\omega}_{vac}\right)\left(1+2\bar{\alpha}\Delta\right)-\dfrac{\pi^2}{4}\bar{\alpha}\bar{\omega}_{vac}{}^2}{1-\dfrac{\pi}{2}\bar{\omega}_{vac}\tan\left(\dfrac{\pi}{2}\bar{\omega}_{vac}\right)\left(1+2\bar{\alpha}\right)-\dfrac{\pi^2}{4}\bar{\alpha}\bar{\omega}_{vac}{}^2}\tag{4-30}$$

Substituting (4-19a) into (4-30) leads to

$$a_1=-\sqrt{\frac{\bar{\omega}_{vac}}{4}}\left[\frac{1+(2\Delta-1)\bar{\alpha}+\dfrac{\pi^2}{4}\bar{\alpha}^2\bar{\omega}_{vac}{}^2}{1+\bar{\alpha}+\dfrac{\pi^2}{4}\bar{\alpha}^2\bar{\omega}_{vac}{}^2}\right]\tag{4-31}$$

and placing (4-26a-d) into (4-29b) results in

$$b_1 = \sqrt{\frac{\bar{\omega}_{vac}}{4}}\left[\frac{1+(2\Delta-1)\bar{\alpha}+\frac{\pi^2}{4}\bar{\alpha}^2\bar{\omega}_{vac}{}^2}{1+\bar{\alpha}+\frac{\pi^2}{4}\bar{\alpha}^2\bar{\omega}_{vac}{}^2}\right] = -a_1 \tag{4-32}$$

Now that the coefficients a_1 and b_1 are determined, expansions (4-23) and (4-24) yield the following approximate analytical expressions for the damped natural frequency and the decay parameter for the n$^{\text{th}}$ mode:

$$\bar{\omega}_n \simeq \bar{\omega}_{n,vac} - \sqrt{\frac{\bar{\omega}_{n,vac}}{4}}\left[\frac{1+(2\Delta-1)\bar{\alpha}+\frac{\pi^2}{4}\bar{\alpha}^2\bar{\omega}_{n,vac}{}^2}{1+\bar{\alpha}+\frac{\pi^2}{4}\bar{\alpha}^2\bar{\omega}_{n,vac}{}^2}\right]\beta \tag{4-33}$$

$$\bar{\delta}_n \simeq \sqrt{\frac{\bar{\omega}_{n,vac}}{4}}\left[\frac{1+(2\Delta-1)\bar{\alpha}+\frac{\pi^2}{4}\bar{\alpha}^2\bar{\omega}_{n,vac}{}^2}{1+\bar{\alpha}+\frac{\pi^2}{4}\bar{\alpha}^2\bar{\omega}_{n,vac}{}^2}\right]\beta \tag{4-34}$$

Once the damped natural frequency and the decay parameter are determined, one may use Eq. (4-18) to calculate the quality factor:

$$Q_n = \frac{\sqrt{1+\left(\bar{\delta}_n / \bar{\omega}_n\right)^2}}{2\bar{\delta}_n / \bar{\omega}_n} = \sqrt{\bar{\omega}_{n,vac}}\left[\frac{1+\bar{\alpha}+\frac{\pi^2}{4}\bar{\alpha}^2\bar{\omega}_{n,vac}{}^2}{1+(2\Delta-1)\bar{\alpha}+\frac{\pi^2}{4}\bar{\alpha}^2\bar{\omega}_{n,vac}{}^2}\right]\frac{1}{\beta} + O(1) \quad \text{as} \quad \beta \to 0 \tag{4-35}$$

Therefore, an approximate expression for Q_n in terms of the system parameters can be written as

$$Q_n \simeq \sqrt{\bar{\omega}_{n,vac}}\left[\frac{1+\bar{\alpha}+\frac{\pi^2}{4}\bar{\alpha}^2\bar{\omega}_{n,vac}{}^2}{1+(2\Delta-1)\bar{\alpha}+\frac{\pi^2}{4}\bar{\alpha}^2\bar{\omega}_{n,vac}{}^2}\right]\frac{1}{\beta} \tag{4-36}$$

Equations (4-33) and (4-36) imply that the (approximate) inverse relationship between the fluid-induced relative shift in natural frequency and the quality factor of the ASID, listed in Eq. (3-14) for the fundamental mode of the SDOF model, is true for any mode *n* of the continuous model. This is most likely due to the use of the Stokes fluid resistance model in both analytical models.

The approximate expressions for the in-vacuum natural frequency of the ASID, Eq. (4-21a, b), may now be used to obtain the analytical expressions for the damped natural frequency, the decay parameter, and the quality factor for any mode of interest. However, since the fundamental mode is of most interest in this case, we will write out the mode-1 results explicitly by substituting Eq. (4-22a) into Eqs. (4-33), (4-34), and (4-36) and rewriting the results as follows:

$$\bar{\omega}_1 \simeq \frac{1}{\sqrt{1+2.466\bar{\alpha}}} - \frac{1}{2\left(1+2.466\bar{\alpha}\right)^{1/4}}\left[\frac{1+(2\Delta-1)\bar{\alpha}+\frac{\pi^2}{4}\frac{\bar{\alpha}^2}{\left(1+2.466\bar{\alpha}\right)}}{1+\bar{\alpha}+\frac{\pi^2}{4}\frac{\bar{\alpha}^2}{\left(1+2.466\bar{\alpha}\right)}}\right]\beta \quad (4\text{-}37)$$

$$\bar{\delta}_1 \simeq \frac{1}{2\left(1+2.466\bar{\alpha}\right)^{1/4}}\left[\frac{1+(2\Delta-1)\bar{\alpha}+\frac{\pi^2}{4}\frac{\bar{\alpha}^2}{\left(1+2.466\bar{\alpha}\right)}}{1+\bar{\alpha}+\frac{\pi^2}{4}\frac{\bar{\alpha}^2}{\left(1+2.466\bar{\alpha}\right)}}\right]\beta \quad (4\text{-}38)$$

$$Q_1 \simeq \frac{1}{\left(1+2.466\bar{\alpha}\right)^{1/4}}\left[\frac{1+\bar{\alpha}+\frac{\pi^2}{4}\frac{\bar{\alpha}^2}{\left(1+2.466\bar{\alpha}\right)}}{1+(2\Delta-1)\bar{\alpha}+\frac{\pi^2}{4}\frac{\bar{\alpha}^2}{\left(1+2.466\bar{\alpha}\right)}}\right]\frac{1}{\beta} \quad (4\text{-}39)$$

where the definitions of β, $\bar{\alpha}$, and Δ in terms of the basic system parameters are given by Eqs. (4-15c-e) in conjunction with (4-19b).

For illustrative purposes, approximate analytical results for the first three modes for a silicon-based ASID of specific dimensions, immersed in heptane, are shown in Figs. 4-3, 4-4, and 4-5, along with the “exact” results. (Heptane was chosen simply because this liquid was used in recent experiments by another group [24].) The approximate analytical results are based on Eqs. (4-33), (4-34), and (4-36) [with $\bar{\omega}_{n,vac}$ being approximated using Eqs. (4-22a-c)], while the “exact” results are obtained by solving the frequency equation (4-17) numerically.

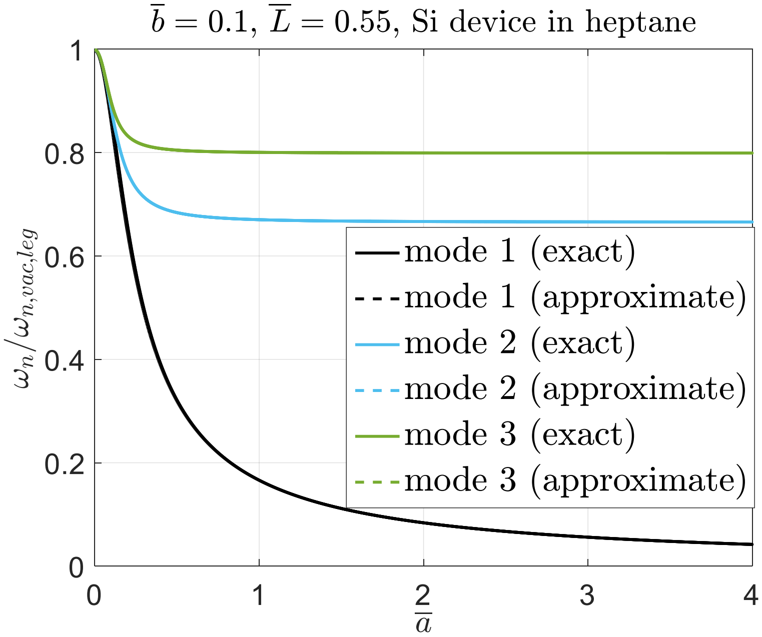

Fig. 4-3. Normalized damped natural frequency of a Si ASID ($\rho = 2330$ kg/m^3, $E = 130$ GPa) in heptane ($\rho_f = 679.5$ kg/m^3, $\eta = 0.000386$ Pa.s): Approximate analytical results, Eq. (4-33), vs. exact results.

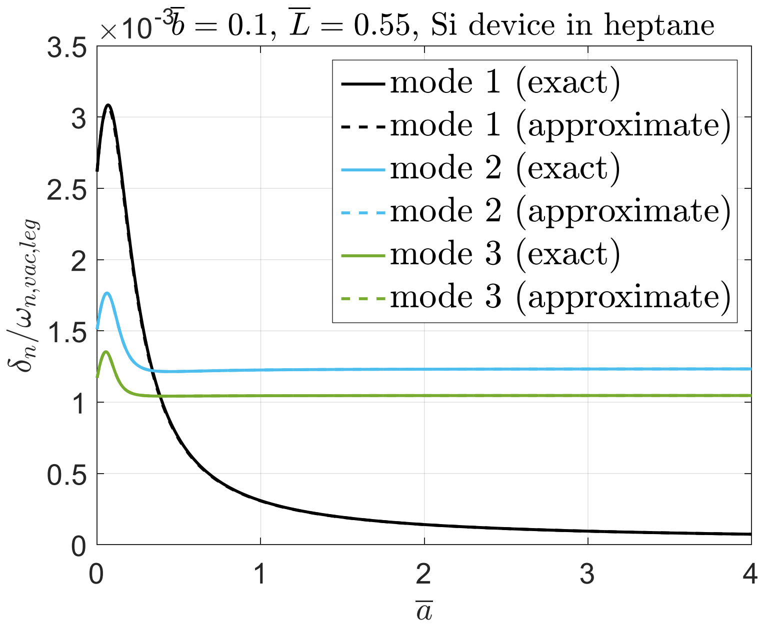

Fig. 4-4. Normalized decay parameter of a Si ASID ($\rho = 2330$ kg/m^3, $E = 130$ GPa) in heptane ($\rho_f = 679.5$ kg/m^3, $\eta = 0.000386$ Pa.s): Approximate analytical results, Eq. (4-34), vs. exact results.

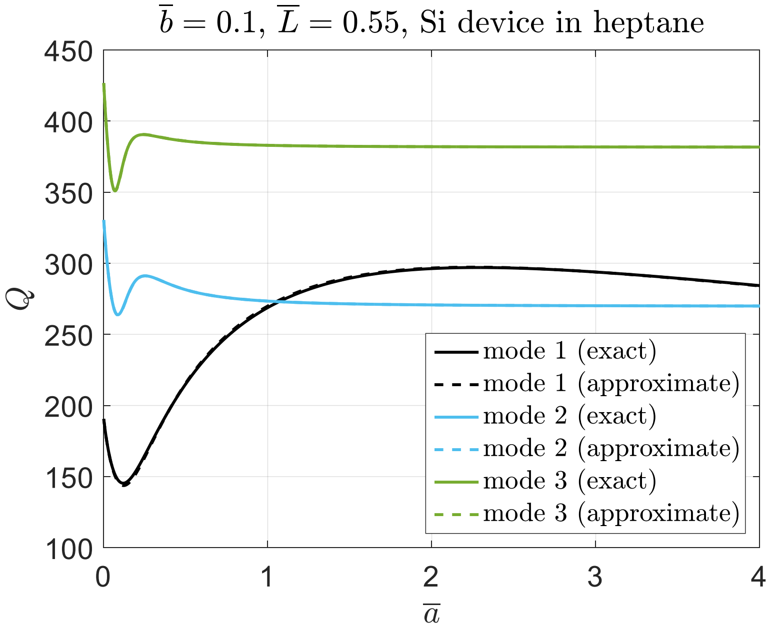

Fig. 4-5. Quality factor of a Si ASID ($\rho = 2330$ kg/m^3, $E = 130$ GPa) in heptane ($\rho_f = 679.5$ kg/m^3, $\eta = 0.000386$ Pa.s): Approximate analytical results, Eq. (4-36), vs. exact results.

Note that the approximate analytical results exhibit excellent accuracy in Figs. 4-3, 4-4, and 4-5. We also remark that these plots suggest that all three plotted quantities exhibit a uniform asymptotic behavior as the disk size increases. In particular, the following asymptotic formulae for the damped natural frequency, the decay parameter, and the quality factor can be obtained by taking limits of Eqs. (4-33), (4-34), and (4-36), respectively, as $\bar{\alpha} \to \infty$:

$$\lim_{\bar{\alpha}\to\infty}\left(\frac{\omega_n}{\omega_{n,vac,leg}}\right) = \frac{1}{(2n-1)}\left[2(n-1) - \frac{1}{\sqrt{2}}\sqrt{n-1}\beta\right] \tag{4-40}$$

$$\lim_{\bar{\alpha}\to\infty}\left(\frac{\delta_n}{\omega_{n,vac,leg}}\right) = \frac{1}{\sqrt{2}}\frac{\sqrt{n-1}}{(2n-1)}\beta \tag{4-41}$$

$$\lim_{\bar{\alpha}\to\infty} Q_n = \sqrt{2}\frac{\sqrt{n-1}}{\beta} \tag{4-42}$$

We note that these three asymptotic formulae are approximate in the sense that they are based on the linearized forms (in β) for the in-fluid natural frequency and decay parameter [Eqs. (4-33) and (4-34)].

While the results shown in Figs. (4-3) - (4-5) are for specific material properties (silicon and heptane properties in this case), one may present them in a more general way that is independent of the ASID material and the ambient fluid. For that purpose, the "material-normalized" vacuum-to-fluid relative frequency shift, $\frac{(\bar{\omega}_{n,vac} - \bar{\omega}_n)/\bar{\omega}_{n,vac}}{\beta}$, and the "material-normalized" quality factor, βQ, being functions of $\bar{\alpha}$ and Δ (or $\bar{a}$, $\bar{b}$, and $\overline{L}$) only, are plotted with respect to the normalized disk radius as shown in Figs. 4-6 and 4-7:

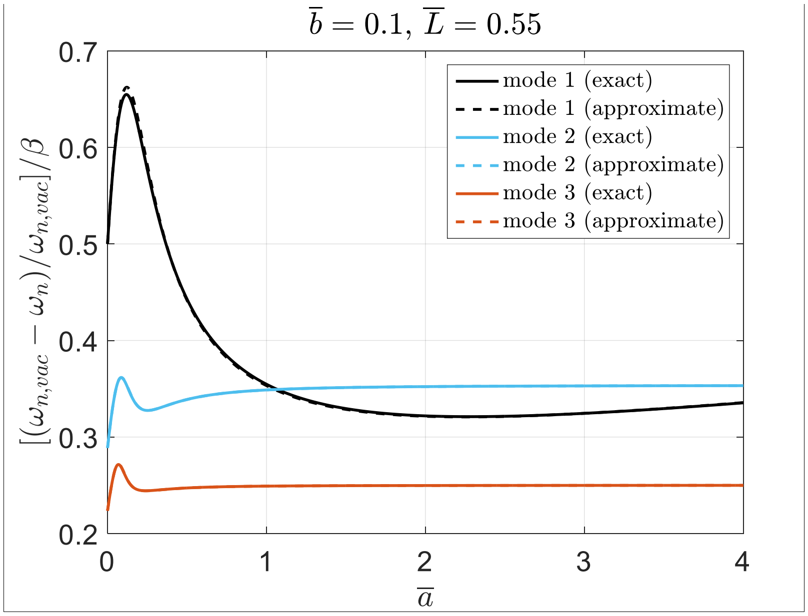

Fig. 4-6. Material-normalized relative frequency shift of the ASID: Approximate analytical results vs. exact results.

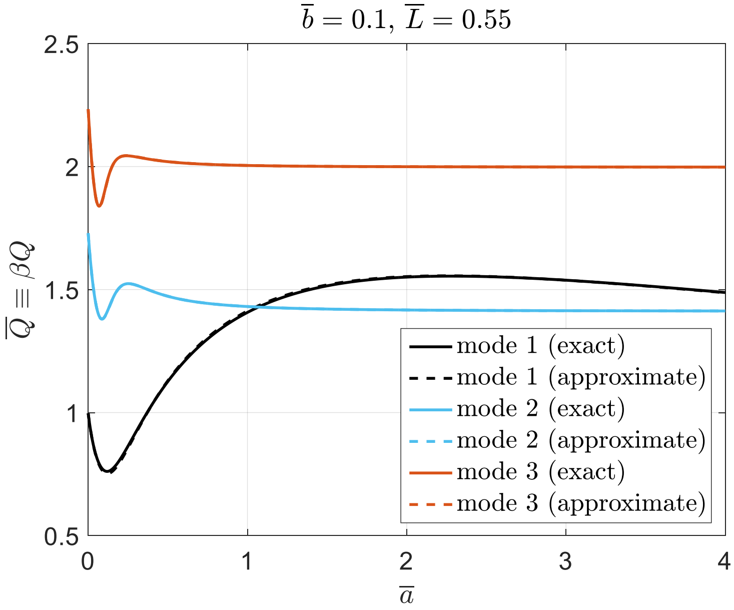

Fig. 4-7. Material-normalized quality factor of the ASID: Approximate analytical results vs. exact results.

The material-normalized quality factor results of the ASID for the first three modes, shown in Fig. 4-7, indicate that, for the leg dimensions considered in the figure, the fundamental mode yields higher Q values than mode 2 for a specific range of $\bar{a}$ values within which the relative maximum in Q occurs. However, for small values of $\bar{a}$, including the special "no-disk case" (theoretical details for this case will appear in the next section), the quality factor of the ASID increases as the mode number is increased. The same is true for sufficiently large disk radii [not shown in Fig. 4-7 but demonstrated analytically through the asymptotic limit given by Eq. (4-42)]. Finally, one may make analogous comments regarding the behavior of the material-normalized relative frequency shift shown in Fig. 4-6 due to the inverse relationship that exists between the two ordinate quantities of Figs. 4-6 and 4-7. [See Eq. (3-14) and the commentary following Eq. (4-36).]

While the graphical results presented in this section have been limited to specific cases (i.e., the leg dimensions and/or the material properties being fixed), a more exhaustive parametric study of the performance of the ASID, including the effects of all the system parameters along with the corresponding discussion of the results, will be included in Ch. 5. Moreover, the approximate expressions for the resonant characteristics of the ASID obtained in this section will also be employed in Ch. 6 in which the sensing metrics of the device will be explored analytically and expressed explicitly in terms of the basic system parameters.

4.3.6. In-Fluid Vibration of a Single Leg (No-Disk Case)

Axial vibration of a single leg in fluid without the presence of the disk (i.e., a fixed-free leg) is another special case of the general BVP (4-8a-c) and its associated solution. However, given the fundamental importance of this special case, the present section will be dedicated to a separate presentation of the in-fluid axial vibration of a cantilever. The analytical results obtained herein will enable us to estimate the in-fluid eigenproperties of an axial-mode microcantilever in terms of geometric and material parameters, including the properties of the fluid. Such results could be useful in making comparisons between axial-mode cantilevers and other types of microcantilever-based devices, i.e., those operated in the flexural (transverse or lateral) and torsional modes. The results summarized in this section may also be used to ascertain to what extent the presence of the disk, besides providing a potentially larger sensing area, will improve or detract from the resonator performance of the ASID in liquid environments.

We note that the analytical results of Sect. 4.3.5 for the resonant characteristics of the ASID for the case of small fluid resistance do, in fact, include the no-disk solution as a special case (when the disk radius a – or parameter $\bar{\alpha}$ – is set equal to zero). [Recall that the normalized in-vacuum natural frequency in Eqs. (4-33), (4-34), and (4-36) has an exact value at $\bar{\alpha} = 0$; therefore, the no-disk case for these expressions would be approximate only by virtue of the linearization with respect to the fluid resistance parameter, β.] However, in a portion of what follows, a separate formulation for this special case will be performed for two reasons: (1) as will be shown shortly, the analytical solution to the no-disk frequency equation will lead to a better approximation of the normalized decay parameter, $\bar{\delta}_n$, as a function of β (i.e., a quadratic form in β); and (2) it will enable us to study the eigenproperties of this special case analytically over a broader range of β. (Detailed numerical results will be presented in Sect. 5.2.4 of the next chapter.)

4.3.6.1. Frequency Equation for the No-Disk Case

The governing BVP for the no-disk case may be deduced from (4-8a-c) by setting the disk parameter $\bar{a}$ equal to zero in the second boundary condition (4-8c). While the resulting BVP could be solved directly, we will instead specialize the general solution that has already been obtained in Sect. 4.3.3. The response solution will have the same general form as (4-16); however, the frequency equation [(4-17) with (4-15a,b)] that determines the damped natural frequency and decay parameter for all modes will become much more simplified than for the general case of the ASID. Setting $\bar{a} = 0$ in (4-15b) results in parameter λ_2 vanishing; thus, the frequency equation (4-17) for the no-disk case reduces to

$$\lambda_1 \cos \lambda_1 = 0 \tag{4-43}$$

where λ_1 is defined in (4-15a). Considering that $\lambda_1 = 0$ gives the trivial solution of (4-43) and that $\cos\lambda_1 = 0$ yields positive, real roots $\left(\lambda_1\right)_n = \dfrac{\left(2n-1\right)\pi}{2}$, the final form of the in-fluid frequency equation for a single leg may be written as

$$\left(\bar{\omega}_n^{\,2}+\beta\bar{\omega}_n^{\,3/2}+\beta\sqrt{\bar{\omega}_n}\bar{\delta}_n-\frac{\beta}{\sqrt{\bar{\omega}_n}}\bar{\delta}_n^{\,2}-\bar{\delta}_n^{\,2}\right)+i\left(-\beta\bar{\omega}_n^{\,3/2}+2\bar{\omega}_n\bar{\delta}_n+2\beta\sqrt{\bar{\omega}_n}\bar{\delta}_n\right)=\left(2n-1\right)^2 \tag{4-44}$$

where β is defined in (4-15c). For given values of the leg and fluid parameters Eq. (4-44) may be solved numerically for $\bar{\omega}_n$ and $\bar{\delta}_n$ for the modes of interest; however, an analytical approach to solving this equation will be explored in the following section.

4.3.6.2. Analytical Solution for the No-Disk Case: Damped Natural Frequency, Decay Parameter, and Quality Factor

Approximate analytical expressions for the damped natural frequency and the decay parameter for the no-disk case, governed by (4-44), can be achieved by employing Taylor's series expansions of $\bar{\omega}_n$ and $\bar{\delta}_n$. By considering the imaginary part of (4-44) one may write $\bar{\delta}_n$ in terms of $\bar{\omega}_n$:

$$\bar{\delta}_n=\frac{\beta\bar{\omega}_n}{2\left(\sqrt{\bar{\omega}_n}+\beta\right)} \tag{4-45}$$

Substituting (4-45) into the real part of (4-44), the following frequency equation for the damped natural frequency can be derived for the no-disk case:

$$\bar{\omega}_n^{\,2}+\beta\bar{\omega}_n^{\,3/2}\left[1+\frac{\beta}{4\left(\sqrt{\bar{\omega}_n}+\beta\right)}\right]=\left(2n-1\right)^2 \tag{4-46}$$

When β is sufficiently small, an estimate of $\bar{\omega}_n$ may be determined by assuming that $\bar{\omega}_n$ is expressible as a Taylor's series expansion in powers of β. This leads to the following result:

$$\bar{\omega}_n \equiv \frac{\omega_n}{\omega_0} = \left(2n-1\right) - \frac{\sqrt{2n-1}}{2}\beta + O\left(\beta^2\right) \quad \text{as} \quad \beta \to 0 \tag{4-47}$$

Note that the approximate linear form for $\bar{\omega}_n$ in terms of β, given by the truncated form of (4-47), is consistent with the specialized form of the general result given by (4-33) when the disk size is set equal to zero. Substituting (4-47) into (4-45) yields the following Taylor's series expansion for the decay parameter, $\bar{\delta}_n$:

$$\bar{\delta}_n \equiv \frac{\delta_n}{\omega_0} = \frac{\sqrt{2n-1}}{2}\beta - \frac{5}{8}\beta^2 + O\left(\beta^3\right) \quad \text{as} \quad \beta \to 0 \tag{4-48}$$

While the linear portion of (4-48) matches the general result of the ASID given by (4-34) when $\bar{a} = 0$, the quadratic expression for $\bar{\delta}_n$ as a function of β is expected to yield a better approximation, especially for increasing values of the fluid resistance parameter. Recall that $\omega_0 = \omega_{1,vac,leg}$ is the mode-1, in-vacuum natural frequency of an isolated leg, which has the following relationship to the in-vacuum natural frequency of higher modes:

$$\frac{\omega_{n,vac,leg}}{\omega_{1,vac,leg}} = 2n-1 \tag{4-49}$$

Should one wish to scale each in-fluid natural frequency and decay parameter by the in-vacuum natural frequency of its corresponding mode, we may write

$$\frac{\omega_n}{\omega_{n,vac,leg}} = \frac{\bar{\omega}_n}{2n-1} = 1 - \frac{1}{2\sqrt{2n-1}}\beta + O\left(\beta^2\right) \quad \text{as} \quad \beta \to 0 \tag{4-50}$$

$$\frac{\delta_n}{\omega_{n,vac,leg}} = \frac{\bar{\delta}_n}{2n-1} = \frac{1}{2\sqrt{2n-1}}\beta - \frac{5}{8\left(2n-1\right)}\beta^2 + O\left(\beta^3\right) \quad \text{as} \quad \beta \to 0 \tag{4-51}$$

Substituting (4-50) and (4-51) into (4-18) yields the quality factor of the leg vibrating axially in fluid:

$$Q_n = \frac{\sqrt{2n-1}}{\beta} + O\left(\beta^0\right) \quad \text{as} \quad \beta \to 0 \tag{4-52}$$

Therefore, the following approximations, obtained by truncating the foregoing expressions, can be used to estimate the damped natural frequency, the decay parameter, and the quality factor for small values of β; moreover, in these final results we introduce notation to explicitly show that these results apply to the no-disk case:

$$\frac{\omega_{n,leg}}{\omega_{n,vac,leg}} \approx 1 - \frac{1}{2\sqrt{2n-1}}\beta \tag{4-53}$$

$$\frac{\delta_{n,leg}}{\omega_{n,vac,leg}} \approx \frac{1}{2\sqrt{2n-1}}\beta - \frac{5}{8\left(2n-1\right)}\beta^2 \tag{4-54}$$

$$Q_{n,leg} \approx \frac{\sqrt{2n-1}}{\beta} \tag{4-55}$$

It should be emphasized that these approximate analytical results are equivalent to those that could have been obtained by specializing the general ASID results in Sect. 4.3.5 [with the exception of the quadratic term in (4-54)], which provides a check on these simpler results for the no-disk case. In Ch. 5 the approximate analytical results given by (4-53)-(4-55) will be compared with the “exact” results obtained by solving (4-44) numerically.

4.4. Mathematical Formulation and Solution for the Forced-Vibration Case

The formulation and solution of a continuous-system model for the forced-vibration response of the ASID are derived in this section. This will enable one to determine the resonant characteristics of the device in a viscous fluid and relate them to the system’s geometric and material parameters in order to optimize the resonator performance. The external input to the system is the same as that of the SDOF forced-vibration case described by assumption (9) in Sect. 3.2: the supporting legs are subjected to identical, harmonic eigenstrains which are uniform throughout the legs, i.e., $\varepsilon^*(t) = \varepsilon_0 e^{i\omega t}$ (for example, due to electrothermal loading). Portions of the following results have been published recently. (See [88] and [89].)

4.4.1. Governing BVP due to Imposed Harmonic Leg Strain

In order to derive the BVP governing the forced vibration of the ASID, a free-body diagram of an infinitesimal element of length *dx* in the leg, identical to that indicated in Fig. 4-1 for the free-vibration case, is employed. The resulting differential equation governing the axial vibration of the leg therefore has the same form as the free-vibration equation of motion (4-1):

$$\left[\rho bh + 2\bar{\bar{m}}_f\left(b+h\right)\right]\ddot{u}\left(x,t\right) + 2\bar{\bar{c}}_f\left(b+h\right)\dot{u}\left(x,t\right) - bh\sigma'(x,t) = 0 \qquad \text{(4-56)}$$

In the present case, however, it is important to point out that the response quantity, $u(x,t)$, in (4-56) represents the *total* axial displacement, i.e., the superposition of the imposed (stress-free) displacement due to the eigenstrain (e.g., the electrothermal strain) and any elastic displacement that arises due to the dynamics of the problem. The axial stress is related to the *elastic* strain through Hooke's law:

$$\sigma(x,t) = E\left[\varepsilon(x,t) - \varepsilon^*(t)\right] = E\left[u'(x,t) - \varepsilon_0 e^{i\omega t}\right] \tag{4-57}$$

where $\varepsilon(x,t)$ is the total axial strain in the leg. Since the eigenstrain is assumed to be uniform throughout the legs (i.e., its derivative with respect to *x* is zero), the substitution of (4-57) into (4-56) yields the *same* (homogeneous) equation of motion as described by (4-3):

$$\left[\rho bh + 2\bar{\bar{m}}_f\left(b+h\right)\right]\ddot{u}\left(x,t\right) + 2\bar{\bar{c}}_f\left(b+h\right)\dot{u}\left(x,t\right) - Ebhu''\left(x,t\right) = 0 \tag{4-58}$$

The fixed-end condition at *x*=0 gives the first boundary condition:

$$u\left(0,t\right) = 0 \tag{4-59}$$

Noting that the boundary condition at *x*=*L* may be written in terms of the axial stress as $\sigma\left(L,t\right) = F\,/\,bh$, where *F* is related to the disk motion via (4-6), this second BC may be expressed in terms of displacement by using (4-57):

$$\frac{\pi}{4}\frac{\rho a^2}{Eb}\left\{\left[1+\left(1+\frac{2h}{a}\right)\sqrt{\frac{2\rho_f\eta}{\rho^2h^2\omega}}\right]\ddot{u}\left(L,t\right)+\left(1+\frac{2h}{a}\right)\sqrt{\frac{2\rho_f\eta\omega}{\rho^2h^2}}\dot{u}\left(L,t\right)\right\}+u'(L,t) = \varepsilon_0 e^{i\omega t} \tag{4-60}$$

Thus, we see that the forced-vibration BVP for the continuous model differs from its free-vibration counterpart only by virtue of the eigenstrain appearing on the right-hand side of the non-homogeneous BC (4-60). [Compare (4-60) with (4-7).]

The non-dimensional form of the forced-vibration BVP [(4-58), (4-59), and (4-60)] may be obtained by using the dimensionless quantities defined by (4-9a-e), resulting in

$$\bar{u}''(\xi,\bar{t})-\frac{\pi^{3/2}}{2}\sqrt{\bar{L}_0\bar{L}}\left(1+\frac{1}{\bar{b}}\right)\sqrt{\bar{\omega}}\,\dot{\bar{u}}(\xi,\bar{t})-\frac{\pi^2}{4}\left[1+\frac{2}{\sqrt{\pi}}\sqrt{\bar{L}_0\bar{L}}\left(1+\frac{1}{\bar{b}}\right)\frac{1}{\sqrt{\bar{\omega}}}\right]\ddot{\bar{u}}(\xi,\bar{t})=0, \tag{4-61a}$$

$$\bar{u}\left(0,\bar{t}\right)=0, \tag{4-61b}$$

$$\bar{u}'(1,\bar{t})+\frac{\pi^3}{16}\frac{\bar{a}^2}{\bar{b}\,\bar{L}}\left\{\frac{2}{\sqrt{\pi}}\sqrt{\bar{L}_0\bar{L}}\left(1+\frac{2}{\bar{a}}\right)\sqrt{\bar{\omega}}\,\dot{\bar{u}}(1,\bar{t})+\left[1+\frac{2}{\sqrt{\pi}}\sqrt{\bar{L}_0\bar{L}}\left(1+\frac{2}{\bar{a}}\right)\frac{1}{\sqrt{\bar{\omega}}}\right]\ddot{\bar{u}}(1,\bar{t})\right\}=\varepsilon_0 e^{i\bar{\omega}\bar{t}}. \tag{4-61c}$$

Note that $\bar{\omega}\equiv\omega/\omega_0$ in the BVP (4-61a-c) is the normalized *exciting* frequency, i.e., the specified frequency of the imposed eigenstrain and, thus, the frequency of the steady-state response.

4.4.2. Steady-State Solution to BVP: Output Signals

It can be easily shown that the steady-state solution of (4-61a-c) due to the harmonic eigenstrain in the legs has the form

$$\bar{u}(\xi,\bar{t})=\varepsilon_0\bar{U}(\xi)e^{i\bar{\omega}\bar{t}} \tag{4-62}$$

where

$$\bar{U}(\xi) = \frac{\sin\gamma\xi}{\gamma\cos\gamma - \frac{\pi^3}{16}\frac{\bar{a}^2}{\bar{b}\bar{L}}\bar{\varpi}^2\sin\gamma\left[1+2(1-i)\left(1+\frac{2}{\bar{a}}\right)\sqrt{\frac{\bar{L}_0\bar{L}}{\pi\bar{\varpi}}}\right]} \;,$$

$$\gamma = \frac{\pi\bar{\varpi}}{2}\left[1+2(1-i)\left(1+\frac{1}{\bar{b}}\right)\sqrt{\frac{\bar{L}_0\bar{L}}{\pi\bar{\varpi}}}\right]^{1/2} , \qquad \text{(4-63a, b)}$$

is a complex-valued frequency-dependent function from which the amplitude and phase shift of the leg displacement can be obtained at any location in the leg. From this solution any (mechanical) output signal of possible interest may be determined. Two such signals are the disk rotation, θ , which is proportional to the average axial strain, ε_{avg} , in each leg, and the local axial strain in the legs at the supports, ε_{sup} . These signals are easily derived from the solution for the leg displacement. Convenient normalized forms of these output quantities are given by

$$\bar{\theta}(\bar{t}) \equiv \frac{\theta(\bar{t})}{\varepsilon_0 L/a} = \frac{\varepsilon_{avg}(\bar{t})}{\varepsilon_0} = \bar{U}(1)e^{i\bar{\varpi}\bar{t}}, \qquad \bar{\varepsilon}_{sup}(\bar{t}) \equiv \frac{\varepsilon_{sup}(\bar{t})}{\varepsilon_0} = \bar{U}'(0)e^{i\bar{\varpi}\bar{t}} . \quad \text{(4-64a, b)}$$

The average leg strain signal given by (4-64a) corresponds to the overall electrical resistance in the legs and is thus the relevant output quantity for the device shown in Fig. 1-1 whose motion detection scheme was based on variations in the electrical resistance due to the piezoresistive effect [24]. On the other hand, the local strain signal represented by (4-64b) corresponds to the local electrical resistance whose changes would be monitored if the read-out scheme were based on, for example, a piezoresistive Wheatstone bridge being employed near the support [56]. While these two output signals are considered in the present work, we again emphasize that any other mechanical response quantity that may be of interest can be derived from the displacement field given by (4-62) and (4-63a, b).

CHAPTER 5:

ASID RESONATOR RESPONSE: NUMERICAL RESULTS AND DISCUSSION

5.1. Introduction

Numerical results of the predicted ASID resonator response based on the models described in Ch. 3 (SDOF model) and Ch. 4 (continuous-system model) are presented in this chapter. Starting with the free-vibration results in Sect. 5.2, the damped natural frequency given by the SDOF model is compared with the mode-1 result of the continuous model. The in-fluid natural frequency results are followed by comparisons of the vacuum-to-fluid decrease in the natural frequency and the quality factor results for the two models over practical ranges of the various system parameters. In addition to the general ASID modeling, free-vibration results for the special no-disk case, based on the analytical solution derived in Sect. 4.3.5, are presented in Sect. 5.2.4 and the associated in-fluid eigenproperties of a single leg under axial vibration are discussed. Results for the forced-vibration response under imposed harmonic leg strain are then presented and discussed (Sect. 5.3). These results include the frequency response results (displacement amplitude and phase) from which the ASID's resonant characteristics, including the in-fluid resonant frequency, the fluid-induced reduction in the resonant frequency, and the quality factor at resonance, are extracted and compared with the eigenproperties of the system obtained from the free-vibration case. In an attempt to represent the resonant behavior of the ASID through its eigenproperties, results of Sects. 5.2 and 5.3 are compared to one another in Sect. 5.4 for various ASID design parameters. For validation purposes, the theoretical results of the present study are compared with finite element modeling of the device for both in-vacuum and in-fluid cases (Sect. 5.5). Finally, further validation of the theory is provided in Sect. 5.6, in which the theoretical values of the ASID's quality factor are compared to the existing experimental data.

5.2. Free-Vibration Results

Free-vibration analysis of the ASID resonator operating in a viscous fluid is summarized in Sect. 3.3 for the SDOF model and in Sect. 4.3 for the continuous model. The analytical solutions obtained in those sections will be employed in this section to perform a parametric study of the underlying in-fluid eigenproperties of the ASID device. The free-vibration results, including the results of both models, along with relevant discussion in this section will focus on the damped natural frequency and quality factor of the ASID and their functional dependence upon the basic ASID design parameters – thus shedding light on how to maximize the resonator's performance in a viscous fluid environment. Moreover, these results will be used extensively in Ch. 6 in which the sensing performance metrics of an ASID-based sensor are investigated. It should be noted that, while the sufficient accuracy of the approximate analytical expressions for the damped natural frequency for small fluid resistance (Sects. 3.3 and 4.3) has been confirmed, the numerical results associated with the general ASID device in this section are based on the "exact" solutions to Eq. (3-11) for the SDOF model and Eq. (4-33) for the continuous model. However, for the special no-disk case of the ASID, we will include both the exact and the approximate results (approximate in the sense that the fluid resistance parameter is assumed to be small) to ensure that the obtained approximate formulae for this special case are sufficiently accurate as well.

5.2.1. In-Fluid Natural Frequency

Theoretical results for the damped natural frequency of a silicon-based ASID $\left(E = 130\,\text{GPa},\ \rho = 2330\ \text{kg/m}^3\right)$ operating in water $\left(\rho_f = 1000\ \text{kg}/\text{m}^3,\ \eta = 0.001\ \text{Pa}\cdot\text{s}\right)$ are shown in Fig. 5-1 in which the normalized in-fluid natural frequency of the device is plotted against the disk size for fixed leg dimensions. (These silicon properties are based on the case in which the legs are aligned with the <100> crystalline direction as was specified in [24].) Comparing the results of the SDOF model with the mode-1 results of the continuous model in Fig. 5-1, it is clear that the SDOF model fails to capture the correct values for the in-fluid natural frequency of the ASID at small disk radii, theoretically approaching infinity at $\bar{a} = 0$. This behavior was expected for the SDOF model as the mass of the supporting legs and their associated fluid effects are neglected in this simple model. (This assumption also explains why the SDOF results in Fig. 5-1 overestimate those of the more accurate continuous model for mode 1, i.e., underestimating the mass and damping results in a higher natural frequency.) For relatively large disk sizes, however, mass and fluid resistance effects associated with the disk becomes dominant as opposed to those associated with the legs, thus decreasing the discrepancy between the two models as the disk gets larger.

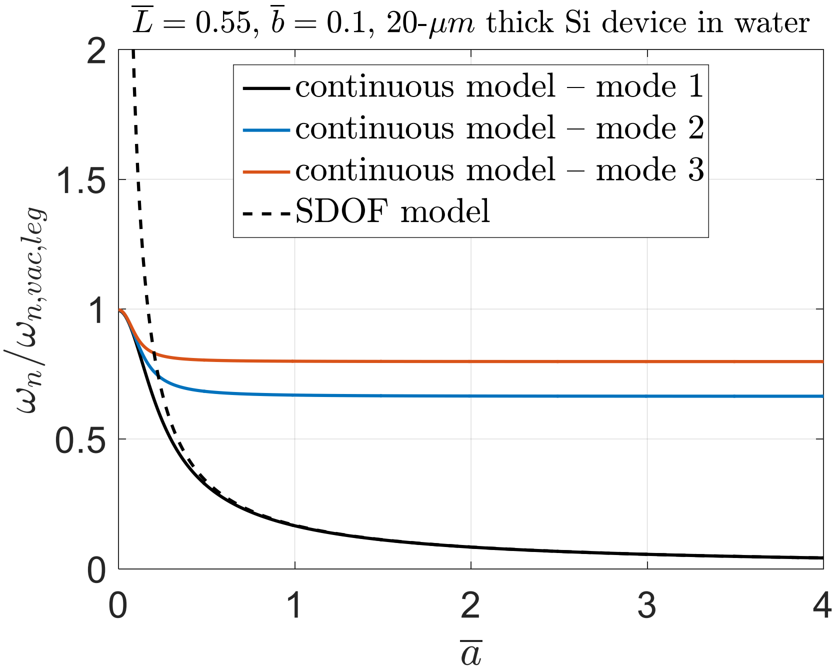

Fig. 5-1. Variation of the damped natural frequency of an ASID resonator with respect to the disk size – SDOF model vs. continuous model (modes 1-3)

The results of the (mode-1) continuous model as well as the SDOF model shown in Fig. 5-1 indicate that increasing the disk size results in a lower damped natural frequency of the device. This is because a larger disk simply means a larger ASID mass, a larger added fluid mass, and a larger added fluid damping to the system, all of which contribute to the reduction in the damped natural frequency of the system for the fundamental mode while the stiffness of the device (i.e., legs' geometry and material) remains unchanged. For modes 2 and 3, the natural frequency of the ASID also decreases when the disk size is increased initially as shown in Fig. 5-1; however, this resonant characteristic of the system becomes quite insensitive to the disk size quickly as the disk gets larger. To physically interpret these natural frequency results of the ASID for modes 2 and higher, one may argue that the behavior of the present system in higher modes is similar to that of a fixed-fixed axial member – i.e., a rod that is perfectly fixed at one end and essentially fixed at the other end since it is attached to a disk that barely moves due to its significant inertia in these higher modes. Therefore, if the ASID resonator is operated at a mode other than the fundamental mode, an extremely small disk rotation amplitude converts the ASID device virtually to two fixed-fixed legs oscillating axially, whose resonant characteristics in vacuum are well-known (e.g., [90]). (Details regarding the in-fluid vibration amplitude and output signal of the system for different modes will be included later in the forced-vibration section of this chapter.) Also note that the large-disk asymptotic behavior of the results shown in Fig. 5-1 has already been discussed in Sect. 4.3.5 and the analytical asymptotic expression for the mode-n natural frequency of the ASID is given by (4-40).

Since the results shown above are limited to ASID specimens having a fixed set of leg dimensions, one may also want to explore the effect of the leg dimensions on the natural frequency of the device. In particular, the effect of the leg width-to-length ratio, which is proportional to the axial stiffness of the leg, on the damped natural frequency of the device may be of most interest. Such results are shown in Fig. 5-2 in which the variation of the natural frequency with $\sqrt{\bar{b}/\bar{L}}$ for different values of $\bar{a}$ is shown. It is important to note that since the dimensionless form of the damped natural frequency is based on scaling by the natural in-vacuum frequency of an axial-mode cantilever, and that this reference frequency varies with L itself, here we present instead the *dimensional* natural frequency results in Fig. 5-2. Also note that the parameter in the abscissa of the figure is varied in a manner such that the top surface area of the legs remains unchanged ($bL=0.4h^2= 0.4(20)^2=160\ \mu\text{m}^2$); therefore, the mass of the device is fixed for all cases considered in the figure.

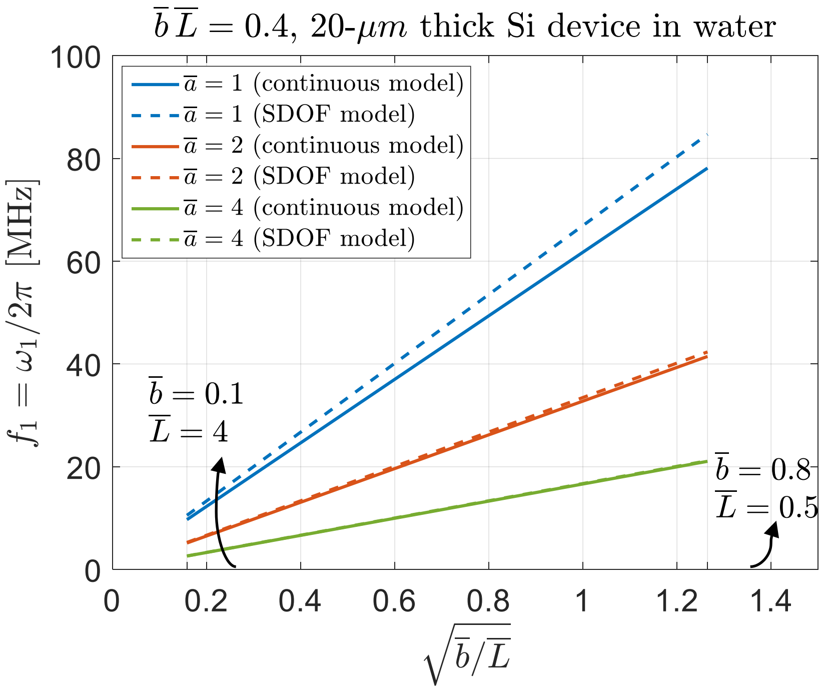

Fig. 5-2. Effect of leg aspect ratio on the damped natural frequency of the ASID – SDOF model vs. continuous model (mode 1)

The results of Fig. 5-2 indicate that the combination of increasing leg width and decreasing leg length (i.e., wider, shorter, and therefore stiffer legs) yields a higher frequency, as expected. As was the case for Fig. 5-1, the results shown in Fig. 5-2 for the SDOF and continuous models also demonstrate that the discrepancy between the two models increases as the disk size gets smaller. While the results presented in this figure are based on a fixed *bL* value, one may intuitively conclude that increasing the stiffness could also be obtained either (a) by increasing *b* with a fixed *L* value in which case a larger surface area results in the leg mass and the associated inertial and viscous fluid effects to increase, or (b) by decreasing *L* with a fixed *b* value in which case a smaller surface area results in the leg mass and its associated fluid effects to decrease. In the first (second) case, the increase (decrease) in the leg mass and associated fluid effects would be expected to decrease (increase) the slope of the curves shown in Fig. 5-2.

5.2.2. Vacuum-to-Fluid Shift in Natural Frequency

In the previous section a parametric study was performed to demonstrate how the ASID's dimensions affect the performance of the device in terms of the damped natural frequency – without focusing on the effects of changing the surrounding fluid. In most liquid-phase MEMS resonators, including the present ASID device, one of the main challenges that researchers face is minimizing the detriments of the inertial and viscous effects associated with the ambient fluid. The added fluid mass and damping for liquid-phase resonators causes the natural frequency of the device to drop compared to the in-vacuum case. This shift in frequency depends on the properties of the surrounding fluid in which the device is immersed.

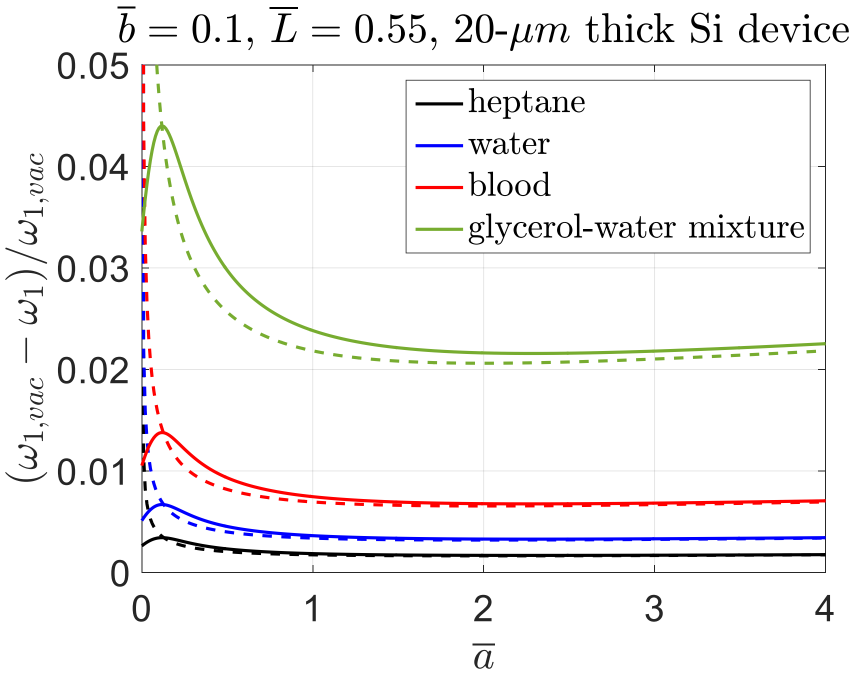

Fig. 5-3. Vacuum-to-fluid shift in natural frequency of the ASID – mode-1 continuous model (solid) vs. SDOF model (dashed)

Figure 5-3 shows the relative vacuum-to-fluid shift in the natural frequency of the ASID as a function of the disk radius while the other dimensions are fixed. Four different liquids are considered in Fig. 5-3, as characterized by the following density and viscosity properties (listed from lowest to highest): heptane $\left(\rho_f = 679.5\ \mathrm{kg/m^3},\ \eta = 0.000386\ \mathrm{Pa \cdot s}\right)$, water $\left(\rho_f = 1000\ \mathrm{kg/m^3},\ \eta = 0.001\ \mathrm{Pa \cdot s}\right)$, blood $\left(\rho_f = 1060\ \mathrm{kg/m^3},\ \eta = 0.004\ \mathrm{Pa \cdot s}\right)$, and glycerol (75%wt)-water mixture $\left(\rho_f = 1200\ \mathrm{kg/m^3},\ \eta = 0.036\ \mathrm{Pa \cdot s}\right)$. Of all the liquids considered in this figure, the most viscous (and densest) one, the glycerol-water mixture, reduces the natural frequency of the device by the most, as expected. For this particular liquid, the difference between the results of the continuous model and the SDOF model is greater than that of the other cases. The reason for this is that a more viscous and denser fluid surrounding the device results in a larger added fluid mass and damping to the legs. Since these effects are completely neglected in the SDOF model, a larger discrepancy between the two models is observed in Fig. 5-3 for the glycerol-water mixture. Results of both models (for all four liquids) in Fig. 5-3 show that the fluid-induced shift in the natural frequency of the system has a minimum value at or near $\bar{a} = 2$. At this special $\bar{a}$ value, the relative minimum of the shift in natural frequency may also be a global minimum, as is the case in this figure, or it might not correspond to a global minimum. The latter case will often be encountered when the legs are relatively stiff, resulting in the global minimum value of the relative fluid-induced shift in the natural frequency occurring when the disk radius is zero (i.e., for the no-disk case). The non-monotonic behavior of the shift in natural frequency of the ASID with respect to the disk size, exhibited in Fig. 5-3, may be related in large part to the added fluid mass. This quantity is the main cause of the reduction in frequency when a resonator operates in a viscous fluid. (More specifically, the vacuum-to-fluid frequency shift of the ASID may be written in a general form as

$$\frac{\omega_{vac}-\omega}{\omega_{vac}}=1-\frac{\omega}{\omega_{vac}}=1-\frac{\sqrt{K/\left(M_{ASID}+M_f\right)}}{\sqrt{K/M_{ASID}}}=1-\frac{1}{1+M_f/M_{ASID}}$$

in which "*K*" is the effective stiffness of the system, and "M_{ASID}" and "M_f" are the effective masses associated with the device and the fluid, respectively. Therefore, the initial increase in the frequency shift that leads to a maximum value as shown in Fig. 5-3 is related to the increase in the M_f/M_{ASID} ratio while the decrease in the frequency shift that follows and leads to a relative (or global) minimum value may be related to the decrease in this ratio.) The results shown in Fig. 5-3 indicate that the magnitude of the fluid-induced relative shift in natural frequency of the ASID is relatively small even for very viscous and dense liquids. While this magnitude increases as the legs become more slender [see Eqs. (3-13) and (3-14)], the efficiency of the ASID design keeps the frequency shift relatively small even for extremely slender legs. For example, for the case of L/b=20 (as opposed to L/b=5.5 in the figure), the fluid-induced shift in frequency of the ASID is less than 10% when the device is immersed in the very viscous/dense glycerol-water mixture.

It may also be useful to look at the frequency shift results of the ASID at higher modes of vibration. In order for the results to be independent of the materials used for the ASID device and the ambient fluid, a more general "material-normalized" vacuum-to-fluid shift in the natural frequency of the ASID is studied for the first three modes for two cases as shown in Fig. 5-4. Note that cases 1 and 2 indicated in the figure are associated with relatively slender legs and relatively stiff legs, respectively. With the curves corresponding to case 2 being below those associated with case 1, Fig. 5-4 suggests that an ASID design with stiffer supporting legs lowers the fluid-induced reduction in the natural frequency significantly, regardless of the fluid properties. While the results of case 2 (stiffer legs) indicate that the frequency shift curves for modes 2 and 3 are below the mode-1 curve for any $\bar{a}$ value, the mode-1 results of case 1 (slender legs) show that the magnitude of the relative frequency shift is smaller than that of modes 2 and 3 over a specific range of $\bar{a}$ ($\bar{a}$ >1.5 approximately in this case).

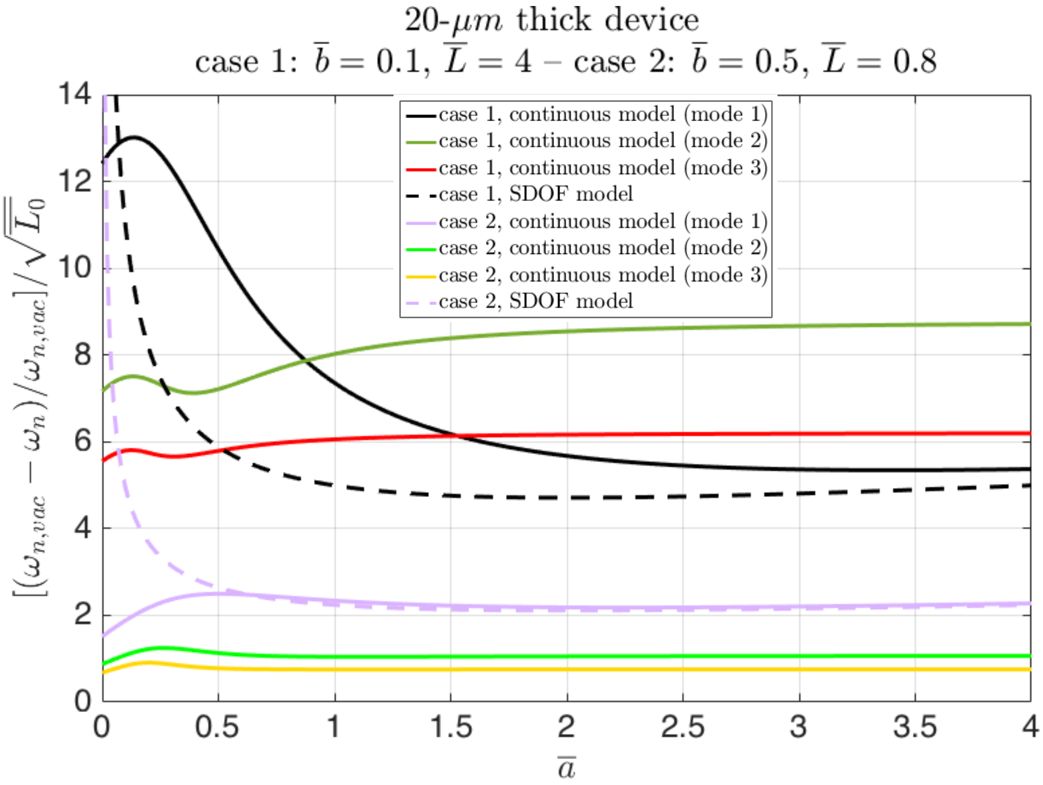

Fig. 5-4. "Material-normalized" shift in natural frequency of the ASID – continuous model (modes 1-3) and SDOF model

Comparing the continuous-model results of the two cases for mode 1 with the SDOF-model curves in Fig. 5-4, it is observed that the discrepancy between the two models decreases significantly for case 2 in which stiffer legs are used. [One possible explanation for this is that the higher stiffness in case 2, while the mass remains unchanged, results in a higher natural frequency of the ASID. The fluid mass effect, including that associated with the legs (neglected by the SDOF model) is the main cause of the shift in natural frequency of the ASID. Since the effective fluid mass varies inversely with frequency (see Eq. (3-4b)), we would expect the difference between the two models to become smaller at higher frequencies.]

5.2.3. Quality Factor

Another important characteristic of liquid-phase MEMS resonators is the quality factor of the system that indicates how well (or poorly) a device performs as a resonant sensor in a particular viscous fluid environment (gas or liquid). Depending on the applications, such resonators could operate in fluids with different physical properties (density and viscosity, in particular), and therefore one would expect the quality factor to vary considerably when the device is immersed in different liquids. This is explored in Fig. 5-5 in which the effect of material properties (both solid and liquid), represented by the material-dependent parameter $\bar{L}_0$ (whose definition is listed explicitly in the figure), on the quality factor of the ASID is shown for different values of $\bar{a}$ and fixed leg dimensions.

It is apparent from Fig. 5-5 that the results of the continuous model yield an essentially linear variation of Q with respect to the abscissa quantity, $1/\sqrt{\bar{L}_0}$, a result which is mathematically evident in the SDOF approximate relationship encapsulated by Eq. (3-13). [Note that (3-13) may easily be expressed in terms of $\bar{L}_0$ through (4-9e) or using the abscissa label in Fig. 5-5.] Again, we see the expected departure of the SDOF-model results from those of the continuous model (a very slight overestimation in this case) as the disk size becomes smaller relative to the device thickness. As expected, the device will yield a higher quality factor in liquids having lower values of viscosity. (Analogously, Q will also increase when the fluid density is decreased since density and viscosity always appear together as a product in the Stokes fluid resistance model as indicated in the abscissa label of Fig. 5-5.) The quality factor also increases as the material's modulus or density is increased. (See the material-dependence of the abscissa in Fig. 5-5.) Another important conclusion from the results of Fig. 5-5 is that the quality

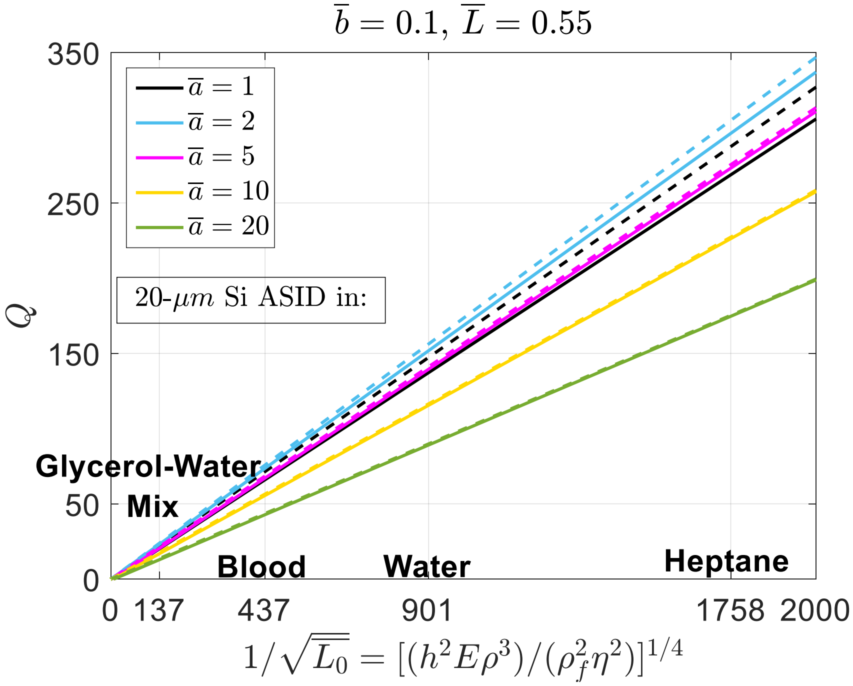

Fig. 5-5. Effect of material properties on the quality factor of the ASID – mode-1 continuous model (solid) and SDOF model (dashed)

factor of the ASID increases as the device thickness is increased. This implies that if all of the ASID's geometric dimensions are multiplied by a factor *k* (i.e., uniform shrinking or enlarging of the device) the quality factor of the system will change approximately by a factor of $\sqrt{k}$ [and the resonant frequency and fluid-induced relative shift in resonant frequency will be multiplied approximately by $1/k$ and $1/\sqrt{k}$, respectively]. [See Eq. (3-22b) of the SDOF model and Eq. (4-39) of the continuous model for the explicit relationship between the quality factor and the device thickness.] This result is important for mass-based sensing applications in which miniaturization of an ASID-based sensor may make it more "sensitive" as the device is scaled down, but this will reduce the quality factor and increase the percent change in resonant frequency caused by the fluid as well. (Detailed parametric studies of the sensing performance metrics of an ASID-based sensor, including how they scale, will be presented in Ch. 6.)

While the curves of Fig. 5-5 are general in the sense that they apply to arbitrary material properties and device thicknesses, we have indicated for illustrative purposes specific abscissa values corresponding to a 20-μm-thick silicon device immersed in four different liquids whose physical properties have been listed earlier in Sect. 5.2.2. Heptane, being the least viscous of the four liquids, gives the highest quality factor, whereas liquids of higher viscosity and density such as a glycerol (75%wt)-water mixture or blood are seen to reduce the quality factor significantly. Theoretical results such as those depicted in Fig. 5-5 may be useful in extrapolating experimental Q data for one material system (e.g., a Si device in water) to another material system (e.g., an SU-8 device in blood).

In addition to the device thickness, the other ASID geometric parameters (disk and leg dimensions in "plan view") also have an effect on the quality factor of the device.

Since the effect of the material properties on the quality factor of the ASID has already been illustrated through Fig. 5-5, a “material-normalized” quality factor quantity, $\bar{Q} \equiv \sqrt{\bar{L}_0} Q$, is plotted against the normalized disk radius for different values of $\bar{b}$ and $\bar{L}$ in Fig. 5-6. Clearly seen in Fig. 5-6 is the existence of a relative maximum, which in some cases corresponds to a *Q*-optimal disk size (global maximum for *Q*). The SDOF model gives a constant optimal disk radius of $\bar{a}_{opt} = 2$ for all cases [see Eq. (3-13)], while the disk size yielding the relative maximum in *Q* is seen to vary and depend on the leg dimensions when the more exact continuous model is utilized. It is also observed that the peaks of the curves shown in Fig. 5-6 are relatively flat; thus, the simple SDOF model gives a good estimate of the relative maximum value of *Q* as calculated using the more accurate continuous model. [An analogous comment applies to predicting the relative minimum in the fluid-induced relative shift in natural frequency as well due to the inverse relationship between the two quantities.] Also of interest is that the continuous-model results show that the presence of the disk does not necessarily increase the *Q* value beyond that of the isolated leg (i.e., the no-disk case in which $\bar{a} = 0$), as indicated by the global maximum occurring at $\bar{a} = 0$ for the cases of stiffer legs. However, for the more flexible (more slender) legs, implementing a disk of optimal or near-optimal radius ($\bar{a} \approx 2$) may significantly improve *Q* over that of a simple cantilever driven axially. In fact, one may easily derive an approximate criterion for determining in which cases an appropriately designed ASID (i.e., with properly sized disk) will result in a higher *Q* than the isolated leg (no-disk case). Specifically, by comparing the approximate expression for the maximum *Q* obtained in the SDOF model, given by Eq. (3-15a), to the approximate formula for the (mode-1) quality factor of an isolated leg, given by Eq. (4-55), one may show that when the leg dimensions satisfy

$$\bar{L} > 4\pi^3 \frac{\bar{b}^3}{\left(1+\bar{b}\right)^4}, \tag{5-1}$$

the “true ASID” with optimal or near-optimal disk size ($\bar{a}$ near 2) will have a higher viscous quality factor than the axial-mode microcantilever.

Figure 5-6 also suggests that, in general, the accuracy of the SDOF estimate for the quality factor will deteriorate as the disk radius and/or the stiffness of the device decreases. As mentioned earlier, this is due to the increasing importance of leg mass and leg fluid resistance (both neglected in the SDOF model) as the disk size decreases relative to the leg size.

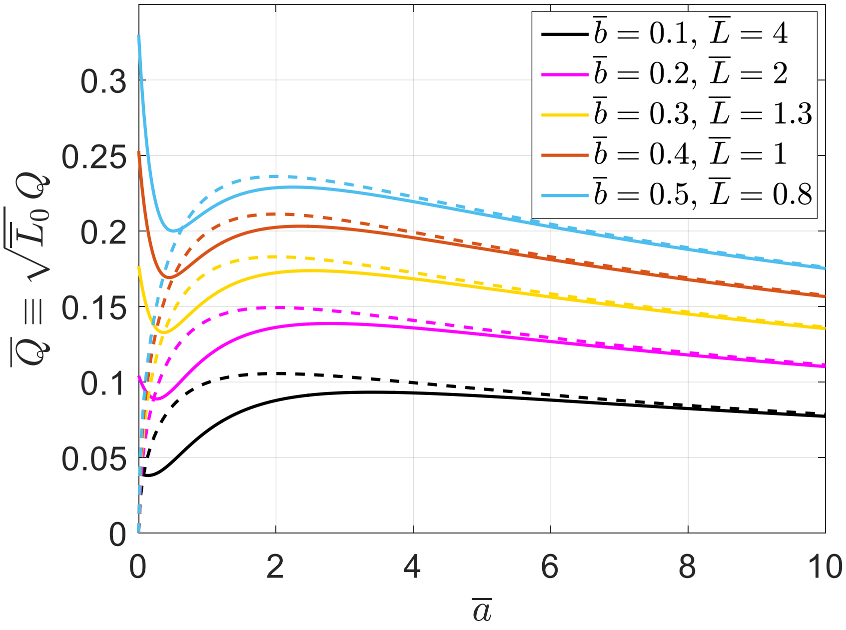

Fig. 5-6. “Material-normalized” quality factor of the ASID plotted vs. disk size – mode-1 continuous model (solid) and SDOF model (dashed)

Regarding the disk size at which Q has a relative maximum value, the detailed variation of this special value of disk radius – that we will describe as the "critical" disk radius, $\bar{a}_{cr}$ – can be observed in Fig. 5-7 in which $\bar{a}_{cr}$ is seen to increase with increasing $\bar{L}$ and decreasing $\bar{b}$. All curves in Fig. 5-7 begin at the SDOF value of 2, indicating that the SDOF result provides a lower bound on the critical disk size. While the results in Fig. 5-7 are associated with a particular device thickness and material system (20-µm-thick silicon device in heptane), additional calculations show that the dependence of the critical value of $\bar{a}$ on the normalized material length, $\bar{L}_0$, is negligible for practical ranges of solid and fluid properties and microscale device dimensions.

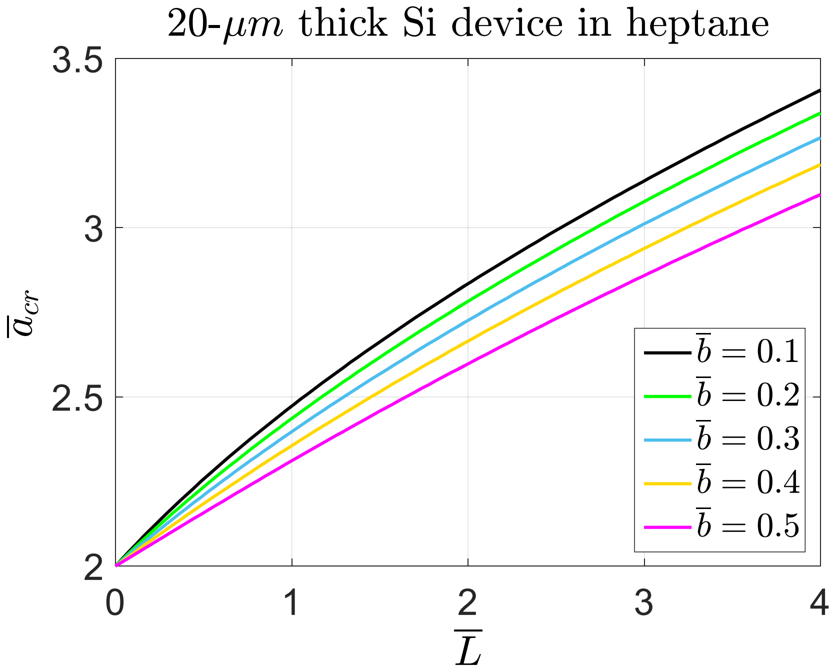

Fig. 5-7. Critical disk size (resulting in a relative maximum in *Q*) versus leg length for various values of leg width

It is important to note that, while the results presented in Figs. 5-5 and 5-6 suggest that the ASID device is theoretically capable of very high levels of Q in liquid (in excess of 300) if the legs are shorter and wider (i.e., stiffer) and if the disk radius is critical (or near-critical), there may exist limitations that make an increase in leg stiffness beyond a certain point impractical as this could lead to an undetectable output signal. For example, if the legs are stiffened by decreasing their length, this will be accompanied by a reduction in the quasi-static disk rotation due to the electrothermal leg strain, since the quasi-static disk rotation is proportional to the leg length. In addition, any stiffening of the legs, due to either decreasing the length L or increasing the width b, would result in a reduction of the dynamic response of the system.

5.2.4. Special Case: Single Leg Eigenproperties (No-Disk Case)

An axial-mode microcantilever is a special case of the general ASID design that may be considered as a separate device whose performance can be compared with that of the ASID resonator and also with other microcantilever-based devices that are excited in different modes of vibration (flexural or torsional). The results of this section are based on the analytical approach toward the axial vibration of a single leg immersed in a viscous fluid summarized in Sect. 4.3.6 of the previous chapter. In particular, the variation of the in-fluid natural frequency, the decay parameter, and the quality factor of a liquid-phase, axial-mode cantilever with respect to the fluid resistance parameter, β, is studied for the first three modes. (The explicit definition of β in terms of the system parameters is listed in the following figures.)

As expected and shown in Fig. 5-8a, the normalized damped natural frequency of the cantilever decreases as the fluid resistance parameter is increased (due to the inertial and viscous fluid effects on the cantilever). The “exact” results shown in this figure are based on the numerical solution to the frequency equation (4-46) which enables us to obtain the results accurately for larger values of β.

In order to compare the approximate analytical expression for the damped natural frequency of the cantilever, given by Eq. (4-53), with the exact solution of Eq. (4-46), the results for relatively small (and more practical) values of β are shown in Fig. 5-8b. As the fluid resistance parameter gets larger, the discrepancies between the exact and approximate curves in Fig. 5-8b tend to increase because the derivation of the approximate formula is based on the assumption of a small value of fluid resistance parameter; hence it is expected to fail at larger β values. (For a relatively slender Si cantilever with the width of $\bar{b} = 0.1$ and length of $\bar{L} = 4$ immersed in a relatively viscous fluid such as glycerol (75%wt)-water mixture, β is approximately 0.18; therefore the approximate equation would give fairly accurate results in most practical cases.) It may also be interesting to note that the difference between the exact and approximate results shown in Fig. 5-8b decreases when the cantilever is operated at higher modes. For example, at $\beta = 0.3$, the relative error reduces from 1.5% at mode 1 to 0.46% at mode 2 to 0.27% at mode 3.

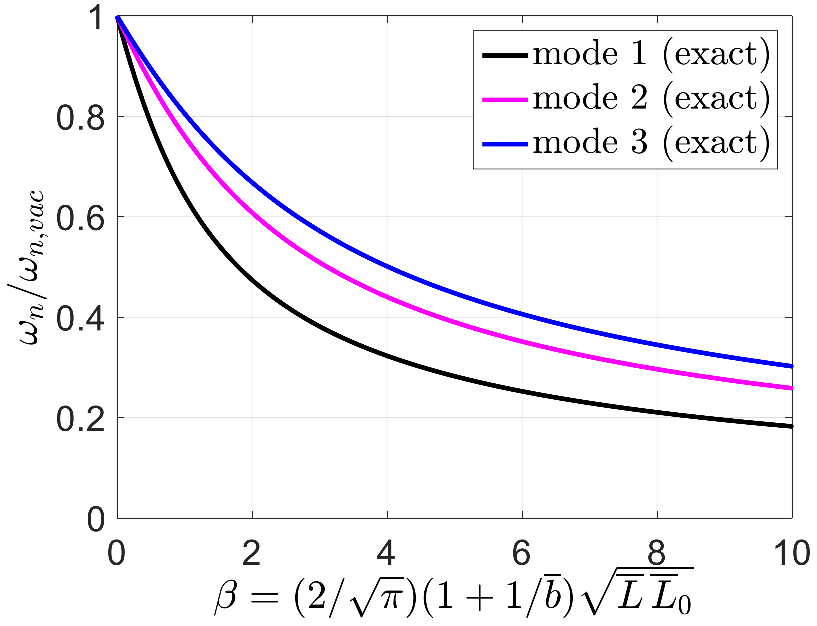

(a)

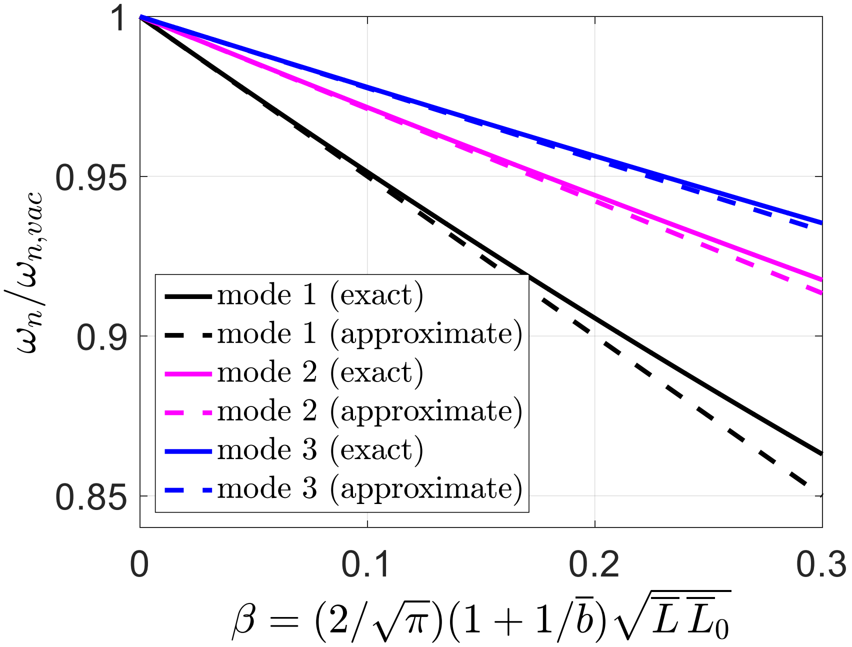

(b)

Fig. 5-8. (a) Variation of the normalized in-fluid natural frequency of a single leg with the fluid parameter; (b) Comparison between the exact and approximate results for small β values.

The variation of the (normalized) decay parameter, another important characteristic of the cantilever that – along with the damped natural frequency – determines the quality factor of the device, is shown in Fig. 5-9a in which the exact results [obtained by substituting the "exact" values of $\bar{\omega}_n$ into Eq. (4-45)] are plotted against the fluid resistance parameter for the first three modes. For the purpose of comparison, the results obtained from the approximate analytical formula for the decay parameter of an isolated cantilever, given by Eq. (4-54), are presented for smaller β values as shown in Fig. 5-9b. Similar to the results of the damped natural frequency presented earlier, Fig. 5-9b shows that the difference between the exact and approximate curves increases with increasing values of the fluid resistance parameter, as expected.

Figure 5-9a exhibits a peak value in $\delta_n / \omega_{n,vac}$ with respect to β for each mode. This peak value is the same for all modes and can be determined analytically by using (4-45) and (4-46). (See Appendix A for the derivation details.) Final results are as follows:

$$(\beta_{cr})_n = \frac{4K}{4K^2 - 2K + 1}\left[\frac{\left(4K^2+1\right)^2 - 4K^2}{\left(4K^2+2K+1\right)^2 + 4K^2}\right]^{1/4}\sqrt{2n-1} = 1.3651\sqrt{2n-1} \qquad (5\text{-}2)$$

$$\left.\frac{\delta_n}{\omega_{n,vac}}\right|_{max} = \frac{2K}{4K^2+2K+1}\sqrt{\frac{\left(4K^2+1\right)^2 - 4K^2}{\left(4K^2+2K+1\right)^2 + 4K^2}} = 0.1829 \qquad (5\text{-}3)$$

where $K = \left(\frac{\sqrt{5}+3}{16}\right)^{1/3} = 0.6891$.

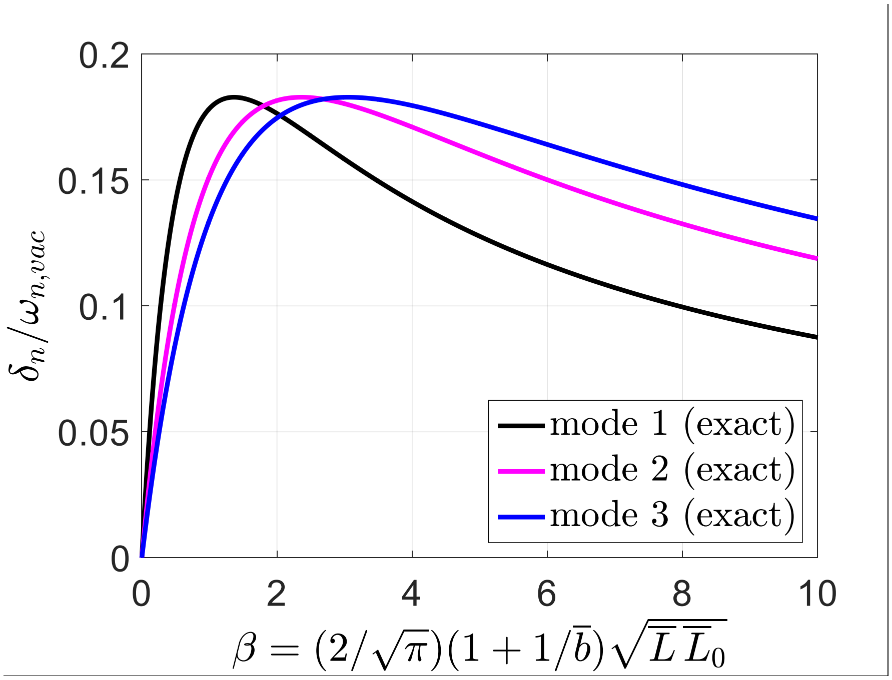

(a)

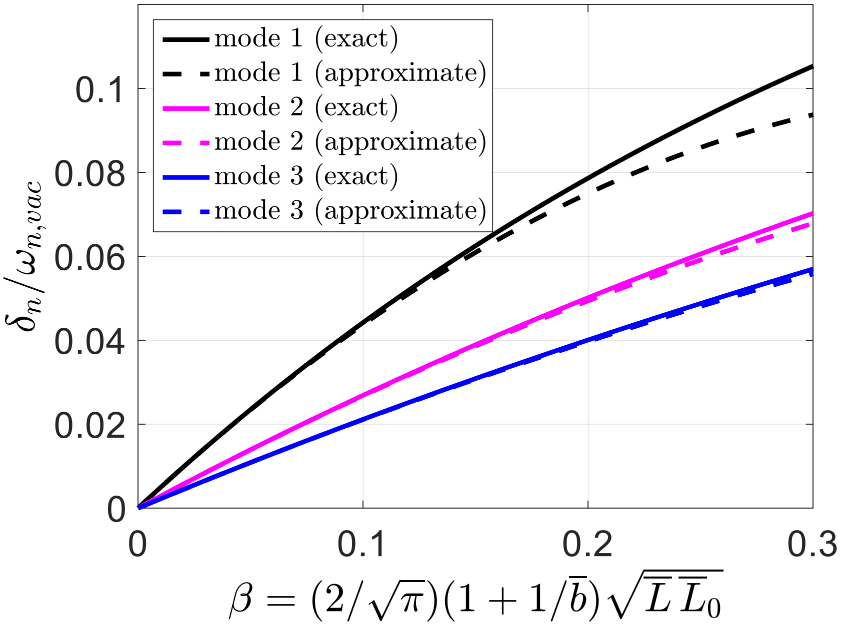

(b)

Fig. 5-9. (a) Variation of the normalized decay parameter of an isolated leg with the fluid parameter; (b) Comparison between the exact and approximate results for small β values.

The peak value for the decay parameter as a function of β implies that the quality factor of the system must have a lower bound with respect to the fluid resistance parameter. This asymptotic behavior may be observed better by plotting the δ_n/ω_n ratio or the damping ratio, d_n, of the cantilever with respect to the fluid parameter β as shown in Fig. 5-10. As $\beta \to \infty$, the δ_n/ω_n ratio approaches a maximum value of ½ for all modes. (See Appendix A for the derivation and Fig. 5-10 for graphical evidence.) Therefore, based on Eq. (4-18), the viscous quality factor of the axial-mode cantilever has a lower bound of $\sqrt{5}/2 = 1.118$ as will be indicated by plots of Q to be presented shortly.

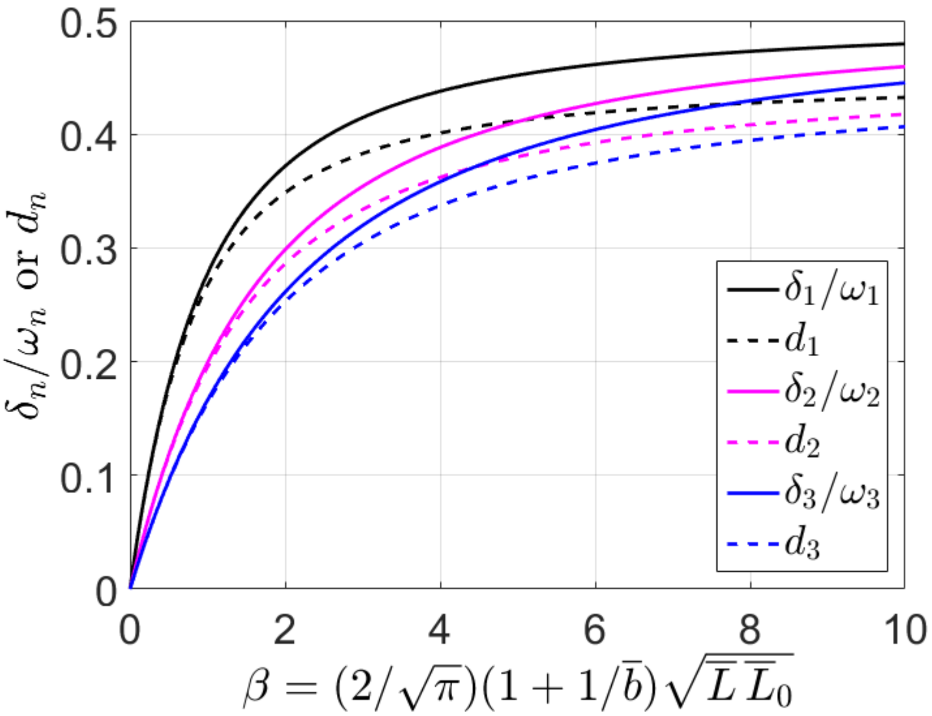

Fig. 5-10. Variation of the decay parameter-to-damped natural frequency ratio, and the damping ratio with the fluid resistance parameter. As $\beta \to \infty$, δ_n/ω_n curves approach 1/2; and damping ratio curves approach $1/\sqrt{5} = 0.4472$.

The quality factor results of the axial-mode cantilever over a relatively small, practical range of β are shown in Fig. 5-11 for the first three modes. The exact (approximate) curves are based on the exact (approximate) values of $\bar{\varpi}$ and $\bar{\delta}$ being substituted into Eq. (4-18). The curves of Fig. 5-11 not only show that increasing the fluid resistance parameter lowers the quality factor of the cantilever but, as mentioned earlier, all of the curves approach the same (non-zero) minimum value ($\sqrt{5}/2 = 1.118$) as β goes to infinity, regardless of mode number.

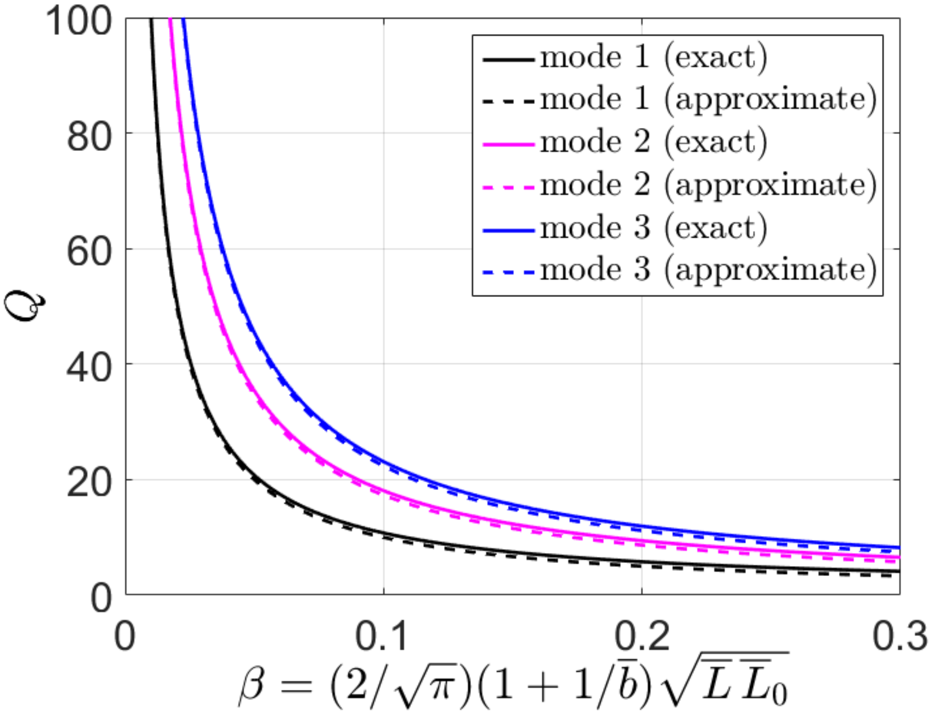

Fig. 5-11. Variation of the quality factor of an axial-mode microcantilever with the fluid resistance parameter.

The Q results obtained from the present theory for the no-disk case can also be useful should one wish to compare the performance of an axial-model cantilever with cantilevers vibrating in alternative modes. For example, for a silicon-based microcantilever $\left(E = 169\,\text{GPa},\ \rho = 2330\ \text{kg/m}^3\right)$ with the dimensions of ($L \times b \times h$) = (200×90×12) μm immersed in water $(\rho_f = 1000\ \text{kg/m}^3,\ \ \eta = 0.001\,\text{Pa}\cdot\text{s})$, the simple analytical formula, Eq. (4-55), yields Q = 142.7 for the fundamental axial mode, which is an excellent estimate of the more exact result of 143.5, obtained using Eqs. (4-46), (4-45), and (4-18). These axial-mode values for Q are much better than the corresponding theoretical Q values of 23 and 60 for the fundamental transverse and lateral flexural modes, respectively [60], and 44.3 for the fundamental torsional-mode cantilever [70]. Therefore, in this illustrative example it is found that the fundamental axial mode operation of a cantilever results in a viscous quality factor that is at least 2.4 times larger than the alternative fundamental modes.

Finally, the simple analytical formulas for an axial-mode microcantilever derived in the present study may be compared with previous theoretical results. For example, a general framework for analyzing the effect of a viscous fluid on a resonator was summarized in [42], in which a special case considered was that of an axial-mode cantilever in a fluid providing Stokes resistance. For the microcantilever/fluid pair considered in the previous paragraph, the theoretical results of the present study for the damped natural frequency, relative fluid-induced shift in natural frequency, and quality factor are 10.6084 MHz, -0.3505%, and 142.7, respectively, using Eqs. (4-53) and (4-55). The corresponding results obtained from the theory in [42] are 10.6084 MHz, -0.3504%, and 143.4. Thus, the simple analytical formulas derived herein provide estimates that are in excellent agreement with the results presented in [42], although the general framework employed in the latter requires an iterative approach; the present analytical formulas have the advantage of being in closed form and, thus, more clearly demonstrate the functional dependence.

While the results of a liquid-phase axial-mode cantilever have been shown to outperform microcantilevers of alternative vibration modes and, in some cases, the ASID design, there exist some potential disadvantages of axial-mode cantilevers when compared with the more general ASID device. These include (1) the actuation/detection scheme implemented for an axial-mode cantilever would necessarily be different from that for an ASID device since the latter involves passing a current between the two pads on the two sides of the ASID [23, 24] – an option that is not available with a single cantilever; (2) an efficient axial-mode cantilever must be relatively short and wide which implies that the device may not provide a sufficiently large functionalized area for sensing applications as opposed to the relatively large sensitive area afforded by the disk in an ASID; and (3) in an ASID device the disk serves to shield the moving end of each leg so that the leg ends are not stroking directly against the fluid.

5.3. Forced-Vibration Results

In practical applications MEMS resonators in general, and the ASID device in particular, are usually driven by an external source (applied force, imposed temperature, etc.), resulting in frequency-response results from which the resonant characteristics of interest may be extracted. In particular, the resonant frequency and quality factor of the system are typically obtained from the output signal of the system. Therefore, the focus of this section is to extract these resonant characteristics from sample theoretical frequency response results for a harmonically excited ASID device in order to compare them with the ASID’s eigenproperties studied in Sect. 5.2 and to demonstrate that one may be able to analytically predict and improve the resonant behavior of an ASID immersed in a viscous fluid based by strategically modifying the system’s geometric and material parameters.

5.3.1. Frequency Response

The normalized frequency response of the ASID can be obtained by evaluating Eqs. (4-63a, b) of the continuous model or Eq. (3-20) of the SDOF model over a range of driving frequencies. While the SDOF model considers the disk rotation as the only output of the system (which is proportional to the leg strain, assumed to be uniform), the continuous model is used to provide two outputs: the disk rotation (or average leg strain) and the local strain at the supports, as described earlier through Eqs. (4-64a, b). Since the focus of the present work is on the resonant characteristics of the ASID, we provide only sample frequency response curves for a specific set of system parameters as shown in Fig. 5-12, where the moduli (i.e., magnitudes) of the complex quantities $\bar{U}(1)$ and $\bar{U}'(0)$ of Eqs. (4-64a, b) and $\bar{\theta}_0 \equiv \dfrac{\theta_0}{L\varepsilon_0/a}$ of Eq. (3-20) are being evaluated as normalized response quantities. Physically, these response quantities correspond to normalized forms of either the disk rotation (average leg strain) amplitude or the local leg strain amplitude at the supports.

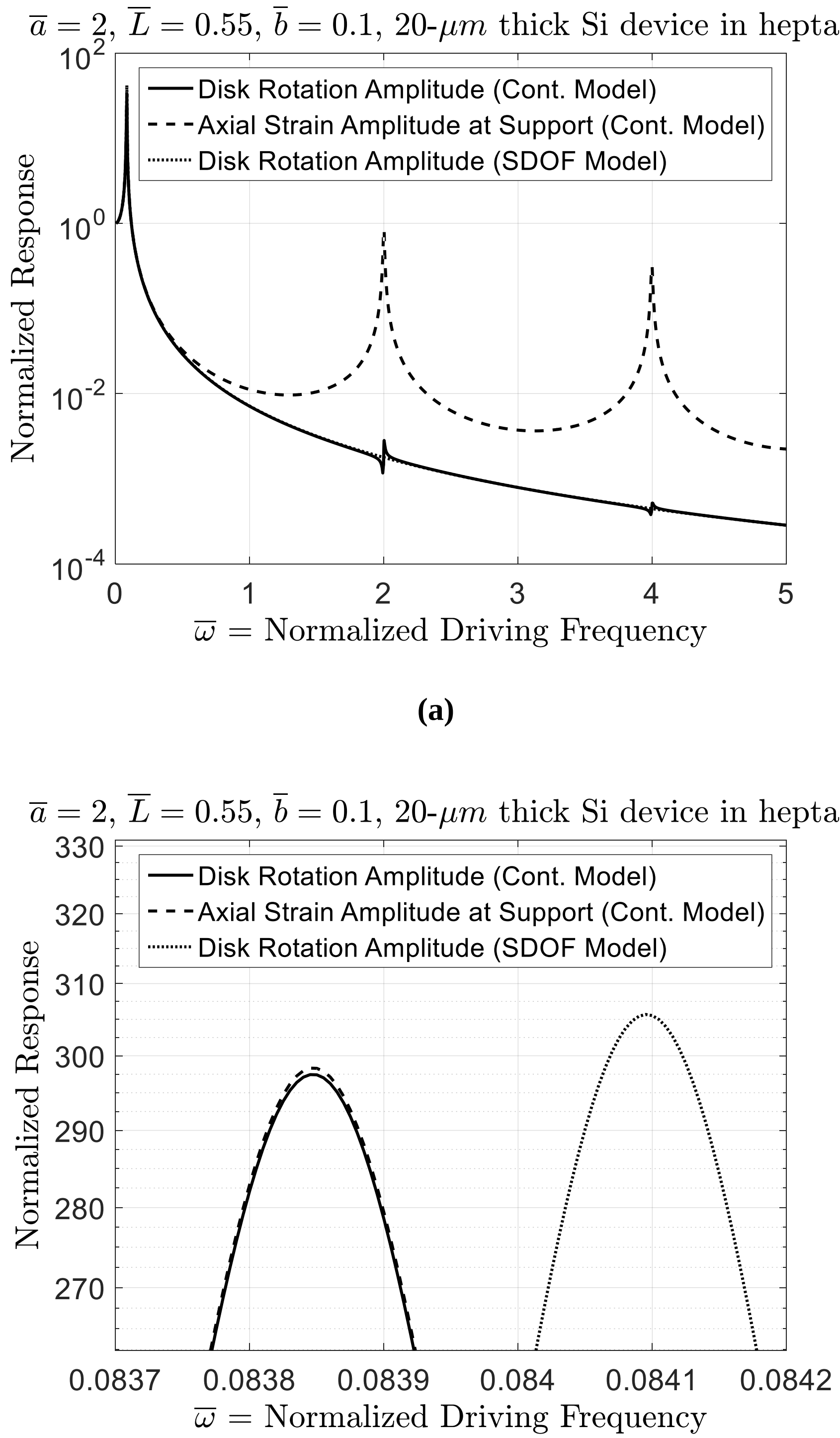

(a)

(b)

Fig. 5-12. (a) Theoretical output signals based on continuous model and SDOF model; (b) Zoomed view of signals for mode-1 response indicating slight difference between the two models.

The continuous-model curves of Fig. 5-12 show that the two output signals have virtually identical responses in mode 1, while they tend to differ significantly in higher modes, with the local strain signal being stronger. As mentioned earlier in Sect. 5.2.1, the disk rotation signal corresponds to the average strain in the legs; thus, if the legs are excited in a mode other than the fundamental mode, some portions of the legs move in opposite directions, resulting in a smaller average strain in the leg. Moreover, the smaller value of disk rotation in the higher modes suggests that the boundary condition at the leg-disk junction is approaching a fixed condition; i.e., the disk inertia is limiting the disk rotation at higher driving frequencies. A comparison of the mode-1 results of the continuous and SDOF models shows that they are indistinguishable in Fig. 5-12a, while the zoomed view provided in Fig. 5-12b shows that the two models yield slightly different results. Nevertheless, for the case considered in Fig. 5-12 the SDOF model gives excellent approximations to the resonant frequency (0.3% high) and resonant peak amplitude (2.8% high).

Due to damping in the system, the response may be shifted in time compared to the loading (i.e., the peak response and peak loading no longer occur at the same time). This phase shift can be obtained by calculating the argument of the complex quantities in Eqs. (4-64a, b) of the continuous model and Eq. (3-20) of the SDOF model. [The latter is explicitly expressed by Eq. (3-21).] The phase shift results associated with the disk rotation response (for both models) as well as the local strain at the supports (continuous model) are evaluated over a range of exciting frequencies as shown in Fig. 5-13.

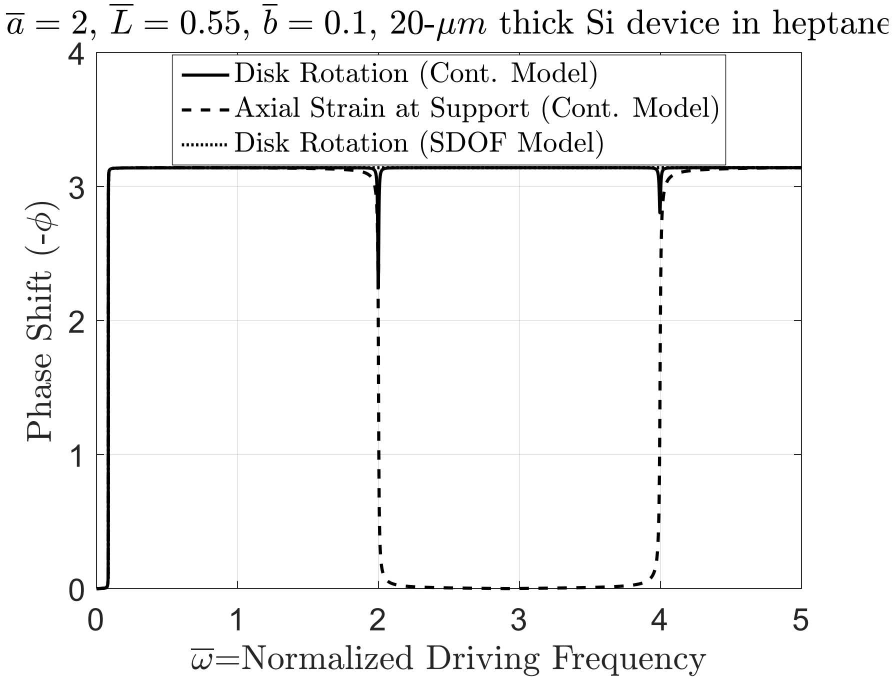
$\overline{a} = 2$, $\overline{L} = 0.55$, $\overline{b} = 0.1$, 20-μm thick Si device in heptane
Disk Rotation (Cont. Model)
Axial Strain at Support (Cont. Model)
Disk Rotation (SDOF Model)
Phase Shift (-ϕ)
0
1
2
3
4
0
1
2
3
4
5
$\overline{\omega}$=Normalized Driving Frequency

(a)

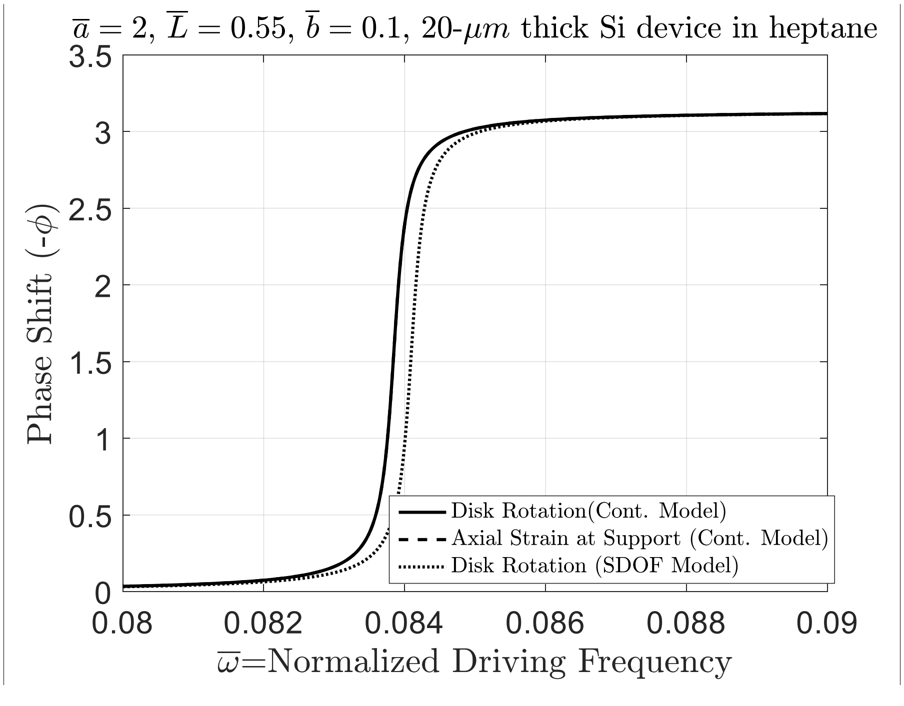
$\overline{a} = 2$, $\overline{L} = 0.55$, $\overline{b} = 0.1$, 20-μm thick Si device in heptane
3.5
3
2.5
2
1.5
1
0.5
0
Phase Shift (-ϕ)
Disk Rotation(Cont. Model)
Axial Strain at Support (Cont. Model)
Disk Rotation (SDOF Model)
0.08
0.082
0.084
0.086
0.088
0.09
$\overline{\omega}$=Normalized Driving Frequency

(b)

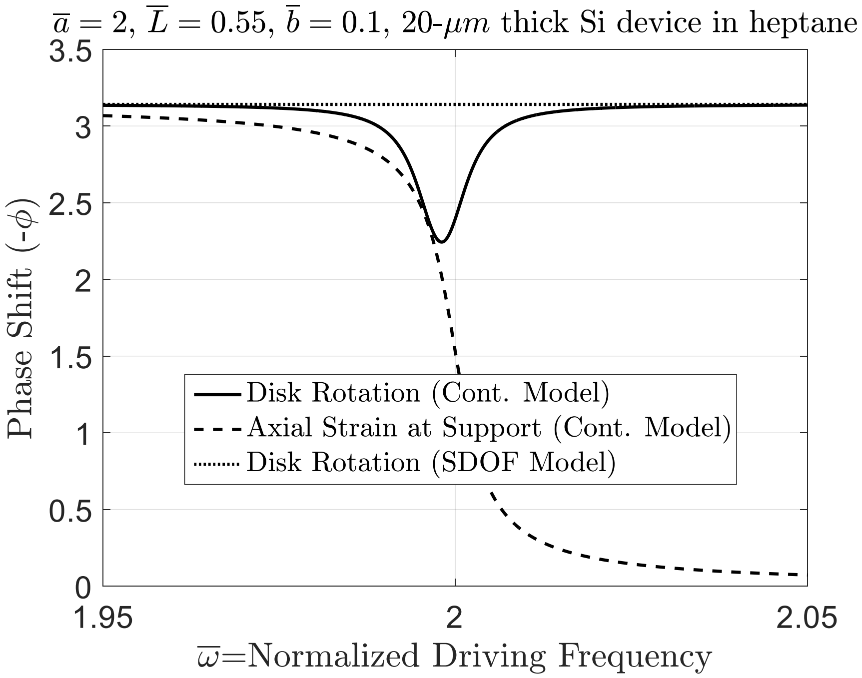

(c)

Fig. 5-13. (a) Theoretical phase shifts corresponding to two ASID output signals: disk rotation and axial strain at the supports; (b) Zoomed view of mode-1 results indicating a slight discrepancy between the two models; (c) Zoomed view of mode-2 results showing details of the phase shift associated with the disk rotation signal

The results of Fig. 5-13a indicate that the disk rotation response is approximately in phase with the exciting leg strain at driving frequencies below the first resonant frequency, while it exhibits a lag angle of π as the driving frequency increases beyond the mode-1 resonance. At higher resonances there is a “rounded spike” in the phase shift of the disk rotation signal (as shown in Fig. 5-13c) whose height tends to decrease as the mode number increases. The phase shift results corresponding to the local axial strain at the supports, however, show a repetitive pattern in which the response has a phase shift of approximately zero (i.e., the axial strain at supports is in phase with the excitation) between modes 2*n*-2 and 2*n*-1, *n* = 1, 2, 3, …, and is out of phase with respect to the excitation (phase shift near π) between modes 2*n*-1 and 2*n.* (In other words, as the exciting frequency is increased, the phase shift transitions from 0 to π when traversing an odd-mode resonance and from π to 0 when traversing an even-mode resonance.)

A zoomed view of the mode-1 phase shift curves indicates that while the SDOF model is incapable of predicting the response of the system for higher modes, it provides an excellent approximation for the mode-1 phase shift of the ASID's disk rotation response as shown in Fig. 5-13b.

5.3.2. Resonant Characteristics

With the fundamental mode of vibration being the main mode of interest in this study, the mode-1 frequency responses of the ASID for different values of $\bar{a}$ are shown in Fig. 5-14 in which the in-fluid (water in this case) responses are presented for both the SDOF and continuous models. As expected, the frequency response obtained from the SDOF model gets closer to that of the continuous model as the disk size is increased because the leg mass and associated fluid resistance effects that are neglected by the SDOF model have less impact, as opposed to their disk counterparts, on the ASID's performance when the disk is relatively large. The frequency response curves of Fig. 5-14 also demonstrate that increasing the disk size causes the peak amplitude to occur at lower frequencies. This is consistent with the free-vibration results shown in Fig. 5-1 in which the damped natural frequency of the ASID reduces when the disk gets larger. Of all the five disk radii considered in Fig. 5-14, the strongest peak (highest Q) corresponds to $\bar{a} = 2$, a result that is consistent with the critical disk size obtained for the free-vibration case that yields the relative maximum Q. (In the next section, we will extract the resonant frequency and quality factor from the frequency response of the ASID and compare them with the analytical results of the free-vibration case.)

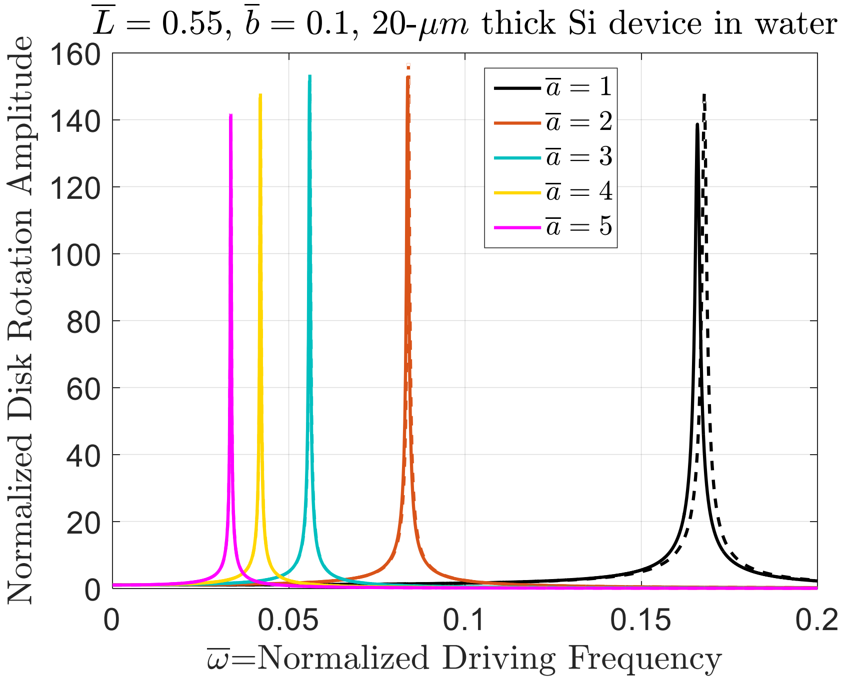

Fig. 5-14. Theoretical frequency response curves generated by the continuous model (solid) and the SDOF model (dashed) for the in-fluid (water) case. Note that the strongest peak (highest *Q*) corresponds to $\bar{a} = 2$.

While the results shown in Fig. 5-14 are for one liquid (water), it is important to note that fluids with higher viscosities may have a significant (negative) impact on the performance of the ASID. This is shown in Fig. 5-15 in which the frequency response of a 20-µm-thick Si ASID specimen is generated for different ambient fluids. (The physical properties of the liquids used in this figure are given in Sect. 5.2.2.) The results shown in Fig. 5-15 indicate that fluids with

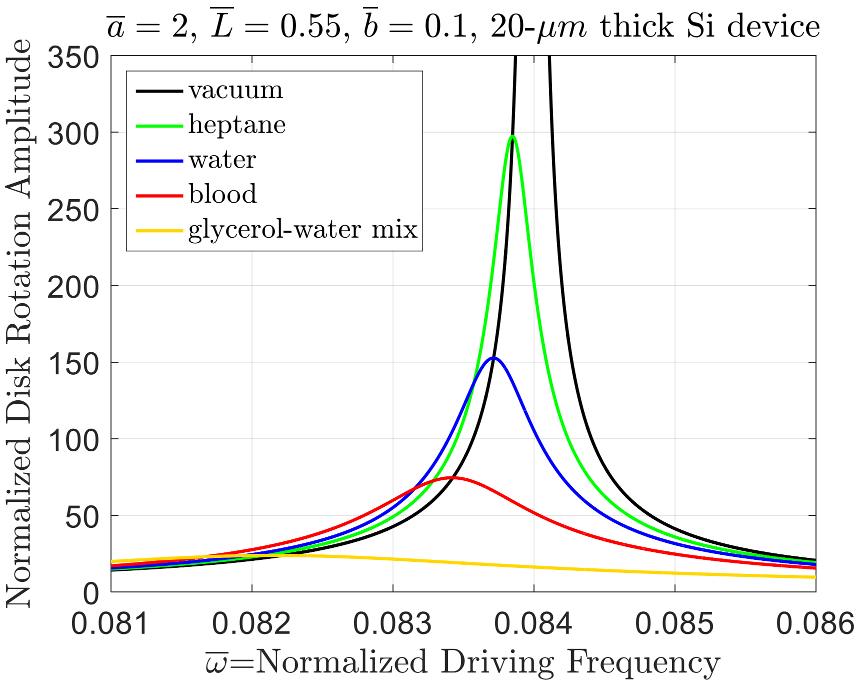

Fig. 5-15. Theoretical frequency response curves generated by the continuous model for various fluid environments.

higher density and viscosity values tend to shift the peak amplitude to the left. Moreover, they weaken the peak response amplitude significantly, resulting in a lower quality factor; for example, the quality factor in Fig. 5-15 is reduced from ~300 in heptane to ~150 in water to ~75 in blood. Two simple methods by which *Q* can be extracted from the frequency response curves will be briefly explained in the next section.

5.4. Comparison of Resonant Characteristics with Eigenproperties of the System

The free-vibration analysis of the ASID led to explicit analytical expressions for the eigenproperties of the system in terms of the basic geometric and material parameters. Assuming that the resonant characteristics of the ASID (resonant frequency and quality factor at resonance, in particular) may be approximated by the corresponding free-vibration results, one may apply the previously derived free-vibration analytical estimates to the case of a harmonically excited device. In order to confirm the validity of those analytical approximations, we will compare the resonant frequency and quality factor extracted from the frequency response results of Fig. 5-14 with the corresponding analytical estimates for both the SDOF and continuous models. Table 5-1 shows the results for the resonant frequency (i.e., the driving frequency in Hz causing peak response amplitude) of a 20-μm-thick Si ASID in water for five different disk radii and fixed leg dimensions whose frequency responses for mode 1 are generated in Fig. 5-14 along with the results obtained from the analytical expressions of the free-vibration case. The results shown in this table indicate that, over the range of disk sizes considered, the resonant frequency of the ASID can be very well predicted by the corresponding estimates obtained from the free-vibration analysis. (Reference [42] also shows that when the quality factor of a damped cantilever is sufficiently large, the in-fluid resonant frequency of the device becomes virtually identical to the natural frequency.)

Table 5-1. Comparison between the mode-1 resonant frequency extracted from Fig. 5-14 with results from Eqs. (3-22a) and (4-37) of the SDOF and continuous models.

	Resonant Frequency [MHz]			
	SDOF Model		Continuous Model	
$\bar{a}$	From Frequency Response Curve	Eq. (3-22a)	From Frequency Response Curve	Eq. (4-37)
1	28.502	28.503	28.167	28.169
2	14.254	14.254	14.211	14.211
3	9.502	9.502	9.489	9.489
4	7.126	7.126	7.120	7.120
5	5.700	5.700	5.697	5.697

Comparison between the Q results extracted from the frequency response curves of Fig. 5-14 and the corresponding analytical estimates are summarized in Table 5-2. Note that the extracted values for Q are obtained by two methods: (1) the bandwidth method, in which Q may be related to the resonant peak bandwidth through

$$Q = \frac{f_{res}}{\Delta f_{BW}} \tag{5-4}$$

where Δf_{BW} is the bandwidth at the “half-power” amplitude [90]; and (2) the resonant amplification method [90, 91], which gives Q as the peak value from the normalized frequency response curve. (The latter method comes from the dynamic response of a simple mass-spring-damper SDOF model in which the dynamic amplification factor – i.e., the ratio of the dynamic amplitude to the static deflection of the system – may be related to the quality factor when the system is driven at its resonant frequency.) Again, the Q results of Table 5-2 indicate that the quality factor of the ASID at resonance may

Table 5-2. Comparison between the quality factor extracted from Fig. 5-14 with results from Eqs. (3-22b) and (4-39) of the SDOF and continuous model, respectively.

	Q					
	SDOF Model			Continuous Model		
$\bar{a}$	From Frequency Response Curve		Eq. (3-22b)	From Frequency Response Curve		Eq. (4-39)
	Bandwidth Method	Resonant Amplification Method		Bandwidth Method	Resonant Amplification Method	
1	147.8	148.0	147.2	138.4	138.7	137.4
2	156.7	156.9	156.2	152.5	152.7	151.5
3	153.5	153.8	153.0	151.3	151.5	150.2
4	147.8	148.0	147.2	146.4	146.6	145.3
5	141.7	141.9	141.1	140.7	140.9	139.7

be predicted very well by the corresponding analytical expressions, thus furnishing researchers and engineers useful tools for preliminary design of ASID devices.

5.5. Comparison with FEA Results

In order to evaluate the accuracy of the in-vacuum frequency results obtained from the analytical modeling of the ASID for the free-vibration and forced-vibration cases, finite element analyses of the device for different geometric dimensions are performed using COMSOL. For this purpose, a 3-D model of the ASID resonator is created in COMSOL (Fig. 5-16) by employing the following assumptions: free tetrahedral elements; legs and disk are linear elastic and isotropic with Poisson's ratio of 0.28, E = 130 GPa, ρ = 2330 kg/m^3. (These properties are based on the case in which the legs are aligned with the <100> crystalline direction of silicon.)

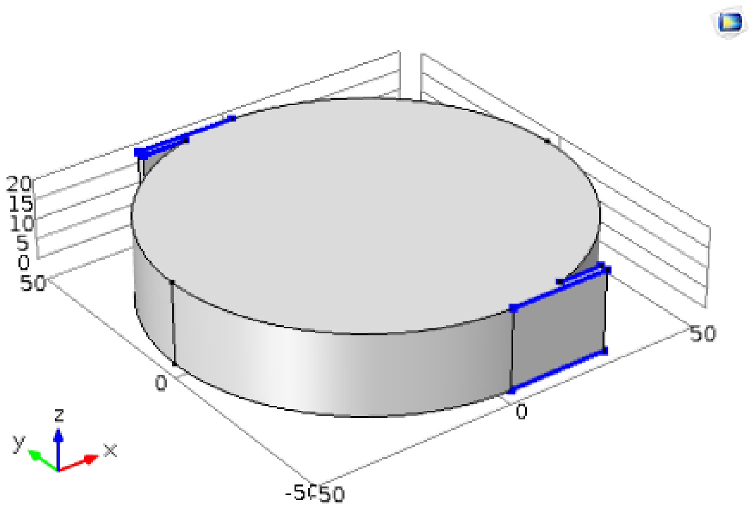

Fig. 5-16. FEA modeling of the ASID resonator in COMSOL

Note that due to different distances between the leg fixed end and the disk-leg junction for the actual device and the ambiguity in the definition of the leg length associated with published experimental data, the theoretical results provided in this section are based on two different definitions of the leg length *L*: (1) an effective leg length based on the shorter distance between the fixed end and the disk as shown in Fig. 5-17a in which the shaded portion is not considered in the modeling of the ASID; and (2) an effective leg length based on the average value of L_1 and L_2 depicted in Fig. 5-17b.

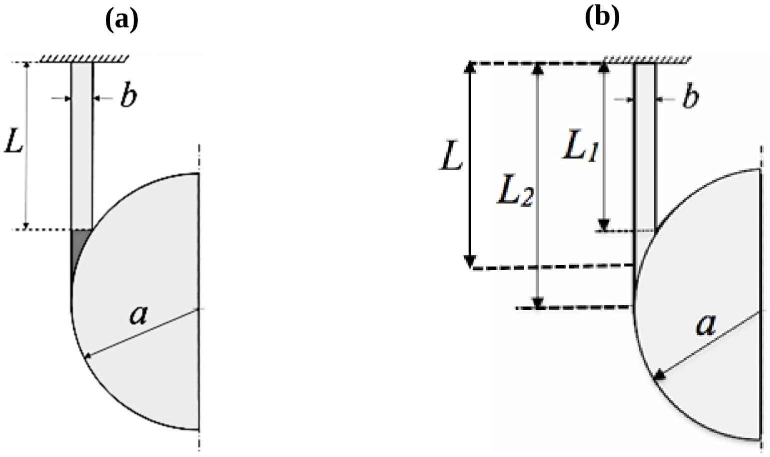

Fig. 5-17. Leg length definition based on (a) the shorter distance between the fixed end and the disk-leg junction; and (b) the average of L_1 and L_2

In-vacuum natural frequencies associated with different values of leg length and width and disk radii are obtained by performing a modal analysis of the ASID resonator in COMSOL. These FEM results are summarized in Tables 5-3a and 5-3b in which the analytical results obtained from the SDOF and continuous models (based on both definitions of leg length as described in earlier) are included for comparison. (Regarding the 3-D geometry of the ASID in COMSOL, we should note that the values of *L* listed in the tables correspond to the shortest distance between the fixed end and the leg-disk junction, i.e., the shorter of the blue edges shown in Fig. 5-16).

Table 5-3a. In-vacuum natural frequency in MHz: FEA vs. analytical (*b*=2 μm, *h*=20 μm)

a [μm]	L_1 [μm]	FEA	Analytical (avg *L*) [% error]		Analytical (short *L*) [% error]	
			SDOF	Cont.	SDOF	Cont.
50	11	9.1532	8.9429 [2.30]	9.0164 [1.49]	11.4400 [-24.98]	11.5510 [-26.20]
	17	7.8241	7.7448 [1.01]	7.7986 [0.33]	9.2022 [-17.61]	9.2797 [-18.60]
	24	6.8212	6.8145 [0.10]	6.8518 [-0.45]	7.7448 [-13.54]	7.7986 [-14.33]
	42	5.3563	5.4202 [-1.19]	5.4296 [-1.37]	5.8545 [-9.30]	5.8731 [-9.65]
100	24	3.4083	3.2559 [4.47]	3.2892 [3.49]	3.8724 [-13.62]	3.9141 [-14.84]
	35	2.9174	2.8296 [3.01]	2.8569 [2.07]	3.2066 [-9.91]	3.2393 [-11.03]
	40	2.7549	2.6842 [2.57]	2.7094 [1.65]	2.9995 [-8.88]	3.0293 [-9.96]
	55.5	2.3828	2.3449 [1.59]	2.3650 [0.75]	2.5465 [-6.87]	2.5696 [-7.84]

Table 5-3b. In-vacuum natural frequency in MHz: FEA vs. analytical

ASID Dimensions (μm)	FEA	Analytical (avg *L*) [% error]		Analytical (short *L*) [% error]	
		SDOF	Cont.	SDOF	Cont.
$a = 50$, $b = 8$, $L_1 = 70$, $h = 5$	7.0785	8.3010 [-17.27]	7.8637 [-11.09]	9.0697 [-28.13]	8.6796 [-22.62]
$a = 100$, $b = 16$, $L_1 = 100$, $h = 5$	4.1228	4.7589 [-15.43]	4.5765 [-11.00]	5.3657 [-30.15]	5.2144 [-26.48]
$a = 250$, $b = 75$, $L_1 = 400$, $h = 15$	1.5401	2.1008 [-36.41]	1.8574 [-20.60]	2.3234 [-50.86]	2.1001 [-36.36]

The good agreement between the FEA eigenfrequencies and the analytical results (especially those that are based on defining the effective leg length in an average sense) for the cases considered in Table 5-3a indicate that the effects of leg bending and disk deformation on the resonant behavior of the ASID device that are neglected in our analytical modeling are not significant. (The SDOF-model results also indicate that the leg mass has a very small influence on the natural frequency of the device when the leg width is relatively small.) However, the larger errors of the analytical results with respect to the FEA results in Table 5-3b show that when the legs are wider and longer, not only the leg mass becomes significant regarding the accuracy of the SDOF model, but also the impact of the leg bending on the response of the system becomes less negligible in that case [i.e., a wider leg results in a larger second moment of area on which the reaction moment and transverse shear force at the disk-leg junction, given by Eqs. (3-3b, c), depend].

In order to compare the natural frequency results of the ASID resonator obtained from the FEA modal analysis with the resonant frequency when the device is driven externally, a frequency-domain FEA analysis of the device is performed when the supporting legs undergo a harmonic external force. In particular, axial harmonic forces of unit amplitude per unit length of the legs (1 μN/μm) are applied on the blue edges of the legs shown in Fig. 5-16 over a range of exciting frequencies. For illustrative purposes, the (in-vacuum) FEA frequency responses of four ASID specimens chosen from Tables 5-3a and 5-3b are shown in Figs. 5-18a-d. (Dimensions of the devices are listed in each figure.)

The frequencies at which the amplitude of the ASID reaches its peak value in Figs. 5-18a-d are in excellent agreement with the corresponding eigenfrequency results of Table 5-3a and 5-3b. This is consistent with the results of Sect. 5.4 in which the resonant frequency of the ASID extracted from the theoretical frequency response curves were found to be in excellent agreement with the analytical results of the free-vibration case.

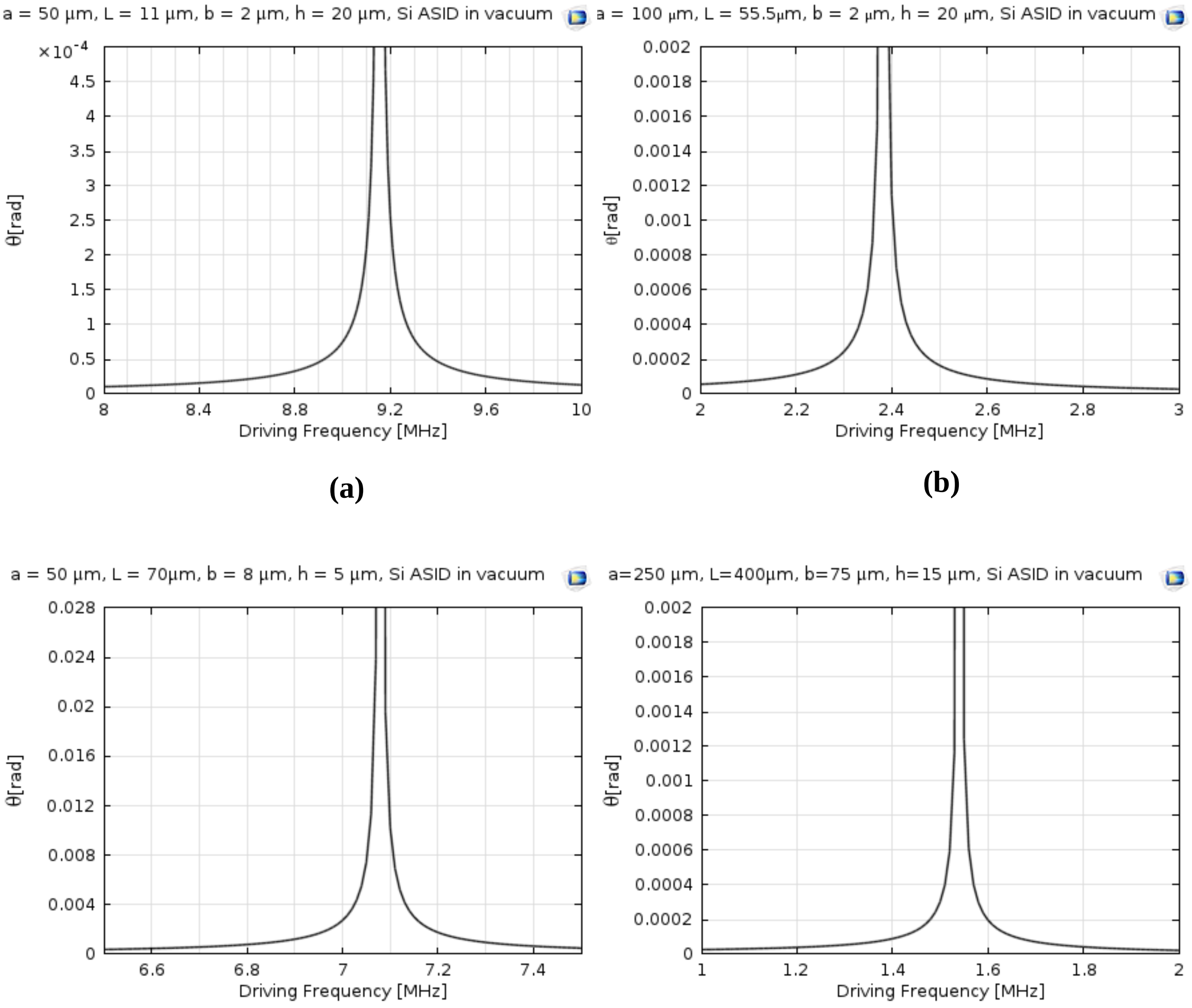

(a) **(b)**

(c) **(d)**

Fig. 5-18. FEA frequency response of the ASID under harmonic leg force

5.6. Comparison between Experimental Data and Theoretical Results of the Current Research

Our primary motivation for studying the dynamic response of the ASID resonator was to understand how the system parameters influence the efficiency of vibration in liquid environments as measured by the quality factor, *Q*. Therefore, to examine the validity of the theoretical models described in this study a comparison will be made between the theoretical predictions for *Q* and the existing liquid-phase quality factor data presented in [24] and [82] for ASID devices. While two different definitions of the leg length described in the previous section and shown in Fig. 5-17 have been used to compare the theoretical frequency results with the results obtained from the FEA modeling in the previous section, and it could be done similarly in this section as well, we employ only one definition of the leg length to compare our predicted *Q* values with the experimental data: that which is based on the minimum distance between the fixed end and the disk-leg junction (as depicted in Fig. 5-17a). The reasons for this are (1) the small portion of the leg that is attached to the disk (shaded area of Fig. 5-17a) is expected to move with the disk rotation and to contribute less to the axial deformation of the leg (i.e., this small area is located where complications neglected by the analytical models such as leg bending occurs); (2) the quality factor of the ASID does not seem to be as sensitive to the definition of leg length as the resonant frequency is. A comparison between the theoretical *Q* results of this section and the corresponding *Q* results based on the average leg length presented in [86] shows that the difference is not significant; and (3) when compared to the results of [86], the predicted *Q* results based on the minimum *L* definition are in a better agreement with the experimental data. The data of [24] correspond to 23 specimens of designs similar to that shown in Fig. 1-1, having a fixed leg width of $b = 2$ μm and various values of device thickness, disk radius, and leg length. All devices in these experiments were fabricated from silicon and measurements were made in heptane. (Details may be found in [23] and [24].) Property values used in the theoretical models for Si and heptane have been listed earlier in Sect. 5.2. The experimental Q data and the predicted values based on the continuous and SDOF models of the present study are displayed in Fig. 5-19. An immediate and encouraging observation suggested by the comparison is that nearly all of the data (markers) are bounded by the corresponding range spanned by the theoretical results (continuous curves) and that these bounds are relatively tight, especially on the high-Q side which is of most practical interest. In addition, the theoretical models capture the qualitative trends of the measured data quite well with respect to changes in both b/L and a/h. The models also provide very good quantitative estimates for Q in many cases, especially for the lower values of $\bar{a}$ which result in higher quality factors, i.e., the upper curves/markers in Fig. 5-19. In particular, the predicted Q values for the specimen that yielded the highest Q were within 3% of the measured result of 304. While no claims of optimizing the disk size were made in [24], it is interesting that the specimen that yielded the largest Q value corresponded to the lowest value of $\bar{a}$ considered in that experimental study $(\bar{a} = 2.5)$, while the present theory (continuous model), using that specimen's dimensions of $(h, b, L) = (20, 2, 11)$ μm, predicts that $\bar{a}_{cr} = 2.3$ (with a predicted Q value of 297), which is consistent with the maximum data value (Q=304). (Note that the predicted Q value for the corresponding no-disk case, i.e., when $\bar{a} = 0$, is 191 which demonstrates that the

ASID device with a critical disk size yields a much higher *Q* value in this case as opposed to the corresponding axial-mode cantilever.)

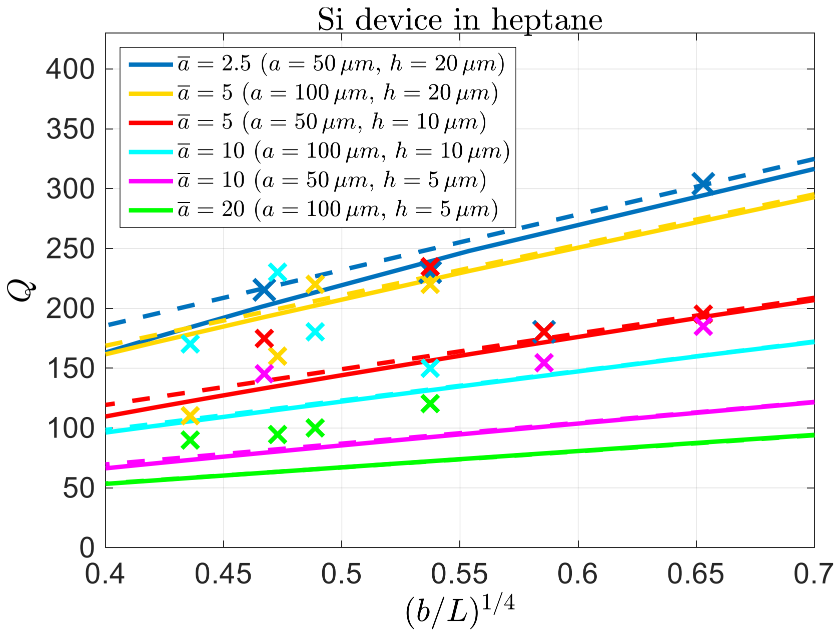

Fig. 5-19. Theoretical *Q*-factors of the ASID vs. existing data for silicon specimens in heptane [24]. (Solid: continuous model; Dashed: SDOF model; X: experiment)

The quantitative difference between theory and experiment in Fig. 5-19, however, is significant for the higher $\bar{a}$ values of 10 and 20, for which the theoretical *Q* values are 30-50% below the data in 10 of 11 cases. Possible reasons for the quantitative discrepancy are the following: (1) The theoretical results are based on the use of a room temperature value of viscosity for heptane, i.e., reduction in viscosity due to temperature effects has not been included. (2) The models neglect the mass associated with the leg-disk junctions (see shaded portion in Fig. 5-17a); underestimating the mass will result in lower predicted *Q* values. (3) The models are based on the assumption of uniform electrothermal loading in the legs, a condition which may be difficult to achieve during testing. (4) Experimental error associated with extraction of Q from noisy signals will obviously exist, as evidenced by the scatter of the data in Fig. 5-19. This error is expected to be higher for lower-Q signals.

If the two sets of theoretical curves in Fig. 5-19 are compared, one finds that, when the legs are shorter and/or the disk diameter is larger, the results of the SDOF analytical formula approach those of the continuous model, as expected, because the inertial and fluid effects associated with the legs become insignificant compared to those associated with the disk.

The theoretical quality factor results of the present study are also compared with another set of experimental data presented in [82] as summarized in Table 5-4 in which three ASID devices with different dimensions are tested in water. Note that the experimental Q values presented in Table 5-4 correspond to the “untreated” ASID specimens of [82], i.e., the results are associated with the device operating in distilled water before being exposed to other chemical solutions. (Details are given in [82].)

Table 5-4. Theoretical *Q*-factors of the ASID vs. existing data for three silicon specimens in water

	Q		
	Theory		Experiment [82]
ASID Dimensions (μm)	SDOF Model	Continuous Model	
$a = 50$, $b = 8$, $L_1 = 70$, $h = 5$	51.8	48.6	48.2
$a = 100$, $b = 16$, $L_1 = 100$, $h = 5$	43.5	41.7	54.3
$a = 250$, $b = 75$, $L_1 = 400$, $h = 15$	84.3	78.9	80.2

While the predicted *Q* values in Table 5-4 are in a good agreement with the measured data, the discrepancy between the results may be related to the reasons provided in the discussion of the *Q* results of Fig. 5-19.

Unfortunately, to the author's knowledge no experimental data has been published on the fluid-induced shift in resonant frequency for ASID devices. In lieu of direct measurements of liquid-phase resonant frequencies, the present theory may be used to estimate fluid-induced frequency shifts from the published values of measured *Q* data; these "semi-empirical" values may then be compared to the theoretical predictions of the relative frequency change. Specifically, we use the *Q* data of [24] to calculate the semi-empirical shifts in resonant frequency of the ASID based on the approximate relationship given by Eq. (3-14). A comparison between these data values and the purely theoretical predictions based on Eqs. (3-13) and (3-14) is presented in Table 5-5. The results show a good agreement between the theoretical predictions of frequency shift and the semi-empirical data for higher-*Q* ASID designs. Specifically, of the 7 ASID specimens that yield Q>200 in heptane (shown in red and green), the theoretical results for 5 cases (shown in green) are within 9% of the semi-empirical data. Possible reasons for the larger discrepancy between the theory and the *Q*-derived data for the other cases have been listed previously following the discussion of Fig. 5-19.

Table 5-5. Theoretical relative shift in resonant frequency vs. “semi-empirical” data based on measured *Q* – Si device (*b*=2 μm) in heptane.

a [μm]	*L* [μm]	*h* [μm]	Magnitude of Relative Shift in Resonant Frequency (%)			% difference (SDOF Model)	% difference (Cont. Model)
			SDOF Model (%)	Cont. Model (%)	Semi-Empirical = 1/2*Q* (%) [measured *Q* value]		
50	11	5	0.438	0.4435	0.2703 [185]	-62.0	-64.1
		10	0.256	0.26	0.2564 [195]	0.16	-1.4
		20	0.1647	0.1683	0.1645 [304]	-0.12	-2.3
	17	5	0.4882	0.4967	0.3226 [155]	-51.3	-54.0
		10	0.2853	0.292	0.2778 [180]	-2.7	-5.1
		20	0.1836	0.1896	0.2778 [180]	33.9	31.7
	24	10	0.311	0.3209	0.2128 [235]	-46.1	-50.8
		20	0.2001	0.2093	0.2174 [230]	7.9	3.7
	42	5	0.6113	0.6339	0.3448 [145]	-77.3	-83.8
		10	0.3575	0.3768	0.2857 [175]	-25.1	-31.9
		20	0.2301	0.2481	0.2326 [215]	1.1	-6.7
100	24	5	0.6884	0.6966	0.4167 [120]	-65.2	-67.2
		10	0.3767	0.3814	0.3333 [150]	-13.0	-14.4
		20	0.2201	0.2238	0.2273 [220]	3.2	1.5
	35	5	0.756	0.7673	0.5 [100]	-51.2	-53.46
		10	0.4138	0.4208	0.2778 [180]	-48.9	-51.5
		20	0.2418	0.2475	0.2273 [220]	-6.4	-8.9
	40	5	0.7815	0.7941	0.5263 [95]	-48.5	-50.9
		10	0.4278	0.4358	0.2174 [230]	-96.8	-100.5
		20	0.25	0.2567	0.3125 [160]	20.0	17.9
	55.5	5	0.8476	0.8646	0.5556 [90]	-52.6	-55.6
		10	0.4641	0.4756	0.2941 [170]	-57.8	-61.7
		20	0.2713	0.2811	0.4545 [110]	40.3	38.2

CHAPTER 6:

ASID PERFORMANCE METRICS IN MASS-BASED SENSING APPLICATIONS

6.1. Introduction

The in-fluid resonant characteristics of the ASID presented and discussed in Chs. 4 and 5 provide a theoretical basis for the resonator's performance in a viscous fluid environment. The results relating the resonant frequency and quality factor of the device to the system's material and geometric parameters may serve as the basis for achieving optimal designs of ASID-based sensors. As will be demonstrated in detail in this chapter, in sensing applications the resonant characteristics are important factors that determine the sensing performance of MEMS resonators, including the ASID sensor considered herein. The sensing performance metrics of the ASID sensor investigated in this chapter are the mass and chemical sensitivities and the mass and chemical limits of detection. In particular, in Sect. 6.2 the mass and chemical sensitivities of the ASID sensor are defined and expressed explicitly in terms of both the system parameters and the resonant response parameters. Similarly, the mass and chemical limits of detection and their counterparts per unit of functionalized sensing area are derived in Sect. 6.3. Finally, numerical results and discussion suggesting the possibilities of improving ASID-based sensor performance are presented and discussed in Sect. 6.4.

6.2. Mass Sensitivity and Chemical Sensitivity

In mass-based sensing applications, one or more surfaces of a MEMS resonator, including the ASID design considered in the present study, are coated with a chemically sensitive layer (e.g., a polymer) that serves as a sensitive film that will sorb an analyte (target substance) when exposed to a surrounding gas or liquid medium containing the analyte. Due to the sorption of the analyte by the coating, the mass of the layer will change (as may the physical properties of the coating material). The increase in the layer mass will result in an increase in the resonator's effective mass and, thus, a decrease in its natural/resonant frequencies. Indeed, this is the sensing principle on which most mass-based resonant sensors are predicated.

In order to derive expressions for the sensing performance metrics of the ASID, several assumptions are made in this chapter: (1) the sensing layer only covers the top surface of the ASID (i.e., the top surfaces of the disk and the supporting legs as shown in Fig. 6-1); (2) the Young's modulus of the coating (before and after analyte sorption) is negligible in comparison with that of the base material; (3) the changes in the fluid properties (density and viscosity) due to analyte sorption into/onto the coating are negligible, i.e., the fluid domain is relatively large in comparison with the sensor; and (4) the analyte is absorbed uniformly throughout the coating volume, and changes in the coating layer dimensions during the absorption process are neglected. Assumptions (2)-(4) imply that the only effect of the analyte sorption process on the dynamic response of the ASID is through the increased mass of the device. Employing the above

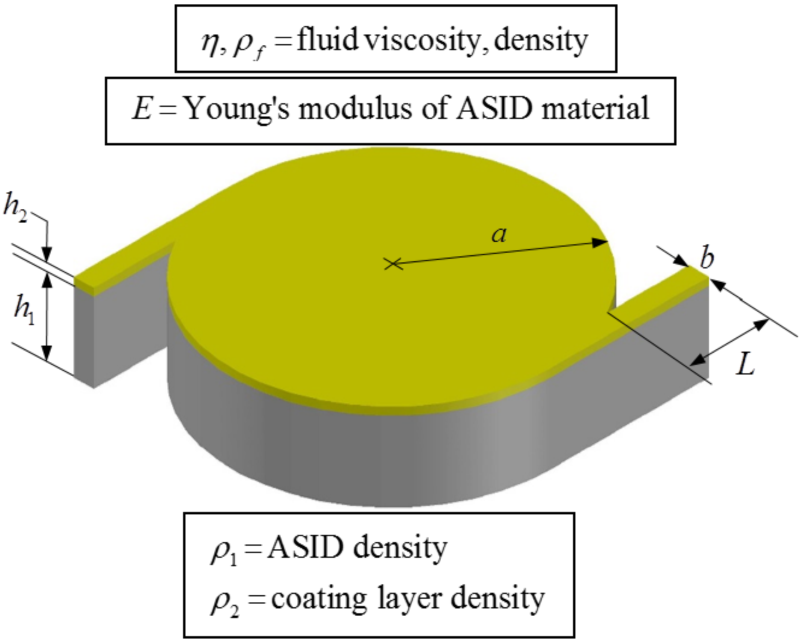

Fig. 6-1. Sensitive layer covering the top surface of the ASID device.

assumptions, the change in the mass of the ASID sensor upon analyte exposure may be monitored through the shift in resonant frequency of the actuated device. We now proceed to show in detail how one may relate the mass uptake to the resonant response, thereby relating the sensing performance metrics to the ASID design parameters and the fluid properties.

The mass sensitivity, S_m, is defined as the change in the resonant frequency with respect to a change in the sensor’s mass, *m* [92]:

$$S_m \equiv \frac{\partial f_{res}}{\partial m} = \frac{1}{V_{eff}} \frac{\partial f_{res}}{\partial \rho_{eff}} \tag{6-1}$$

where V_{eff} is the volume of the sensor and ρ_{eff} is the effective (average) mass density of the sensor, i.e.,

$$\rho_{eff} = \frac{\rho_1 h_1 + \rho_2 h_2}{h_1 + h_2} \tag{6-2}$$

where ρ_1 and ρ_2 are the densities and h_1 and h_2 are the thicknesses of the (uncoated) ASID and the sensing layer, respectively. In essence, the results derived in the earlier chapters are applicable to the case of the two-layer (i.e., coated) ASID provided that we homogenize the coated device through its total thickness as implied by Eq. (6-2) [and Eq. (6-4) to follow]. Noting that $V_{eff} = h_{eff}\left(2bL + \pi a^2\right)$ is the volume of the sensor in which the effective thickness $h_{eff} \equiv h_1 + h_2$ is simply the total thickness, Eq. (6-1) may be expressed as

$$S_m = \frac{1}{h_{eff}\left(2bL + \pi a^2\right)} \frac{\partial f_{res}}{\partial \rho_{eff}} \tag{6-3}$$

where f_{res} may be approximated by the free-vibration results of the SDOF and continuous models of the ASID described in Sects. 3.4.3 and 4.3.5, respectively. In particular, one may utilize the approximate analytical expression for the in-fluid natural frequency given by Eq. (3-22a) for the SDOF model and Eq. (4-33) for the continuous model to calculate the shift in resonant frequency due to the change in the average density of the sensor. It is important to note that the resonant characteristics of the ASID device (resonant frequency and quality factor, in particular) depend on the stiffness of the system, and since the stiffness is assumed to remain unchanged after the deposition of a coating layer on top of the device [see assumption (2) at the beginning of this section], an effective Young's modulus for the legs of the homogenized bi-layer ASID sensor is introduced:

$$E_{eff} = \frac{h_1}{h_1 + h_2} E \tag{6-4}$$

This effective Young’s modulus is smaller than that of the base material in the legs to account for the fact that the coating is assumed to have a negligible Young’s modulus. This results in the coated legs having the same axial rigidity as the uncoated legs (i.e., $E_{eff} b h_{eff} = E b h_1$). Starting with the SDOF model, Eq. (3-22a) may be rewritten in terms of the effective Young’s modulus, the average density, and the total thickness of the sensor:

$$\left(f_{res} \right)_{SDOF} = \sqrt{\frac{E_{eff} b}{\pi^3 \rho_{eff} a^2 L}} \left[1 - \left(1 + \frac{2h_{eff}}{a} \right) \left(\frac{\pi}{16} \frac{a^2 L}{b {h_{eff}}^4} \frac{\rho_f^2 \eta^2}{{\rho_{eff}}^3 E_{eff}} \right)^{1/4} \right] \tag{6-5}$$

Therefore

$$\frac{\partial \left(f_{res} \right)_{SDOF}}{\partial \rho_{eff}} = -\frac{1}{2} \sqrt{\frac{E_{eff} b}{\pi^3 {\rho_{eff}}^3 a^2 L}} \left[1 - \frac{5}{2} \left(1 + \frac{2h_{eff}}{a} \right) \left(\frac{\pi}{16} \frac{a^2 L}{b {h_{eff}}^4} \frac{\rho_f^2 \eta^2}{{\rho_{eff}}^3 E_{eff}} \right)^{1/4} \right] \tag{6-6}$$

Substituting (6-6) into (6-3) results in an explicit approximate expression for the mass sensitivity of the ASID in terms of the system’s geometric and material parameters, including those of the fluid:

$$\left(S_m \right)_{SDOF} = -\frac{1}{2} \frac{1}{h_{eff} \left(2bL + \pi a^2 \right)} \sqrt{\frac{E_{eff} b}{\pi^3 {\rho_{eff}}^3 a^2 L}} \left[1 - \frac{5}{2} \left(1 + \frac{2h_{eff}}{a} \right) \left(\frac{\pi}{16} \frac{a^2 L}{b {h_{eff}}^4} \frac{\rho_f^2 \eta^2}{{\rho_{eff}}^3 E_{eff}} \right)^{1/4} \right] \tag{6-7}$$

Since in many practical cases the fluid-dependent term in (6-7) is very small relative to the fluid-independent part, the mass sensitivity of the ASID sensor may be further simplified by neglecting the fluid term and replacing the effective thickness, density, and modulus with their definitions in terms of the constituent layer parameters:

$$
\begin{aligned}
\left(S_m\right)_{SDOF} &\approx -\frac{1}{2}\frac{1}{h_{eff}\left(2bL+\pi a^2\right)}\sqrt{\frac{E_{eff}b}{\pi^3\rho_{eff}{}^3a^2L}} \\
&= -\frac{1}{2}\frac{1}{h_1\left(2bL+\pi a^2\right)}\sqrt{\frac{Eb}{\pi^3\rho_1{}^3a^2L\left(1+\dfrac{\rho_2h_2}{\rho_1h_1}\right)^3}} = -\frac{1}{2}\frac{\left(f_{res,vac}\right)_{SDOF}}{m}
\end{aligned}
\qquad (6\text{-}8)
$$

where $\left(f_{res,vac}\right)_{SDOF}$ is the in-vacuum resonant frequency of the (bi-layer) ASID obtained from the SDOF model, and *m* is the total mass of the (bi-layer) ASID sensor. Thus, we see that when fluid effects are neglected the mass sensitivity is related to the resonant frequency and mass via the well-known relationship given by the final portion of Eq. (6-8) (e.g., [93]).

In order to show more clearly the basic functional dependence of the mass sensitivity upon the system parameters, we further assume that $\rho_2h_2 \ll \rho_1h_1$ and $2bL \ll \pi a^2$, the latter being more consistent with the SDOF model in which the mass of the legs is neglected. Thus, we obtain the following simple approximation for the mass sensitivity of the ASID sensor:

$$
\left(S_m\right)_{SDOF} \approx -\sqrt{\frac{Eb}{4\pi^5\rho_1{}^3h_1{}^2a^6L}} \qquad (6\text{-}9)
$$

Equation (6-9) demonstrates that the disk radius and the density of the device have the most impact on the mass sensitivity; moreover, the sensitivity is increased when their values are decreased. The dependence of mass sensitivity on disk size will be explored in more detail in Sect. 6.4.1, while in Sect. 6.4.3 the effects of the coating thickness and density on the mass sensitivity will be studied. The relevant SDOF result that will be used in those parametric studies is Eq. (6-8).

Similarly, one may employ the expression for the mode-*n* natural frequency obtained from the more accurate continuous model and given by Eq. (4-33). This results in

$$\begin{gathered}
\frac{\partial\left(f_{n,res}\right)_{cont.}}{\partial\rho_{eff}} = -\frac{1}{2}\frac{f_0}{\rho_{eff}}\left\{\overline{f}_{n,vac} - \frac{5}{2}\sqrt{\frac{\overline{f}_{n,vac}}{4}}\left[\frac{1+(2\Delta-1)\overline{\alpha}+\frac{\pi^2}{4}\overline{\alpha}^2\,\overline{f}_{n,vac}^{\;2}}{1+\overline{\alpha}+\frac{\pi^2}{4}\overline{\alpha}^2\,\overline{f}_{n,vac}^{\;2}}\right]\beta\right\}, \\
f_0 = \frac{\omega_0}{2\pi} = \frac{1}{4L}\sqrt{\frac{E_{eff}}{\rho_{eff}}}, \\
\beta = \frac{2}{\sqrt{\pi}}\left(1+\frac{h_{eff}}{b}\right)\left(\frac{L^2}{h_{eff}^{\;4}}\frac{\rho_f^{\;2}\eta^2}{\rho_{eff}^{\;3}E_{eff}}\right)^{1/4},
\end{gathered} \tag{6-10a-c}$$

where $\overline{f}_{n,vac} \equiv \dfrac{f_{n,vac}}{f_0} = \overline{\omega}_{n,vac}$, given by Eq. (4-21a, b), is the (density-independent) normalized mode-*n* resonant frequency of the ASID in vacuum, in which f_0 is the reference frequency given by (6-10b). Note that the reference frequency and fluid-resistance parameter in (6-10a) – and in (6-11) to follow – are based on the *effective* values of thickness, density, and Young’s modulus of the bi-layer ASID sensor. Substituting (6-10a) into (6-3) yields the mass sensitivity of the ASID sensor for an arbitrary mode *n,* based on the continuous model resonant frequency:

$$\left(S_{m,n}\right)_{cont.} = -\frac{1}{2}\frac{1}{h_{eff}\left(2bL+\pi a^2\right)}\frac{f_0}{\rho_{eff}}\left\{\bar{f}_{n,vac} - \frac{5}{2}\sqrt{\frac{\bar{f}_{n,vac}}{4}}\left[\frac{1+(2\Delta-1)\bar{\alpha}+\frac{\pi^2}{4}\bar{\alpha}^2\bar{f}_{n,vac}{}^2}{1+\bar{\alpha}+\frac{\pi^2}{4}\bar{\alpha}^2\bar{f}_{n,vac}{}^2}\right]\beta\right\} \tag{6-11}$$

By neglecting the fluid-dependent term, β, in (6-11), a more approximate expression for the mode-*n* mass sensitivity of the ASID sensor based on the continuous model may be written as

$$\begin{aligned}\left(S_{m,n}\right)_{cont.} &\approx -\frac{1}{2}\frac{1}{h_{eff}\left(2bL+\pi a^2\right)}\frac{\left(f_{n,vac}\right)_{cont.}}{\rho_{eff}} \\ &= -\frac{\bar{\omega}_{n,vac}(\bar{\alpha})}{8h_1L\left(2bL+\pi a^2\right)}\sqrt{\frac{E}{\rho_1{}^3\left(1+\frac{\rho_2h_2}{\rho_1h_1}\right)^3}} = -\frac{1}{2}\frac{\left(f_{n,vac}\right)_{cont.}}{m}\end{aligned} \tag{6-12}$$

in which the simple analytical results (4-21a, b) or (4-22a-c) may be used to determine $\bar{\omega}_{n,vac}(\bar{\alpha})$. One immediate implication from the above equation is that if the ASID sensor's dimensions are multiplied by the factor *k* uniformly, the mass sensitivity will be multiplied by $1/k^4$. Mass sensitivity results of the two models given by (6-8) for the SDOF model and (6-12) for the continuous model will be presented in Sect. 6.4.

One may also specialize (6-12) to the no-disk case by setting the disk radius equal to zero, thereby obtaining an explicit analytical expression for the mass sensitivity of an axial-mode cantilever in terms of the coated cantilever's geometric and material parameters for an arbitrary mode *n*:

$$\left(S_{m,n}\right)\Big|_{a=0} = -\frac{2n-1}{16h_1bL^2}\sqrt{\frac{E}{\rho_1{}^3\left(1+\frac{\rho_2h_2}{\rho_1h_1}\right)^3}} \tag{6-13}$$

As will be seen in Sect. 6.4.1, the parametric study on the mass sensing performance of the ASID sensor indicates that the maximum theoretical value of the mass sensitivity magnitude occurs for this special no-disk case.

The chemical sensitivity, S_c, of a sensor is defined as the change in resonant frequency with respect to a change in analyte concentration in the surrounding environment, c_A [92-94]:

$$S_c = \frac{\partial f_{res}}{\partial c_A} \tag{6-14}$$

Rewriting (6-14) in terms of the mass sensitivity (6-1) results in

$$S_c = \frac{\partial m}{\partial c_A}\frac{\partial f_{res}}{\partial m} = V_{eff}\frac{\partial \rho_{eff}}{\partial c_A}S_m \tag{6-15}$$

Note that the change in the average density of the sensor upon analyte absorption is due to the change in the density of the coating layer only. Therefore, based on Eq. (6-2), we have

$$\frac{\partial \rho_{eff}}{\partial c_A} = \frac{h_2}{h_1+h_2}\frac{\partial \rho_2}{\partial c_A} \tag{6-16}$$

Recalling that V_{eff} in Eq. (6-15) is the total volume of the sensor and placing (6-16) into (6-15) results in

$$S_c = V_2 \frac{\partial \rho_2}{\partial c_A} S_m \qquad (6\text{-}17)$$

where $V_2 = h_2\left(2bL + \pi a^2\right)$ is the volume of the coating, and the "analyte sensitivity," $\frac{\partial \rho_2}{\partial c_A}$, of the coating material with respect to the analyte (in a given ambient environment – e.g., in air or water) is related to the chemical interaction between the coating material and the analyte in the ambient environment [92]. As will be demonstrated shortly, one may easily show that $\frac{\partial \rho_2}{\partial c_A}$ is equal to the partition coefficient *K* of the analyte/coating pair (for a specific gas or liquid medium), defined by [92]

$$K \equiv \frac{c_2}{c_A} \qquad (6\text{-}18)$$

where c_A is the analyte concentration in the ambient environment and c_2 is the analyte concentration in the coating layer after chemical equilibrium has been reached. The partition coefficient given by (6-18) is a chemical equilibrium constant that characterizes the absorption behavior of a sensitive film relative to the ambient analyte, and depends on the nature of the film and the analyte, the ambient vapor pressure (i.e., the tendency of particles to escape the liquid in an equilibrium state at a given temperature), and the operation temperature [92]. The analyte concentration in the coating layer may be expressed as the ratio of the absorbed mass, Δm, to the volume of the coating:

$$c_2 = \frac{\Delta m}{V_2} \qquad (6\text{-}19)$$

By employing (6-18) and (6-19), the density of the coating layer after analyte exposure can be expressed as

$$\rho_2 = \frac{m_2 + \Delta m}{V_2} = \frac{m_2}{V_2} + c_2 = \frac{m_2}{V_2} + Kc_A \tag{6-20}$$

Taking a derivative of (6-20) with respect to c_A results in

$$\frac{\partial \rho_2}{\partial c_A} = K \tag{6-21}$$

Finally, by substituting (6-21) into (6-17), the chemical sensitivity of the device may be rewritten as a function of the mass sensitivity through the partition coefficient:

$$S_c = KV_2S_m \tag{6-22}$$

which indicates that, for a given mass sensitivity of the device, the chemical sensitivity may be improved by either using a thicker coating (increasing V_2) or using a coating material having a higher partition coefficient when used in combination with the targeted analyte.

The scaling law for the chemical sensitivity of an ASID-based sensor given by (6-22) indicates that a uniform multiplication of all of the sensor's dimensions by the factor *k* will multiply the chemical sensitivity by 1/*k*.

6.3. Limit of Detection

Following the approach of Waggoner and Craighead [93], we will now demonstrate that the mass limit of detection for an ASID-based sensor is proportional to its mass and inversely related to its quality factor. An analogous relationship for the chemical limit of detection will also be derived.

Using the definition of mass sensitivity (6-1) and its relationship to resonant frequency and sensor mass (6-8), the change in the resonant frequency due to a small added mass, Δm, is

$$\Delta f_{res} = -\frac{1}{2}\frac{\Delta m}{m} f_{res} \tag{6-23}$$

in which we are neglecting the small difference between the in-vacuum and the in-fluid resonant frequencies of the ASID. The minimum detectable added mass to the sensor, $\Delta m_{\min}$, due to analyte sorption, known as the mass limit of detection and denoted here as LOD_m, is an important measure of the sensor performance. Based on Eq. (6-23), this quantity depends on the smallest shift in the resonant frequency, $\Delta f_{\min}$, that can be measured by the sensor. The frequency shift resolution – and therefore, the mass limit of detection – is determined in large part by the quality factor Q of the sensor. As noted in Sect. 5.4, Q may be related to the resonant peak bandwidth through

$$Q = \frac{f_{res}}{\Delta f_{BW}} \tag{6-24}$$

where Δf_{BW} is the bandwidth at the "half-power" amplitude. Assuming that $\Delta f_{\min}$ is a particular fraction (denoted as κ) of Δf_{BW}, i.e.,

$$\Delta f_{\min} = -\kappa \Delta f_{BW} \tag{6-25}$$

in which κ (<1) is a positive number and the negative sign accounts for the fact that the resonant frequency will decrease due to the added mass, the following relationship is obtained:

$$\Delta f_{\min} = -\kappa \frac{f_{res}}{Q} \tag{6-26}$$

Substituting (6-26) into (6-23) leads to the following relationship between the mass limit of detection, the initial sensor mass, and the quality factor:

$$LOD_m \equiv \Delta m_{\min} = 2\kappa \frac{m}{Q} = 2\kappa \frac{\left(\rho_1 h_1 + \rho_2 h_2\right)\left(2bL + \pi a^2\right)}{Q} \approx 2\kappa \frac{\rho_1 h_1 \left(2bL + \pi a^2\right)}{Q} \tag{6-27}$$

in which the last (approximate) form is based on the assumption that the coating mass is small with respect to the base mass. (We will use this assumption in some of the following results as well.) Equation (6-27) suggests that decreasing the smallest detectable analyte mass may be achieved by reducing the device mass and/or increasing the quality factor. However, one must keep in mind that these two quantities are not independent.

By substituting the analytical expression for the quality factor obtained from the SDOF model [(Eq. (3-22b) with appropriate effective quantities for the thickness, density, and modulus] into the more exact version of (6-27), one may derive a simple, explicit expression for the mass limit of detection of the ASID sensor in terms of the basic system parameters:

$$
\begin{aligned}
\left(LOD_m\right)_{SDOF} &= 2\kappa\left[\rho_1 h_1\left(\pi a^2 + 2bL\right)\right]\left(\frac{\pi\rho_f{}^2\eta^2 L}{\rho_1{}^3 E b h_1{}^2}\right)^{1/4}\left[\frac{\dfrac{a}{h_1} + 2\left(1 + \dfrac{h_2}{h_1}\right)}{\sqrt{\dfrac{a}{h_1}}}\right]\left(1 + \frac{\rho_2 h_2}{\rho_1 h_1}\right)^{1/4} \qquad (6\text{-}28)\\
&\approx 2\kappa\left(\frac{\pi^5\rho_1\rho_f{}^2\eta^2 L}{Eb}\right)^{1/4} a^{3/2}\left(a + 2h_1\right)
\end{aligned}
$$

in which the final approximate form is based on the assumptions that the legs are much smaller than the disk ($2bL \ll \pi a^2$) and that the thickness and mass of the coating is small relative to their base-layer counterparts. Based on the approximate form of Eq. (6-28), it is clear that the mass limit of detection predicted by the SDOF model depends more strongly on the disk radius than on any other system parameter. The more exact dependence of the mass LOD on disk radius and on coating thickness/density [via the more exact form in Eq. (6-28)] will be explored in greater detail in Sects. 6.4.2 and 6.4.3, respectively.

We may also obtain an analytical formula for the mass LOD in an arbitrary mode *n* based on the continuous-system model by substituting the analytical expression for *Q* [(Eq. (4-36), based on the assumption of small fluid resistance, with appropriate effective quantities for the thickness, density, and modulus] into Eq. (6-27). In this case the explicit formula is not as simple as for the SDOF case; therefore, we do not list it here. However, for the no-disk case, the continuous model yields a relatively compact form for the LOD of an axial-mode cantilever in a viscous fluid for arbitrary mode *n*:

$$\left(LOD_{m,n}\right)\Big|_{a=0}=\frac{8\kappa bL}{\sqrt{(2n-1)\pi}}\left(\frac{\rho_1\rho_f{}^2\eta^2L^2}{E}\right)^{1/4}\left[1+\frac{h_1}{b}\left(1+\frac{h_2}{h_1}\right)\right]\left(1+\frac{\rho_2h_2}{\rho_1h_1}\right)^{1/4} \tag{6-29}$$

This form is important since, as we shall see in Sect. 6.4.2, the parametric study on mass LOD will indicate that the no-disk case will always yield the minimum value of LOD_m. We also note that the above equation suggests that the design parameter *L* has the highest impact on the mass limit of detection of a liquid-phase, axial-mode microcantilever sensor, with shorter cantilevers resulting in better mass resolution.

By virtue of (6-8), result (6-27) may also be expressed in terms of mass sensitivity via

$$LOD_m=\kappa\frac{f_{res}}{Q|S_m|} \tag{6-30}$$

In order to normalize the mass limit of detection with respect to the functionalized (coated) area of the sensor, we may alternatively define the mass limit of detection per unit area as

$$LOD_{\bar{\bar{m}}}\equiv\Delta\bar{\bar{m}}_{\min}=2\kappa\frac{\bar{\bar{m}}}{Q}=2\kappa\frac{\rho_1h_1+\rho_2h_2}{Q}\approx2\kappa\frac{\rho_1h_1}{Q} \tag{6-31}$$

where $\bar{\bar{m}}$ is the mass per unit area of the ASID sensor. The detailed forms of the mass LOD per unit area predicted by the SDOF model may be obtained by dividing the two forms in Eq. (6-28) by $\left(\pi a^2+2bL\right)$ and πa^2, respectively.

The chemical limit of detection, LOD_c, describes the smallest ambient analyte concentration that is detectable by the sensor. Noting that, based on (6-18) and (6-19),

$\Delta m = c_2 V_2 = K c_A V_2$, the mass limit of detection expression (6-27) may be converted to the chemical limit of detection:

$$LOD_c \equiv \left(c_A\right)_{\min} = \frac{1}{KV_2} LOD_m = 2\kappa \frac{m}{KV_2 Q} = 2\kappa \frac{\left(\rho_1 h_1 + \rho_2 h_2\right)}{K h_2 Q} \approx 2\kappa \frac{\rho_1 h_1}{K Q h_2} \qquad \text{(6-32)}$$

Expression (6-32) suggests that improving the LOD_c could be achieved by decreasing the total sensor mass, increasing the quality factor, increasing the volume of the coating, and/or increasing the partition coefficient. However, since all of these parameters are not independent of one another, a change in one may adversely affect another in terms of its effect on the LOD_c and the chemical sensitivity. Therefore, a balanced approach to the optimization of the ASID sensor design should be employed.

Note that, by using (6-22), Eq. (6-32) can also be expressed in terms of the resonant frequency, the chemical sensitivity, and the quality factor:

$$LOD_c = \kappa \frac{f_{res}}{Q\left|S_c\right|} \qquad \text{(6-33)}$$

It follows from (6-32) that the chemical limit of detection per unit area is

$$\begin{aligned} LOD_{\bar{\bar{c}}} \equiv \left(\bar{\bar{c}}_A\right)_{\min} = \frac{1}{KV_2} LOD_{\bar{\bar{m}}} = 2\kappa \frac{\bar{\bar{m}}}{KV_2 Q} &= \frac{2\kappa}{K} \frac{\left(\rho_1 h_1 + \rho_2 h_2\right) \Big/ \left[h_2\left(2bL + \pi a^2\right)\right]}{Q} \\ &\approx 2\kappa \frac{\rho_1 h_1}{K Q h_2 \left(2bL + \pi a^2\right)} \end{aligned} \qquad \text{(6-34)}$$

Note that if all of the ASID sensor's dimensions are uniformly multiplied by *k*, the mass and chemical limits of detection, LOD_m and LOD_c, will be multiplied by $k^{5/2}$ and $1/\sqrt{k}$, respectively. Thus, each order-of-magnitude miniaturization of the ASID results in an improvement in the mass limit of detection, reducing it by 99.7%, but results in a poorer chemical LOD that is roughly tripled.

6.4. Parametric Study on ASID Sensor Performance

The purpose of this section is to perform a parametric study on the performance metrics (sensitivity and LOD) of an ASID sensor and to discuss the qualitative and quantitative trends exhibited by the sensor. In particular, this section seeks to examine the effects of the material and geometric parameters of the ASID on its sensing performance in order to provide guidelines for maximizing its mass-detection capabilities in viscous liquid environments. Detailed results will be presented and discussed for mass sensitivity and mass limit of detection. However, as noted in the previous two sections, since the trends in these mass-based performance measures may easily be related to their chemical-sensing counterparts via Eqs. (6-22), (6-32), and (6-34), relevant comments regarding chemical-sensing performance of the ASID will also be included in Sects. 6.4.1 and 6.4.2. It should be noted that the graphical results to be presented in Sects. 6.4.1 and 6.4.2 are based on the assumptions that the coating thickness and coating mass are much smaller than their base-material counterparts. However, the effects of the coating’s thickness and mass on the mass sensitivity and mass limit of detection of the sensor are studied separately and in some detail in Sect. 6.4.3 and comments related to chemical sensing are also furnished.

6.4.1. Mass Sensitivity

When the ASID sensor is exposed to the (gas or liquid) environment, the resonant frequency of the sensor is expected to drop due to the mass uptake and this dependence is characterized by the mass sensitivity. The variation of the theoretical mass sensitivity of a silicon ASID sensor with respect to the normalized disk size is shown in Fig. 6-2 in which the results of both the SDOF model [Eq. (6-8)] and continuous model [(Eq. (6-12)] are included. In both cases the coating mass is assumed to be negligible in comparison with the base-material (silicon) mass.

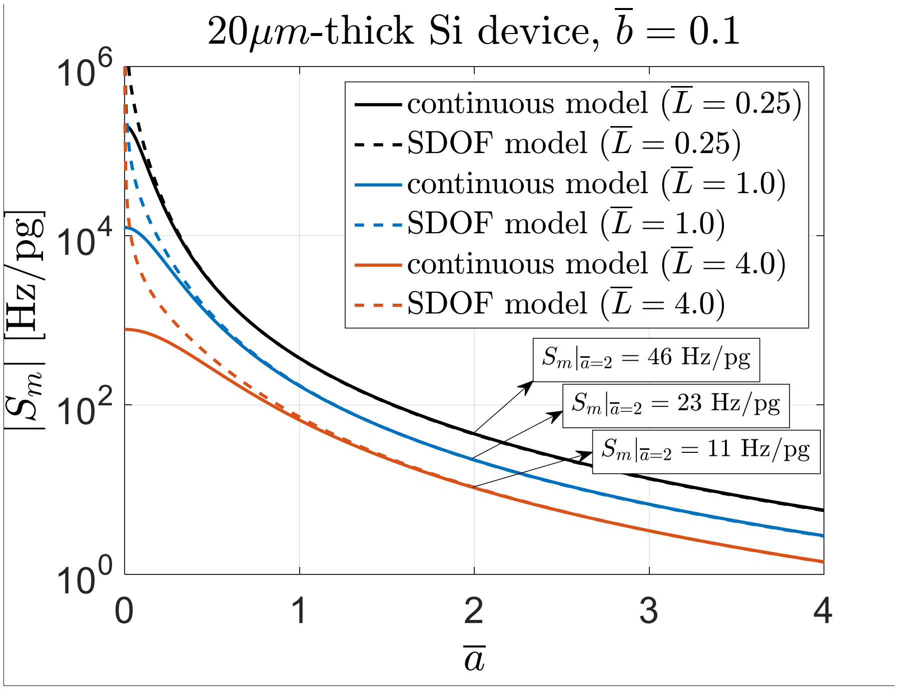

Fig. 6-2. Mass sensitivity of a Si ASID sensor ($\rho = 2330\ \text{kg/m}^3$, $E = 130$ GPa) with respect to the normalized disk radius: SDOF model vs. continuous model (mode 1)

Also note that the value of the normalized leg width is fixed at 0.1 in the figure, but several values of normalized leg length are considered. While the SDOF model fails at small $\bar{a}$ values (as expected), the discrepancy between the mass sensitivity results of the two models tends to decrease for larger $\bar{a}$ values. Based on Fig. 6-2, the maximum mass sensitivity occurs at $\bar{a}=0$ (i.e., the no-disk case) for the device parameters considered. In fact, by setting the derivative of Eq. (6-12) with respect to $\bar{a}$ equal to zero, one may prove that the highest mass sensitivity will always correspond to the no-disk case. The analytical expression for this maximum mass sensitivity (or the mass sensitivity of an axial-mode microcantilever) for an arbitrary mode *n* is given by Eq. (6-13). Figure 6-2 also demonstrates that shorter legs result in a higher mass sensitivity for the ASID sensor, as does the simple estimate given by Eq. (6-9). In particular, the quantitative comparison of S_m for the three ASIDs with different leg lengths at $\bar{a}=2$ is shown in Fig. 6-2. Those values show that, if the legs get shorter by a factor of 4, the mass sensitivity increases by a factor of 2 (approximately). Equation (6-9) clearly shows this $1/\sqrt{L}$ dependence.

Equation (6-12) also enables us to calculate the mass sensitivity of the ASID sensor for higher modes. Theoretical results of S_m for the first three modes are shown in Fig. 6-3 in which a quantitative comparison of the results at $\bar{a}=2$ (a practical, efficient disk size for the ASID design in terms of quality factor) indicates a much higher mass sensitivity for modes 2 and 3 compared to that of the fundamental mode. This is a reflection of the fact that, for a given ASID

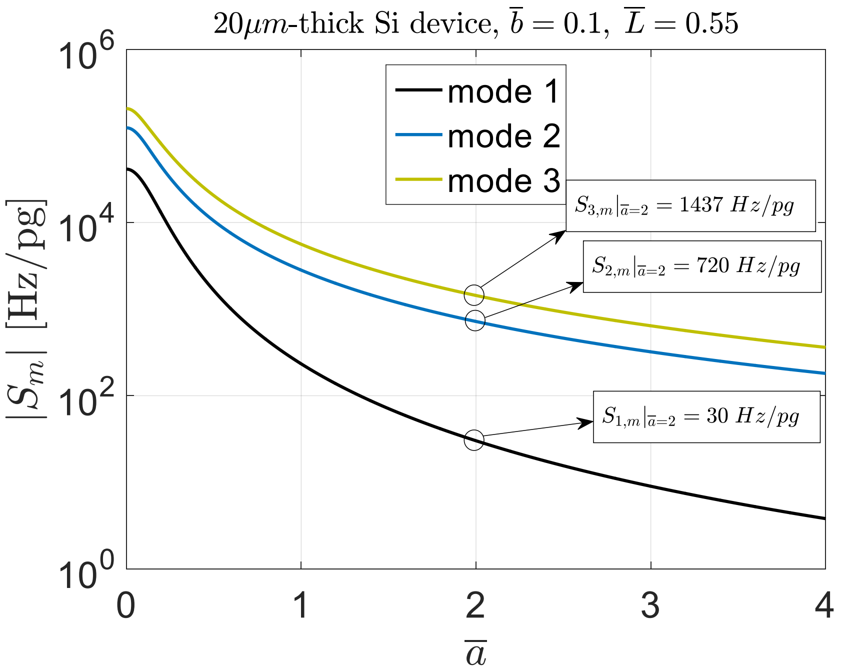

Fig. 6-3. Mass sensitivity of a Si ASID sensor ($\rho = 2330$ kg/m^3, $E = 130$ GPa) for the first three modes: continuous model

specimen (i.e., fixed mass), the resonant frequency of the device increases significantly when it is operated at higher modes, and therefore the increase in mass sensitivity is expected. However, higher-mode operation of the system could be problematic in practice since the detection of the (weaker) output signals (e.g., local leg deformation or disk rotation amplitude) could become difficult.

While the numerical results of this section are limited to mass sensitivity, one may easily perform a similar parametric study on the chemical sensitivity of the ASID sensor by using Eq. (6-22). Such a study will also show that the highest chemical sensitivity for an ASID corresponds to the limiting case of an axial-mode cantilever sensor (i.e., the special no-disk case of the ASID).

6.4.2. Mass Limit of Detection

As explained earlier in Sect. 6.3, the smallest detectable sorbed mass into/onto the ASID sensor may be characterized by the mass limit of detection of the device, a quantity that is proportional to the ratio of the total device mass to the quality factor of the resonator. This section includes graphical results demonstrating how the mass limit of detection, calculated using the more exact forms of Eq. (6-28) for the SDOF model and Eq. (6-27) for the continuous model, varies with respect to particular system parameters and mode number. (In the case of the continuous model, the calculation of Q is based on Eq. (4-36).) However, the results of this section are based on the assumptions that the coating thickness is small with respect to the base material (silicon) thickness and, as was the case in the previous section, that the coating mass is negligible in comparison with the base-material mass. (Coating thickness and mass effects will be considered in the section that follows.)

Focusing on the continuous-model results [Eq. (6-27)] shown in Fig. 6-4 for a silicon ASID of fixed thickness and various leg dimensions and immersed in either heptane or in water, we see that the mass LOD of the sensor increases as the disk size is increased. The reason that the LOD_m increases monotonically with $\bar{a}$ is that, for a given set of leg dimensions, the quality factor of the ASID tends to decrease initially as the disk gets larger (see Fig. 5-6); therefore, the mass LOD of the sensor for small values of $\bar{a}$ clearly increases (i.e., increase in mass and decrease in Q results in a higher LOD_m). For larger values of $\bar{a}$, however, the quality factor of the device increases with increasing $\bar{a}$ until it reaches a relative maximum near $\bar{a} = 2$. However, the increase in total mass of the device increases quadratically with disk radius, thereby dominating the effect of increasing Q in this range of $\bar{a}$. This results in the "optimal-Q" disk size being different from the "optimal-LOD_m" disk size. In fact, as can be seen in the inset of Fig. 6-4, the no-disk case theoretically corresponds to the minimum-LOD_m case (and this appears to always be true); thus, the analytical result derived earlier for the mass LOD of an axial-mode cantilever [Eq. (6-29)] may be quite useful. From a physical standpoint, one may simply explain that, as the sensor's mass gets smaller, it is easier for the sensor to "feel" smaller analytes; therefore, as the disk gets bigger, the mass resolution of the ASID sensor is expected to increase (get worse). Figure 6-4 also suggests that the detrimental effects of a viscous liquid such as water on the LOD_m performance of the sensor can be offset to some extent by utilizing shorter, wider legs (i.e., stiffer legs) while retaining the same value of functionalized area on each leg (*bL*). For example, for a given $\bar{a}$ value and a particular liquid, Fig. 6-4 shows that the LOD_m is reduced (improved) approximately by a factor of 2 if the L/b ratio is decreased by a factor of 16, i.e., in going from the red curves to the magenta curves or from the blue curves to the green curves. This relatively insensitive dependence [roughly $LOD_m \propto \left(L/b\right)^{1/4}$] is indicated by the simple estimate of Eq. (6-28) as well. It should be noted that the SDOF-model LOD_m results of Fig. 6-4 are based on the more exact form of Eq. (6-28); moreover, as a result of the assumptions behind the SDOF model (zero leg mass), the SDOF results in Fig. 6-4 yield a meaningless infinite LOD_m value for the no-disk case.

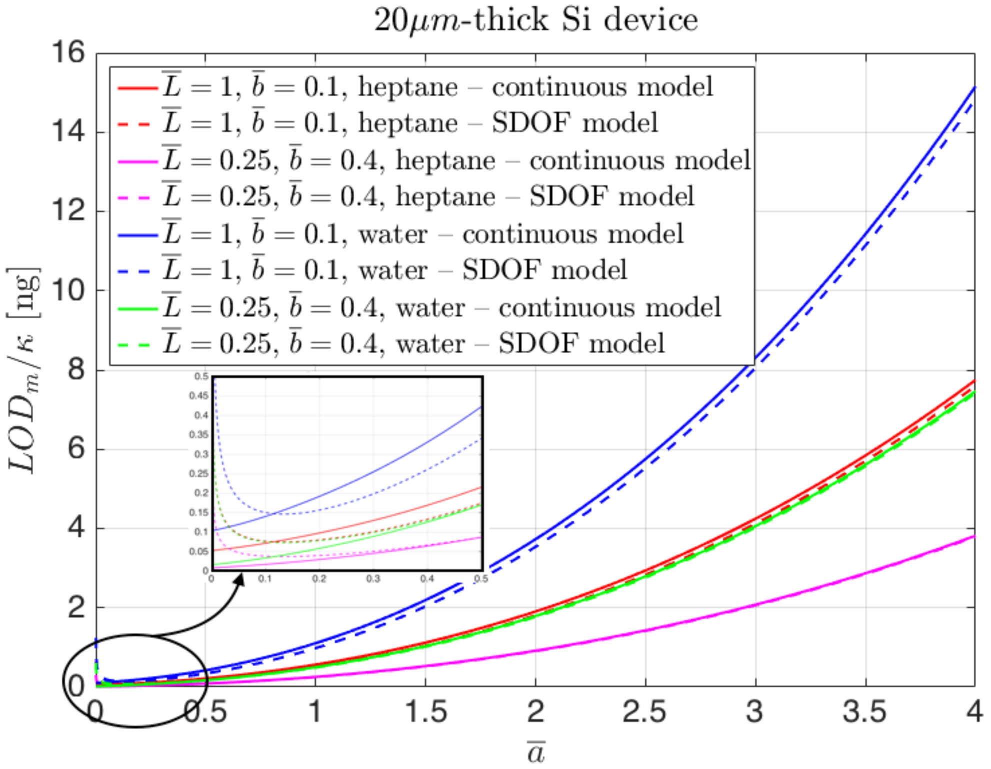

Fig. 6-4. Normalized mass limit of detection vs. disk size – continuous model (mode 1), Si ASID sensor ($\rho = 2330$ kg/m^3, $E = 130$ GPa) in heptane ($\rho_f = 679.5$ kg/m^3, $\eta = 0.000386$ Pa.s) and in water ($\rho_f = 1000$ kg/m^3, $\eta = 0.001$ Pa.s)

Results for the mass limit of detection of the ASID sensor for the first three modes are shown in Fig. 6-5 in which the LOD_m of a 20μm-thick Si device ($\overline{L} = 0.55$, $\overline{b} = 0.1$) operating in water is plotted against the normalized disk radius. While mode 3 exhibits better (lower) mass LOD than the lower modes, mode-2 results show slightly higher mass LOD than those of mode 1 when $\overline{a} > 1$ (approximately). This is because the quality factor of the specific ASID specimen examined in Fig. 6-5 has higher values in mode 1 compared to mode 2 over the approximate range of $1 < \overline{a} < 5.3$, regardless of the system material properties. (See Fig. 4-7 of Ch. 4.) The zoomed view portion of Fig. 6-5 for small $\overline{a}$ values, however, indicates that not only mode 2 yields better mass LOD results compared to mode 1, but also the improvement in LOD_m from mode 1 to mode 2 is larger than that of mode 2 to mode 3. In particular, the percentage improvement in LOD_m at $\bar{a} = 0$ (axial-mode microcantilever sensor) by operating the device at higher modes may be directly obtained from Eq. (6-29). Simple calculations based on that equation show that the LOD_m of an axial-mode cantilever decreases by 42% in going from mode 1 to mode 2, while this improvement reduces to 23% (from mode 2 to 3) and 15% (from mode 3 to 4).

It may also be of interest to examine the trend in the LOD_m results of the first three modes for relatively large values of $\bar{a}$. (For example, the ASID devices fabricated in [24] corresponded to $\bar{a}$ values as large as 20.) Although not graphically shown herein, the mode-1 LOD_m of the ASID sensor eventually becomes larger than the mode-2 result as the disk size gets larger and the slope of the mode-1 curve becomes larger than the others. This may be explained by observing the Q results of the ASID for modes 1-3 shown in Fig. 4-7. As the disk radius is increased (beyond the optimal-Q size), mode-1 Q of the ASID decreases gradually, theoretically approaching zero for an infinitely large disk, while the mode-2 and mode-3 Q values approach non-zero values. [Note the asymptotic formula for Q, Eq. (4-42).] Therefore, increase in mass and (monotonic) decrease in Q_1 result in a higher mass LOD for mode 1 with larger rates of change (slope and curvature) in comparison with modes 2 and 3 at large values of $\bar{a}$.

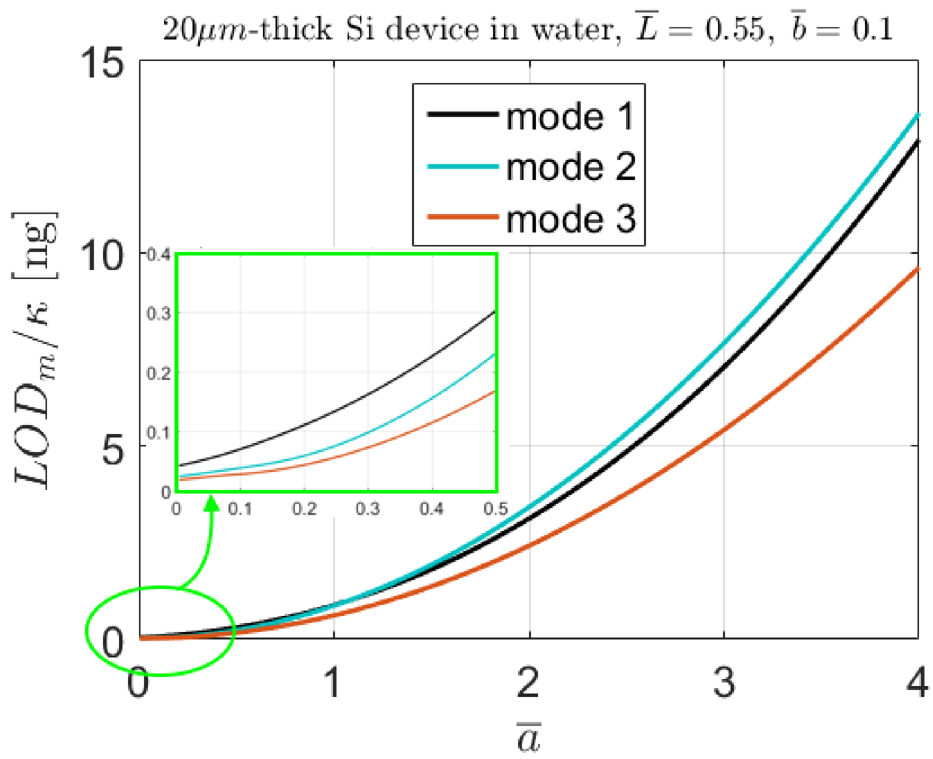

Fig. 6-5. Normalized mass limit of detection vs. disk size – continuous model (modes 1-3), Si ASID sensor ($\rho = 2330\ \text{kg/m}^3$, $E = 130$ GPa) in water ($\rho_f = 1000\ \text{kg/m}^3$, $\eta = 0.001$ Pa.s)

While the no-disk case of the ASID sensor (axial-mode cantilever) appears to minimize the mass LOD, the dependence of the ASID's chemical LOD on disk size exhibits a different behavior with respect to the disk size (not shown herein). In fact, as Eq. (6-32) clearly implies, the only a-dependent term in the equation (Q) results in the chemical LOD of the ASID sensor having a relative minimum at the critical disk size (which corresponds to the relative maximum in Q) and which, for sufficiently slender legs, will be the global minimum value in the chemical LOD.

6.4.3. Effect of Coating Thickness and Density on ASID Mass Sensing Performance

Depending on the thickness and composition of the coating, the performance of the sensor might be significantly improved or compromised. As stated earlier in the introduction of Sect. 6.4, the effects of coating thickness and mass have been neglected in the results of Sects. 6.4.1 and 6.4.2. Therefore, in the present section the effects of a 2µm-thick coating with different densities (associated with three types of polymers) on the mass sensitivity and mass LOD of a 20µm-thick Si ASID sensor will be examined.

In Fig. 6-6 the mass sensitivity [given by Eq. (6-8) for the SDOF model and Eq. (6-12) for the continuous model] is plotted vs. the coating thickness, from which it may be observed that the sensitivity decreases as the coating thickness is increased and does so in a linear fashion over this range of coating thickness. Increasing the coating thickness only adds to the total mass of the sensor in a linear manner (recall we are ignoring any stiffening effect of the coating), thus resulting in a lower S_m value by virtue of reducing the resonant frequency and increasing the mass. [See Eq. (6-8) or (6-12).] This mass effect results in the approximately linear variation of S_m with respect to coating thickness in Fig. 6-6. In fact, the more detailed form of Eq. (6-8) or (6-12) shows that the following proportionality may be used to estimate the change in the mass sensitivity of the ASID sensor due to the deposition of a small-mass coating:

$$S_m \propto \left(1+\frac{\rho_2 h_2}{\rho_1 h_2}\right)^{-3/2} \approx 1-\frac{3}{2}\frac{\rho_2 h_2}{\rho_1 h_2} \quad , \qquad \frac{\rho_2 h_2}{\rho_1 h_2} \ll 1 \ . \tag{6-35}$$

The above approximation is based on a truncated Taylor's series expansion of S_m as a function of $\frac{\rho_2 h_2}{\rho_1 h_2}$ about 0, resulting in the linear estimate.

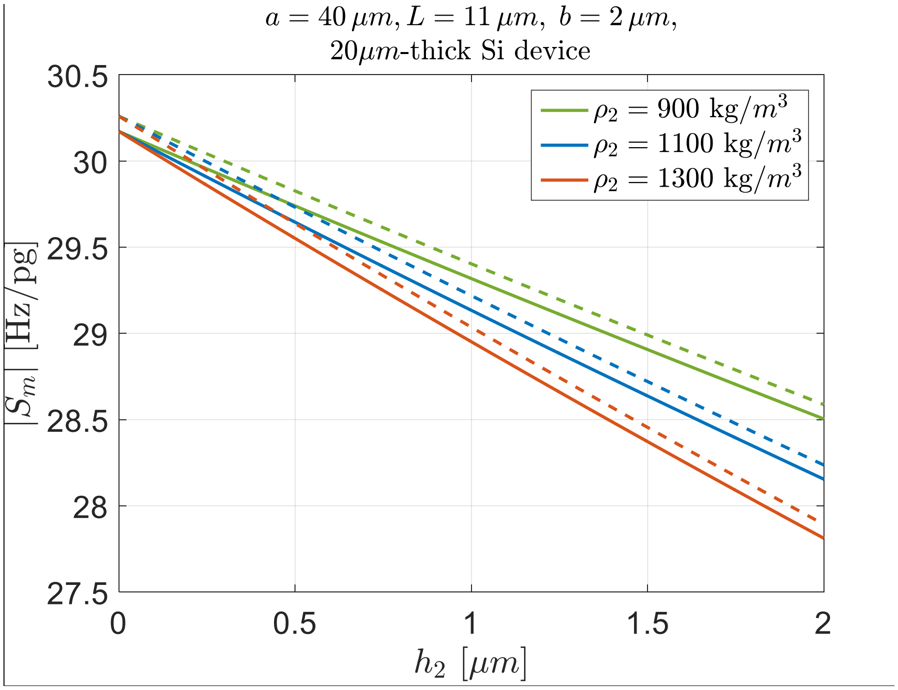

Fig. 6-6. Mass sensitivity of a Si ASID sensor ($\rho = 2330$ kg/m^3, $E = 130$ GPa) vs. coating thickness – mode-1 continuous model (solid) and SDOF model (dashed)

Figure 6-6 also suggests that the rate of the reduction in S_m (with respect to coating thickness) can be lowered by choosing a coating material with a relatively low density – a conclusion that is consistent with Eq. (6-35) as well. Observation of the change in mass sensitivity of the ASID sensor due to the deposition of the coating layer, however, shows that adding a thin layer to the device does not affect S_m significantly. For example, in Fig. 6-6 the mass sensitivity decreases by no more than 8% for a coating thickness that is up to 10% of the base-layer thickness. [Note that the effect of the coating thickness on the chemical sensitivity of the ASID sensor will be more significant as h_2 will have a higher impact on S_c via the coating volume factor in Eq. (6-22).] Regarding the results of the two models in Fig. 6-6, it is apparent that the SDOF model overestimates the mass sensitivity results of the continuous model since the SDOF model yields smaller device mass (or higher resonant frequency values) as it neglects the mass of the ASID supporting legs.

The variation of the mass limit of detection of the ASID sensor with respect to the coating thickness and density is shown in Fig. 6-7 for the fundamental mode. The continuous-model results are based on the form of Eq. (6-27) that includes the coating effects in which Q is based on the continuous model [Eq. (4-36) in which the effective thickness, density, and modulus are used in calculating the fluid-resistance parameter β], and the SDOF-model results are based on the more exact version of Eq. (6-28). The addition of a coating on top of the device increases both the total mass of the system and the quality factor of the device. However, since the increase in sensor mass is the dominant effect, the mass LOD increases with the coating layer thickness. The (nearly) linear relationship between the mass limit of detection of the ASID sensor and the coating layer thickness may be explained by recalling the analytical expression for mode-1 Q from the continuous model given by (4-39). Since the LOD_m is proportional to $\frac{m}{Q}$ [see Eq. (6-27)], it may be easily shown – by neglecting the h_2-dependence of Δ in Eq. (4-39) and employing the Taylor series expansion about $h_2/h_1 = 0$ – that

$$\left(LOD_m\right)_{cont.} \propto \left[1+\frac{h_1}{b}\left(1+\frac{h_2}{h_1}\right)\right]\left(1+\frac{\rho_2 h_2}{\rho_1 h_1}\right)^{1/4} \approx 1+\frac{h_1}{b}+\frac{h_1}{b}\left(1+\frac{1}{4}\frac{\rho_2}{\rho_1}\right)\frac{h_2}{h_1} \qquad (6\text{-}36)$$

Similarly, one may also employ the SDOF-based analytical expression for LOD_m given by (6-28), resulting in

$$\left(LOD_m\right)_{SDOF} \propto \left[\frac{\frac{a}{h_1}+2\left(1+\frac{h_2}{h_1}\right)}{\sqrt{\frac{a}{h_1}}}\right]\left(1+\frac{\rho_2 h_2}{\rho_1 h_1}\right)^{1/4} \approx \frac{\left(\frac{a}{h_1}+2\right)}{\sqrt{\frac{a}{h_1}}}+\left[\frac{2+\frac{1}{4}\frac{\rho_2}{\rho_1}\left(\frac{a}{h_1}+2\right)}{\sqrt{\frac{a}{h_1}}}\right]\frac{h_2}{h_1} \qquad (6\text{-}37)$$

The final portion of Eq. (6-36) or (6-37) clearly indicates the linear variation of LOD_m as a function of h_2/h_1 . Moreover, similar to the mass sensitivity results shown in Fig. 6-6,

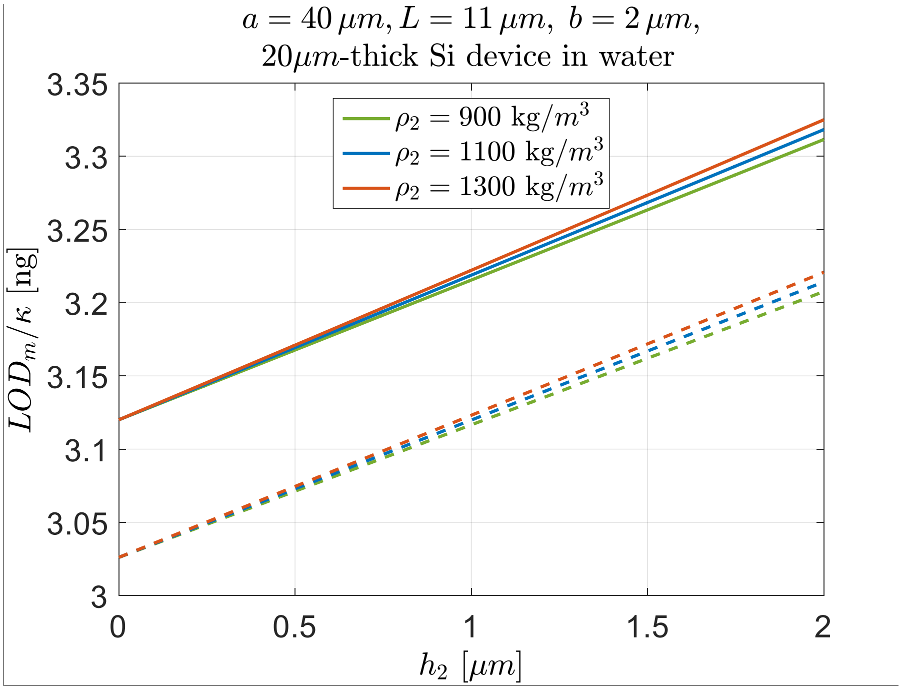

Fig. 6-7. Normalized mass limit of detection vs. coating thickness – mode-1 continuous model (solid) and SDOF model (dashed), Si ASID sensor ($\rho = 2330$ kg/m^3, $E = 130$ GPa) in water ($\rho_f = 1000$ kg/m^3, $\eta = 0.001$ Pa.s)

Eqs. (6-36), (6-37), and the graphical results of Fig. 6-7 also show that a coating with a relatively low density would result in a slightly better LOD_m performance in this case as well. However, as was the case for the mass sensitivity, the thickness and density of a thin coating on the device appear to have an insignificant effect on the value of the LOD_m of the ASID sensor. [In the case of chemical LOD, the coating thickness is expected to have a larger effect due to the direct impact of h_2 on LOD_c in the denominator of Eq. (6-32).] We also note that the results of the SDOF model show lower LOD_m values compared to those of the continuous model. This is due to the fact that, for this value of the disk size, the SDOF model underestimates the device mass and overestimates the quality factor, thus resulting in a lower mass LOD.

While several assumptions underlie the theoretical results of this chapter, the functional dependence of the mass sensing metrics of the ASID sensor on the system's geometric and material parameters sheds light on which design parameters have the most impact on the mass sensitivity and mass limit of detection. Depending on the applications and objectives, a more exhaustive parametric study of the sensing performance of the ASID sensor may be performed in a manner analogous to the approach employed in this chapter. Such a study may provide important guidelines for the optimization of liquid-phase MEMS sensors based on either ASID designs or axial-mode cantilever designs. It would also be straightforward to perform such a study on the chemical-sensing performance (i.e., the chemical sensitivity and chemical LOD) by utilizing the relationships derived earlier to relate mass-sensing performance to chemical-sensing performance [Eqs (6-22) and (6-32)].

CHAPTER 7:

SUMMARY, CONCLUSIONS, AND RECOMMENDATIONS FOR FURTHER STUDY

7.1. Summary

A new analytical approach to a novel high-performance, liquid-phase microdisk resonator supported by two tangentially-oriented legs, described in this research as an “all-shear interaction device” or ASID, has been explored through the use of two detailed theoretical models. The proof-of-concept of such a device was demonstrated by experimental data [23, 24] showing unprecedented levels of quality factor for a fully-immersed device, which provided motivation for the present work. In what follows is a summary of the research performed in this dissertation.

A single degree-of-freedom (SDOF) or lumped-parameter model was first developed to describe the fundamental in-plane rotational oscillation of the disk in a viscous fluid for free-vibration and forced-vibration cases. This relatively simple model was developed based on several major assumptions – the most important being the use of a Stokes-type fluid resistance model on the disk, the assumption that the mass and associated fluid resistance on the legs are negligible, and the treatment of the legs as pure axial members (no bending). The mathematical formulation of the SDOF model based on the aforementioned assumptions enabled the derivation of relatively simple analytical estimates for (a) the underlying in-fluid eigenproperties (natural frequency and quality factor) of the ASID for the free-vibration case, and (b) the in-fluid forced-vibration response of the device due to uniform, harmonic, electrothermal (stress-free) strains being imposed in an in-phase manner on the two actuated legs.

The SDOF model was subsequently generalized by developing a more accurate continuous-system or distributed-parameter model capable of simulating multi-modal response. With the leg mass and associated fluid resistance effects included, the mathematical formulation of the continuous model resulted in BVPs governing the (axial) free and forced vibrations of the legs in which the disk effects were incorporated via appropriate boundary conditions applied at the ends of the legs. The solution to the free-vibration case led to a complex-valued frequency equation whose solution resulted in approximate analytical expressions for the damped natural frequency, the decay parameter, and eventually the quality factor of the system in terms of the device and fluid parameters for an arbitrary mode of vibration involving axial leg vibration and in-plane disk rotation. Motivated by its potential to serve as a separate high-performance device, the in-fluid axial vibration of an isolated leg (cantilever), considered as the special no-disk case of the ASID, was also included in the free-vibration case of the continuous model, thereby enabling the derivation of analytical estimates for the in-fluid eigenproperties of an axial-mode microcantilever. For the forced-vibration case of the continuous model, a mathematical formulation based on the application of eigenstrains to the legs led to the complex-valued frequency-dependent steady-state response of the system, permitting one to extract the in-fluid resonant characteristics (resonant frequency and quality factor) from the frequency response of the system corresponding to a (mechanical) output signal at any location in the leg. Two specific output signals included in the study were the disk rotation (which is proportional to the average axial strain in each leg) and the axial strains in the legs at the supports. For validation purposes, the theoretical results obtained from both analytical models were compared to the results of FEA modeling for natural/resonant frequency and to existing experimental data for quality factor.

Finally, the analytical results obtained from the SDOF and continuous models were used to examine the performance metrics of ASID-based sensors in mass-detection sensing applications. More specifically, the mass and chemical sensitivities and mass and chemical limits of detection (LOD) of ASID-based resonant sensors were explicitly related to the resonant characteristics of the ASID and, thereby, to the system's geometric and material parameters.

7.2. Conclusions

The main objectives of the present research were to derive explicit relationships between the resonator and sensing performance of the ASID-based device and the fundamental system parameters, i.e., the device's material and geometric parameters and the fluid density and viscosity. This provided a strong theoretical basis upon which one may be able to maximize the performance of ASID-based resonant sensors in practical applications. To this end, the major conclusions and contributions of the present study are listed below:

(1) The in-fluid eigenproperty results obtained from the free vibration of the ASID for both the SDOF and mode-1 continuous models were in excellent agreement with the corresponding in-fluid resonant characteristics extracted from the frequency response of the device for the forced-vibration case in which external

harmonic eigenstrains were applied to the support legs. This enables analytical predictions (using either model) of the resonant behavior of the device over wide ranges of the system's fundamental parameters.

(2) Comparisons between the results of approximate analytical expressions for the resonant characteristics, based on the assumption of small fluid resistance effects, and the "exact" results (based on numerical solutions to the frequency equations) for both models demonstrated that the ASID concept (minimizing the device's engagement with the surrounding liquid) results in high accuracy of the small-fluid resistance analytical formulae when compared with the more exact theoretical results. This is true for the analytical estimates of both resonant frequency and quality factor for most liquids.

(3) The very important assumption that distinguishes the SDOF model from the continuous model, i.e., the assumption that the leg mass and associated fluid effects are negligible, was shown to be the main reason for the discrepancies between the (mode-1) results of the two models. More specifically, the approximate analytical formula for the fundamental frequency of the ASID based on the SDOF model explicitly indicates that the resonant frequency is (approximately) inversely proportional to disk radius a, thus yielding a theoretical (and meaningless) value of infinity as the disk radius approaches zero. This point was also clearly shown by the graphical results. The failure of the SDOF model to generate accurate results at relatively small values of $\bar{a} \equiv a/h$ – compared to the (mode-1) results of the continuous model –was also seen in the results of the fluid-induced shift in resonant frequency and quality factor, the latter incorrectly

yielding a zero value when the disk radius becomes zero. Therefore, care must be taken to avoid applying the SDOF results for cases involving small values of *a*/*h*. However, the discrepancy between the results of the two models decreases as the disk size is increased because an increase in the disk size causes the mass and fluid effects associated with the disk to be dominant relative to their leg counterparts. For this reason, the simple results of the SDOF model provide excellent estimates of the more exact results of the continuous model in the fundamental mode, provided that the disk radius is sufficiently large in comparison with the device thickness. Observations indicated that this is the case if the disk radius is greater than or equal to the device thickness.

(4) With the exception of the aforementioned differences between the two models at small disk radii, both models show similar trends for the mode-1 resonant frequency of the ASID as a function of the geometric parameters. In particular, the resonant frequency decreases as the disk size is increased due to the effect of the larger device mass on frequency. The fundamental frequency is also shown to increase in a nearly linear fashion with increases in the parameter $\sqrt{b/L}$ due to the stiffening of the legs.

(5) Based on the results obtained from the continuous model, resonant frequency of the ASID at modes 2 and higher was seen to be relatively insensitive to the disk size, approaching a constant value for each mode as this geometric parameter gets larger. This behavior was found to be consistent with the intuitive understanding of the system dynamics at higher modes, i.e., the vibrational behavior of each ASID leg at modes 2 and higher becomes similar to that of a fixed-fixed axial

member whose one end is perfectly fixed and the other end is attached to a disk that barely moves (due to the disk's significant inertia and very small vibration amplitude in higher modes).

(6) While the resonant frequency of the ASID decreases when switching from vacuum to a viscous fluid medium, and it was shown that the most viscous and densest liquid reduces the frequency by the most, this reduction in resonant frequency was found to vary in a non-monotonic fashion with respect to the disk size. This leads to the existence of a relative minimum in the magnitude of the relative shift in resonant frequency as a function of $\bar{a}$, with this relative minimum often being a global minimum as well. Based on the specific cases considered in the parametric study herein, it was found that the magnitude of the fluid-induced shift in resonant frequency can be lowered significantly by designing an ASID-based device with stiffer (wider and shorter) support legs, or by operating the device at higher modes, regardless of the fluid properties. The relative fluid-induced decrease in resonant frequency of the ASID was also found to be (approximately) proportional to $1/(2Q)$ in any mode, so that knowing one of these quantities, i.e., the relative shift in resonant frequency or the quality factor, permits the estimation of the other.

(7) Regarding the effects of the material properties on the performance of the system, the approximate proportionality of Q to $1\big/\sqrt{\overline{L}_0} = \left[\left(h^2 E \rho^3\right)\big/\left(\rho_f{}^2 \eta^2\right)\right]^{1/4}$ suggests that immersion in a liquid with low viscosity and density or using a structure made of a material with a large Young's modulus or density will improve the quality factor of the ASID in a viscous fluid environment. The theoretical models

also enable one to map the performance of an ASID resonator made of one material measured in one liquid environment into resonant behaviors of an ASID made of a different material operating in different liquids without performing additional experiments in the other material system.

(8) The functional dependence of Q on the disk size based on the SDOF model indicated a relative maximum value for Q at the critical value of $\bar{a} = 2$ (a disk whose radius is twice as the device thickness). However, for the practical range of design parameters considered, the more accurate continuous model showed that, depending on the leg dimensions, the global maximum of the quality factor may or may not correspond to the relative maximum in Q. The continuous model showed that the critical disk size yielding the relative maximum in Q has a lower bound of $\bar{a} = 2$ and that this critical disk radius increases with increasing leg length and/or decreasing leg width (i.e., it increases as the legs become more flexible). On the other hand, the relative maximum value of Q increases as the legs become stiffer (larger b and/or smaller L) in a manner that is given approximately by $Q \propto (b/L)^{1/4}$ according to the SDOF theory.

(9) Regarding the ASID disk size, the global maximum value of Q with respect to this geometric parameter can correspond to either an ASID device with the critical disk size or an axial-mode microcantilever (i.e., the no-disk case of the ASID). The results illustrated that if the legs are relatively slender, the global Q_{max} occurs for the ASID device, and if the legs are relatively stiff, the global Q_{max} will correspond to the special case of the axial-mode cantilever. More specifically, an

approximate criterion for the leg slenderness indicated that if $\bar{L} > 4\pi^3 \frac{\bar{b}^3}{\left(1+\bar{b}\right)^4}$, then the ASID will achieve a higher viscous *Q* in liquids.

(10) The in-fluid eigenproperties of an axial-mode microcantilever obtained from a detailed analysis of the no-disk special case demonstrated that an axial-mode cantilever is a potentially attractive alternative to the other modes of vibration of liquid-phase microcantilevers (transverse flexure, lateral flexure, or torsion) for high-*Q* applications in viscous fluid environments.

(11) The comparison between the theoretical resonant frequencies of the ASID and the results obtained from FEA modeling showed that using different definitions of the leg length (i.e., minimum distance between the fixed end and the disk-leg junction, and the average value of the two distances) alters the theoretical results significantly, as it resulted in larger errors for the frequencies based on taking *L* to be the minimum length dimension. While the quality factor does not seem to be as sensitive to this parameter (leg length) as is frequency, comparison between the theoretical quality factors based on the minimum *L* definition and the experimental data showed that the results of both theoretical models reproduce the trends exhibited by the data. Those results give good quantitative estimates for *Q*, especially for those ASID geometries that exhibit the highest quality factors and are therefore of most interest in resonator applications. The theoretical models predict that the highest measured *Q* value of 304 for an ASID in heptane may possibly be further increased by optimizing the geometric parameters of the device. Comparisons between the theoretical fluid-induced shift in resonant

frequencies of the ASID with “semi-empirical” data (i.e., theoretical $\Delta f/f$ values based on measured Q data) showed good agreement for the higher-Q cases but for other cases exhibited discrepancies associated with the larger errors between theoretical and measured Q (as expected).

(12) Derivation of the analytical expressions for the performance metrics of ASID-based resonant sensors for mass-based sensing applications and the parametric study of the mass sensitivity and mass limit of detection led to the following conclusions:

- Similar to the resonant characteristics results, the sensing performance metrics of the ASID sensor based on the SDOF model tend to deviate from those of the continuous model as the disk size gets smaller, yielding meaningless infinity results for the mass sensitivity and mass limit of detection at $\bar{a} = 0$.
- Mass sensitivity of an ASID-based sensor decreases as the disk radius is increased. In other words, with respect to this geometric parameter, the mass sensitivity associated with the axial-mode cantilever (the special no-disk case) yields the highest value. Moreover, mass sensitivity of the ASID sensor decreases when the leg length is increased. The results of the continuous model also show that operating the ASID at higher modes improves the mass sensitivity significantly. However, these modes are significantly stiffer than the fundamental mode and may therefore be difficult to actuate in practice.

- Mass limit of detection of an ASID-based sensor increases as the disk size is increased; therefore, the lowest mass LOD corresponds to the no-disk case. Moreover, the analytical formula for the mass LOD of the no-disk case (axial-mode cantilever) indicated that the cantilever length has the highest impact on this sensing metric, with shorter cantilevers resulting in better mass resolution. Since the effects of the surrounding fluid have negative effects on the mass LOD, it was found that such detrimental effects on the mass LOD performance of the ASID-based sensor can be offset to some extent by utilizing shorter and wider (i.e., stiffer) legs while retaining the same value of functionalized area on each leg for analyte detection.
- The fact that the highest mass sensitivity and lowest mass LOD values correspond to the no-disk case of the ASID (i.e., an axial-mode cantilever) means that the "optimal-Q" disk size may be different than the "optimal-S_m" and "optimal-LOD_m" disk size.
- The thickness and density of a relatively thin coating deposited onto the device for mass sensing purposes appears to have an insignificant influence on the values of mass sensitivity and mass LOD. For example, for the cases examined, mass sensitivity of an ASID sensor decreases by no more than 8% and mass LOD increases by no more than 7% for a coating thickness that is up to 10% of the base-layer thickness.
- While the parametric study was limited to the mass-based measures, it may easily be shown that the highest chemical sensitivity of the ASID

sensor will always occur for the axial-mode cantilever (the special no-disk case), whereas the chemical LOD of the ASID sensor will have a relative minimum value at the critical disk size (i.e., for the disk radius yielding the relative maximum in Q). This relative minimum value in the chemical LOD will also be a global minimum for an ASID design having sufficiently slender legs as given approximately by criterion (5-1).

(13) The resonant response of a liquid-phase axial-mode cantilever was shown to outperform microcantilevers of alternative vibration modes and, in some cases, the ASID design. However, there exist some potential disadvantages of axial-mode cantilevers when compared with the more general ASID device including (a) the actuation/detection scheme implemented for an axial-mode cantilever would necessarily be different from that for an ASID device since the latter involves passing a current between the two pads on the two sides of the ASID [23, 24] – an option that is not available with a single cantilever; (b) an efficient axial-mode cantilever must be relatively short and wide which implies that the device may not provide a sufficiently large functionalized area for sensing applications as opposed to the relatively large sensitive area afforded by the disk in an ASID; and (c) in an ASID device the disk serves to shield the moving end of each leg so that the leg ends are not stroking directly against the fluid.

(14) The scaling laws for the resonant characteristics and sensing performance metrics of an ASID-based resonator/resonant sensor show that a uniform increase or decrease in all of the device dimensions by a factor k will change $\Delta f/f$, Q, S_m, S_c, LOD_m, and LOD_c by the factors $1/\sqrt{k}$, $\sqrt{k}$, $1/k^4$, $1/k$, $k^{5/2}$, and $1/\sqrt{k}$, respectively.

Thus, miniaturization of the ASID will cause improvements in S_m, S_c, and LOD_m while $\Delta f/f$, Q, and LOD_c will become less desirable (larger, smaller, and larger, respectively). Therefore, depending on the application, maximizing the performance of the ASID device requires a balanced approach among these various performance measures.

7.3. Recommendations for Future Study

The theoretical research performed for this dissertation may be extended and/or supplemented in the future via one or more of the following suggested studies:

- The assumption of the Stokes-type fluid resistance model that was employed in this study to account for the fluid effects on the surfaces of the ASID device originates from the classical solution of Stokes's second problem for the in-plane translational oscillation of a rigid sheet in contact with a viscous fluid. Because this Stokes-type fluid resistance model ignores effects associated with surfaces of finite size (e.g., edge effects) and/or non-planar surfaces, incorporation of a more accurate hydrodynamic function into the modeling of the ASID device may be pursued in an effort to develop a more accurate fluid resistance model.
- The comparison of the theoretical resonant frequencies with the results of the FEA modeling showed that when the leg width is relatively large, the error of the present theory with respect to the FEA results increases. Since the large error in this case might be due to the bending in the legs that is neglected in the present analytical modeling, a more rigorous mathematical model,

including the effects of leg bending, may be warranted to improve the theoretical results.

- The FEA modeling in this work was limited to the in-vacuum case. Therefore, the validity of the in-fluid results of the theoretical models developed in this research may be achieved through the implementation of an in-fluid FEA model of the ASID, e.g., by modeling the device via the Fluid-Structure Interaction (FSI) module in COMSOL that simulates the vibrational response of the system in an “actual” liquid.
- While the effects of the thickness and density of the coating layer on the mass sensitivity and mass LOD of an ASID-based sensor were studied in the present research, the elastic and/or viscoelastic properties of the coating material were ignored. Since these properties could have a significant effect on the sensing performance metrics, one may wish to develop future models in which these are taken into account.
- The leg slenderness criterion that dictates which device (ASID or axial-mode microcantilever) will achieve a higher quality factor in liquids is approximate in the sense that the Q_{max} formula obtained from the SDOF model was compared to the Q expression of an isolated leg. Therefore, a more accurate criterion may be derived by employing the more general Q formula obtained in the continuous model.
- The new theory developed in this study demonstrated the efficiency of the ASID device for resonator and sensing applications, and therefore provides additional motivation for more experimental investigations on the ASID-type

resonators/sensors. To date, the existing data appears to be limited to a small number of studies by a single research group [23, 24, 82-84].

REFERENCES

[1] Maluf, N., *An Introduction to Microelectromechanical Systems Engineering*, Artech House, Incorporated, 2004.

[2] Bogue, R., “MEMS Sensors: Past, Present, and Future,” *Sensor Review*, Vol. 27, No. 1, pp. 7-13, 2007.

[3] Smith, C., “Piezoresistive Effects in Silicon and Germanium,” *Physical Review,* Vol. 94, No. 1, 1954.

[4] Mason, W. P., and Thurston, R. N., “Use of Piezoresistive Materials in the Measurement of Displacement, Force, and Torque,” *Journal of the Acoustical Society of America*, Vol 29, pp.1096–1101, 1957.

[5] Feynman, R., “There’s Plenty of Room at the Bottom,” *Caltech Engineering and Science*, Vol. 23, pp 22-36, 1960.

[6] Binnig, G., Quate, C. F., and Gerber, C., "Atomic-Force Microscope," *Physical Review Letters*, Vol. 56, pp. 930–933, 1986.

[7] Thundat, T., Warmack, R., Chen G., and Allison, D., “Thermal and Ambient-Induced Deflections of Scanning Force Microscope Cantilevers,” *Applied Physics Letters,* Vol. 64, No. 21, pp. 2894-2896, 1994.

[8] Bogue, R., “Recent Developments in MEMS Sensors,” *Sensors Review*, Vol. 33, No. 4, pp. 300-304, 2013.

[9] Roundy, S., Wright, P., and Rabaey, J., “A Study of Low level Vibrations as a Power Source for Wireless Sensor Nodes”, Vol. 26, No. 11, pp. 1131–1144, 2003.

[10] Anton, S., and Sodano, H., “A Review of Power Harvesting Using Piezoelectric Materials (2003–2006),” *Smart Materials and Structures*, Vol. 16, No. 3, 2007.

[11] Priya, S., and Inman, D. (eds.), *Energy Harvesting Technologies*, Springer US, 2009.

[12] Beeby, S., and White, N., *Energy Harvesting for Autonomous Systems*, Artech House, 2010.

[13] Beeby, S., “Energy Harvesting Devices,” Ch. 18 of *Resonant MEMS. Fundamentals, Implementation and Application (Advanced Micro and Nanosystems, Vol. 11),* Brand, O., Dufour, I., Heinrich, S. M., and Josse, F. (eds.), Wiley-VCH Verlag, pp. 451-472, 2015.

[14] Campanella, H., *Acoustic Wave and Electromechanical Resonators*, Artech House, 2010.

[15] Hunt., H. K., and Armani, A. M., “Label-Free Biological and Chemical Sensors,” *Nanoscale*, Vol. 2, No. 9, pp. 1544–1559, 2010.

[16] Fanget, S., Hentz, S., Puget, P., Arcamone, J., Matheron, M., Colinet, E., Andreucci, P., Duraffourg, L., Myers, Ed., and Roukes, M. L., "Gas Sensors Based on Gravimetric Detection – A Review," *Sensors and Actuators B: Chemical*, Vol. 160, No. 1, pp. 804–821, 2011.

[17] Braun, T., Barwich, V., Ghatkesar, M. K., Bredekamp, A. H., Gerber, C., Hegner, M., and Lang, H. P., "Micromechanical Mass Sensors for Biomolecular Detection in a Physiological Environment," *Physical Review E*, Vol. 72, pp. 031907-1–031907-9, 2005.

[18] Arlett, J. L., Myers, E. B., and Roukes, M. L., "Comparative Advantages of Mechanical Biosensors," *Nature Nanotechnology*, Vol. 6, pp. 203–215, 2011.

[19] Beardslee, L. A., Brand, O., and Josse, F., "Resonant MEMS Chemical Sensors," Ch. 15 of *Resonant MEMS. Fundamentals, Implementation and Application (Advanced Micro and Nanosystems, Vol. 11)*, Brand, O., Dufour, I., Heinrich, S. M., and Josse, F. (eds.), Wiley-VCH Verlag, pp. 355-383, 2015.

[20] Johnson, B., and Mutharasan, R., "Biosensors," Ch. 16 of *Resonant MEMS. Fundamentals, Implementation and Application (Advanced Micro and Nanosystems, Vol. 11)*, Brand, O., Dufour, I., Heinrich, S. M., and Josse, F. (eds.), Wiley-VCH Verlag, pp. 391-419, 2015.

[21] Pister, K., and UC Berkeley "On the Limits and Applications of MEMS Sensor Networks," 2001.

[22] Shoaib, M., Hamid, N., Malik, A., Ali, N., and Jan, M., "A Review on Key Issues and Challenges in Devices Level MEMS Testing," *Journal of Sensors*, Vol. 2016, 2016.

[23] Rahafrooz, A., and Pourkamali, S., "Rotational Mode Disk Resonators for High-*Q* Operation in Liquid," *Sensors*, 2010 IEEE, Kona, HI, pp. 1071-1074, 2010.

[24] Rahafrooz, A., and Pourkamali, S., "Characterization of Rotational Mode Disk Resonator Quality Factors in Liquid," *IEEE International Frequency Control Symposium (IFCS).* San Francisco, CA, May 1-5, 5 pp., 2011.

[25] Hansma, P. K., Cleveland, J. P., Radmacher, M., Walter, D. A., Hillner, P. E., Bezanilla, M., Fritz, M., Vie, D., Hansma, H. G., Prater, C. B., Massie, J., Fukunaga, L., Gurley, J., and Elings, V., "Tapping Mode Atomic Force Microscopy in Liquids," *Applied Physics Letters,* Vol. 64, 1994.

[26] Putman, C. A. J., Van der Werf, K. O., De Grooth, B. G., Van Hulst, N. F., and Greve, J., "Tapping Mode Atomic Force Microscopy in Liquid," *Applied Physics Letters*, Vol. 64, 1994.

[27] Lantz, M. A., O'Shea, S. A., and Welland, M. E., "Force Microscopy Imaging in Liquids Using AC Techniques," *Applied Physics Letters*, Vol. 65, 1994.

[28] Walters, D. A., Cleveland, J. P., Thomson, N. H., Hansma, P. K., Wendman, M. A., Gurley, G., and Elings, V., “Short Cantilevers For Atomic Force Microscopy,” *Review of Scientific Instruments*, Vol. 67, 1996.

[29] Butt, H. J., Siedle, P., Seifert, K., Fendler, K., Seeger, T., Bamberg, E., Weisenhorn, A. L., Goldie, K., and Engel, A., “Scan Speed Limit in Atomic Force Microscopy,” *Journal of Microscopy,* Vol. 169, 1993.

[30] Chen, G. Y., Warmack, R. J., Thundat, T., Allison, D. P., and Huang, A., “Resonance Response Of Scanning Force Microscopy Cantilevers,” *Review of Scientific Instruments,* Vol. 65, 1994.

[31] Schäffer, T. E., Cleveland, J. P., Ohnesorge, F., Walters, D. A., and Hansma, P. K., “Studies of Vibrating Atomic Force Microscope Cantilevers in Liquid,” *Journal of Applied Physics*, Vol. 80, 1996.

[32] Sader, J. E., “Frequency Response Of Cantilever Beams Immersed in Viscous Fluids with Applications to the Atomic Force Microscope,” *Journal of Applied Physics,* Vol. 84, No. 1, pp. 64–76, 1998.

[33] Green, C., and Sader, J. E., “Frequency Response of Cantilever Beams Immersed in Viscous Fluids Near A Solid Surface with Applications to the Atomic Force Microscope,” *Journal of Applied Physics*, Vol 98, 2005.

[34] Goeders, K. M., Colton, J. S., and Bottomley, L. A., “Microcantilevers: Sensing Chemical Interactions Via Mechanical Motion,” *Chemical Reviews*, Vol. 108, No. 2, pp. 522–542, 2008.

[35] Boisen, A., Dohn, S., Keller, S. S., Schmid, S., and Tenje, M., “Cantilever-Like Micromechanical Sensors,” *Reports on Progress in Physics*., Vol. 74, No. 3, pp. 036101-1–036101-30, 2011.

[36] Eom, K., Park, H. S., Yoon, D. S., and Kwon, T., “Nanomechanical Resonators and Their Applications in Biological/Chemical Detection: Nanomechanics Principles,” *Physics Reports*, Vol. 503, Nos. 4–5, pp. 115–163, 2011.

[37] Zhu, Q., “Microcantilever Sensors in Biological and Chemical Detections,” *Sensors and Transducers*, Vol. 125, No. 2, pp. 1–21, 2011.

[38] Johnson, B. N., and Mutharasan, R., “Biosensing Using Dynamic-Mode Cantilever Sensors: A Review,” *Biosensors & Bioelectronics*, Vol. 32, No. 1, pp. 1–18, 2012.

[39] Belmiloud, N., Dufour, I., Colin, A., and Nicu, L., “Rheological Behavior Probed by Vibrating Microcantilevers,” *Applied Physics Letters*, Vol. 92, No. 4, pp. 041907-1–041907-3, 2008.

[40] Riesch, C., Reichel, E. K., Keplinger, F., and Jakoby, B., “Characterizing Vibrating Cantilevers for Liquid Viscosity and Density Sensing,” *Journal of. Sensors*, Vol. 2008, Aug. 2008, Art. ID 697062.

[41] Dufour, I., Maali, A., Amarouchene Y., Ayela, C., Caillard, B., Darwiche, A., Guirardel, M., Kellay, H., Mathieu, F., Pellet, C., Saya, D., Youssry, M., Nicu, L., and Colin, A., "The Microcantilever: A Versatile Tool for Measuring the Rheological Properties of Complex Fluids," *Journal of Sensors*, Vol. 2012, Aug. 2012, Art. ID 719898.

[42] Dufour, I., Lemaire, E., Caillard, B., Debeda, H., Lucat, C., Heinrich, S. M., Josse, F., and Brand, O., "Effect of Hydrodynamic Force on Microcantilever Vibrations: Applications to Liquid-Phase Chemical Sensing," *Sensors and Actuators B: Chemical*, Vol. 192, pp. 664–672, 2014.

[43] Zhao, L., Hu, Y., Wang, T., Ding, J., Liu, X., Zhao, Y., and Jiang, Z., "A MEMS Resonant Sensor to Measure Fluid Density and Viscosity under Flexural and Torsional Vibrating Mode," *Sensors*, Vol. 16(6):830, 2016.

[44] Reichel, E., Heinisch, M., and Jakoby, B., "Fluid Property Sensors," Ch. 17 of *Resonant MEMS. Fundamentals, Implementation and Application (Advanced Micro and Nanosystems, Vol. 11)*, Brand, O., Dufour, I., Heinrich, S. M., and Josse, F. (eds.), Wiley-VCH Verlag, pp. 427-446, 2015.

[45] Basak, S., Raman, A., and Garimella, S. V., "Hydrodynamic Loading of Microcantilevers Vibrating in Viscous Fluids," *Journal of Applied Physics*, Vol. 99, No. 11, pp. 114906-1–114906-10, 2006.

[46] Vančura, C., Li, Y., Lichtenberg, J., Kirstein, K. U., Hierlemann, A., and Josse, F., "Liquid-Phase Chemical and Biochemical Detection Using Fully Integrated Magnetically Actuated Complementary Metal Oxide Semiconductor Resonant Cantilever Sensor Systems," *Analytic Chemistry*, Vol. 79, No. 4, pp. 1646–1654, Feb. 2007.

[47] Vančura, C., Dufour, I., Heinrich, S. M., Josse, F., and Hierlemann, A., "Analysis of Resonating Microcantilevers Operating in A Viscous Liquid Environment," *Sensors and Actuators A: Physical*, Vol. 141, No. 1, pp. 43–51, 2008.

[48] Braun, T., Barwich, V., Ghatkesar, M. K., Bredekamp, A. H., Gerber, C., Hegner, M., and Lang, H. P., "Micromechanical Mass Sensors for Biomolecular Detection in A Physiological Environment," *Physical Review E*, Vol. 72, pp. 031907-1–031907-9, 2005.

[49] Van Eysden, C. A., and Sader, J. E., "Frequency Response of Cantilever Beams Immersed in Viscous Fluids with Applications to the Atomic Force Microscope: Arbitrary Mode Order," *Journal of Applied Physics*, Vol. 101, No. 4, pp. 044908-1–044908-11, 2007.

[50] Ghatkesar M. K., Barun, T., Barwich, V., Ramseyer, J. –P., Gerber, C., Hegner, M., and Lang, H. P., "Resonating Modes of Vibrating Microcantilevers in Liquid," *Applied Physics Letters*, Vol. 92, No. 4, pp. 043106-1–043106-3, 2008.

[51] Sharos, L. B., Raman, A., Crittenden, S., and Reifenberger, R., "Enhanced Mass Sensing Using Torsional and Lateral Resonances in Microcantilevers," *Applied Physics Letters*., Vol. 84, No. 23, pp. 4638–4640, 2004.

[52] Dufour, I., Heinrich, S. M., and Josse, F., "Theoretical Analysis of Strong-Axis Bending Mode Vibrations for Resonant Microcantilever (Bio)Chemical Sensors on Gas or Liquid Phase," *Journal of Microelectromechanical Systems*, Vol. 16, No. 1, pp. 44–49, 2007.

[53] Heinrich, S. M., Maharjan, R., Beardslee, L., Brand, O., Dufour, I., and Josse, F., "An Analytical Model for In-Plane Flexural Vibrations of Thin Cantilever-Based Sensors in Viscous Fluids: Applications to Chemical Sensing in Liquids," *Proceedings, International Workshop on Nanomechanical Cantilever Sensors*, Banff, Canada, May 26-28, 2 pp., 2010.

[54] Stokes, G. G., "On the Effect of the Internal Friction of fluids on the Motion of Pendulums," *Transactions of the Cambridge Philosophical Society*, Vol. 9, No. 2, pp. 8–106, 1851.

[55] Heinrich, S. M., Maharjan, R., Dufour, I., Josse, F., Beardslee, L. A., and Brand, O., "An Analytical Model of a Thermally Excited Microcantilever Vibrating Laterally in a Viscous Fluid," *Proceedings and Poster Session, IEEE Sensors 2010 Conference*, Waikoloa, Hawaii, November 1-4, pp. 1399-1404, 2010.

[56] Beardslee, L. A., Addous, A. M., Heinrich, S. M., Josse, F., Dufour, I., and Brand, O., "Thermal Excitation and Piezoresistive Detection of Cantilever In-Plane Resonance Modes for Sensing Applications," *Journal of Microelectromechanical System*, Vol. 19, No. 4, 2010.

[57] Beardslee, L. A., Josse, F., Heinrich, S. M., Dufour, I., and Brand, O., "Geometrical Considerations for the Design of Liquid-Phase Biochemical Sensors Using A Cantilever's Fundamental In-Plane Mode," *Sensors and Actuators B: Chemical*, Vol. 164, 2012.

[58] Dufour, I., Josse, F., Heinrich, S. M., Lucat, C., Ayela, C., Menil, F., and Brand, O., "Unconventional Uses of Microcantilevers as Chemical Sensors in Gas And Liquid Media," *Sensors and Actuators B: Chemical*, Vol. 170, pp. 115–121, 2012.

[59] Cox, R., Josse, F., Heinrich, S. M., Brand, O., and Dufour, I., "Characteristics of Laterally Vibrating Resonant Microcantilevers in Viscous Liquid Media," *Journal of Applied Physics*, Vol. 111, No. 1, pp. 014907-1–014907-14, 2012.

[60] Cox, R., Josse, F., Heinrich, S. M., Dufour, I., and Brand, O., "Resonant Microcantilevers Vibrating Laterally in Viscous Liquid Media," *IEEE International Frequency Control Symposium*, pp. 85-90, Newport Beach, CA, 1-4 June, 2010.

[61] Schultz, J. A., Heinrich, S. M., Josse, F., Dufour, I., Nigro, N. J., Beardslee, L. A., and Brand, O., "Lateral-Mode Vibration of Microcantilever-based Sensors in

Viscous Fluids Using Timoshenko Beam Theory," *Journal of Microelectromechanical Systems*, Vol. 24, No. 4, 2015.

[62] Schultz, J. A., Heinrich, S. M., Josse, F., Nigro, N. J., Dufour, I., Beardslee, L. A., and Brand, O., "Timoshenko Beam Effects in Lateral-Mode Microcantilever-Based Sensors in Liquids," *Micro & Nano Letters*, Vol. 8, No. 11, 2013.

[63] Schultz, J. A., Heinrich, S. M., Josse, F., Nigro, N. J., Dufour, I., Beardslee, L. A., and Brand, O., "Timoshenko Beam Effects in Lateral-Mode Microcantilever-Based Sensors in Liquids," *Proceedings of 2013 Nanomechanical Sensing Workshop*, 2013.

[64] Schultz, J. A., Heinrich, S. M., Josse, F., Dufour, I., Nigro, N. J., Beardslee, L. A., and Brand, O., "Timoshenko Beam Model for Lateral Vibration of Liquid-Phase Microcantilever-based Sensors," *Proc., 14th International Symposium on MEMS and Nanotechnology, SEM*, 2013.

[65] Lakhmi, R., Debeda, H., Dufour, I., Lucat, C., and Maglione, M., "Study of Screen-Printed PZT Cantilevers Both Self-Actuated and Self-Read-Out," *International Journal of Applied Ceramic Technology*, Vol. 11, No. 2, pp. 311–320, 2014.

[66] Castille, C., Dufour, I., and Lucat, C., "Longitudinal Vibration Mode of Piezoelectric Thick-Film Cantilever-Based Sensors In Liquid Media," *Applied Physics Letters*, Vol. 96, No. 15, pp. 154102-1–154102-3, 2010.

[67] Johnson, B. N., and Mutharasan, R., "Persistence of Bending and Torsional Modes in Piezoelectric-Excited Millimeter-Sized Cantilever (PEMC) Sensors in Viscous Liquids — 1 to 103 cP," *Journal of Applied Physics*, Vol. 109, No. 6, pp. 066105-1–066105-3, 2011.

[68] Green, C. P., and Sader, J. E., "Torsional Frequency Response of Cantilever Beams Immersed in Viscous fluids with Applications to the Atomic Force Microscope," *Journal of Applied Physics*, Vol. 92, No. 10, pp. 6262–6274, 2002.

[69] Aureli, M., Pagano, C., and Porfiri, M., "Nonlinear Finite Amplitude Torsional Vibrations of Cantilevers in Viscous Fluids," *Journal of Applied Physics*, Vol. 111, No. 12, pp. 124915-1–124915-16, 2012.

[70] Cai, T., Josse, F., Heinrich, S. M., Nigro, N., Dufour, I., and Brand, O., "Resonant Characteristics of Rectangular Microcantilevers Vibrating Torsionally in Viscous Liquid Media," *Proc., IEEE International Frequency Control Symposium,* Baltimore, MD, May 21-24, pp. 807-812, 2012.

[71] Linden, J., and Oesterschulze, E., "Improving the Quality Factor of Cantilevers in Viscous Fluids by the Adaptation of Their Interface," *Applied Physics Letters*, Vol. 100, No. 11, pp. 113511-1–113511-3, 2012.

[72] Burg, T. P., and Manalis, S. R., "Suspended Microchannel Resonators for Biomolecular Detection," *Applied Physics Letters*, Vol. 83, No. 2698, 2003.

[73] Burg, T. P., Mirza, A. R., Milovic, N., Tsau, C. H., Popescu, G. A., Foster, J. S., and Manalis, S. R., "Vacuum-Packaged Suspended Microchannel Resonant Mass Sensor for Biomolecular Detection," *Journal of Microelectromechanical Systems*, Vol. 15, No. 6, 2006.

[74] Burg, T. P., Godin, M., Knudsen, S. M., Shen, W., Carlson, G., Foster, J. S., Babcock, K., and Manalis, S. R., "Weighing of Biomolecules, Single Cells and Single Nanoparticles in Fluid," *Nature*, Vol. 446, pp. 1066-1069, 2007.

[75] Sader, J. E., Burg, T. P., and Manalis, S. R., "Energy Dissipation in Microfluidic Beam Resonators," *Journal of Fluid Mechanics*, Vol. 650, pp. 215–250, 2010.

[76] Seo, J. H., and Brand, O., "High *Q*-factor In-Plane-Mode Resonant Microsensor Platform for Gaseous/Liquid Environment," *Journal of Microelectromechanical Systems*, Vol. 17, No. 2, pp. 483–493, 2008.

[77] Waggoner, P. S., Tan, C. P., Bellan, L., and Craighead, H. G., "High-*Q*, In-Plane Modes of Nanomechanical Resonators Operated in Air," *Journal of Applied Physics*, Vol. 105, No. 9, pp. 094315-1–094315-6, 2009.

[78] Linden, J., Thyssen, A., and Oesterschulze, E., "Suspended Plate Microresonators with High Quality Factor for the Operation in Liquids," *Applied Physics Letters*, Vol. 104, No. 19, pp. 191906-1–191906-3, 2014.

[79] Rahafrooz, A., Hajjam, A., Tousifar, B., and Pourkamali, S., "Thermal Actuation, A Suitable Mechanism for High Frequency Electromechanical Resonators," *Proc. IEEE 23rd Int. Conf. MEMS,* Hong Kong, pp. 200–203. 2010.

[80] Rahafrooz, A., and Pourkamali, S., "Thermo-electro-mechanical Modeling of High Frequency Thermally Actuated I^2-BAR Resonators," *Tech. Dig. Solid-State, Sens., Actuators, Microsyst. Workshop,* Hilton Head Island, SC, USA, pp. 74–77, 2010.

[81] Brand, O., and Pourkamali, S., "Electrothermal Excitation of Resonant MEMS," Ch. 8 of *Resonant MEMS. Fundamentals, Implementation and Application (Advanced Micro and Nanosystems, Vol. 11),* Brand, O., Dufour, I., Heinrich, S. M., and Josse, F. (eds.), Wiley-VCH Verlag, pp. 173-199, 2015.

[82] Mehdizadeh, E., Chapin, J., Gonzales, J., Rahafrooz, A., Abdolvand, R., Purse, B., and Pourkamali, S., "Direct Detection of Biomolecules in Liquid Media Using Piezoelectric Rotational Mode Disk Resonators," *Sensors IEEE Int. Conf.*, pp. 1-4, 2012.

[83] Mehdizadeh, E., Gonzales, J., Rahafrooz, A., Abdolvand, R., and Pourkamali, S., "Piezoelectric Rotational Mode Disk Resonators for Liquid Viscosity Monitoring," *Tech. Dig. Hilton Head Workshop,* pp. 359-362, 2012.

[84] Mehdizadeh, E., Rostami, M., Guo, X., and Pourkamali, S., "Atomic Resolution Disk Resonant Force and Displacement Sensors for Measurements in Liquid," *Electron Device Letters*, Vol. 35, No. 8, pp. 874-876, 2014.

[85] Sotoudegan, M. S., Heinrich, S. M., Josse, F., Nigro, N. J., Dufour, I., and Brand, O., "A Simple Model for the In-Plane Rotational Response of a Disk Resonator in Liquid: Resonant Frequency, Quality Factor, and Optimal Geometry," *Proceedings and Poster Session, International Workshop on Nanomechanical Sensing (NMC 2013),* pp. 107-108, Stanford, CA, May 1-3, 2013,

[86] Sotoudegan, M. S., Heinrich, S. M., Josse, F., Nigro, N. J., Dufour, I., and Brand, O., "Effect of Design Parameters on the Rotational Response of a Novel Disk Resonator for Liquid-Phase Sensing: Analytical Results," *Proc., IEEE Sensors 2013 Conference,* pp. 1164-1167, Baltimore, MD, November 4-6, 2013.

[87] Beer, F. P., Johnston, E. R., DeWolf, J. T., and Mazurek, D. F., *Mechanics of Materials*, McGraw-Hill Education, New York, NY, 2015.

[88] Sotoudegan, M. S., Heinrich, S. M., Josse, F., Dufour, I., and Brand, O., "A Multi-Modal Continuous-Systems Model of a Novel High-*Q* Disk Resonator in a Viscous Liquid," *Proceedings, International Workshop on Nanomechanical Sensing (NMC 2014),* pp. 98-99, Madrid, Spain, April 30 – May 2, 2014.

[89] Sotoudegan, M. S., Heinrich, S. M., Josse, F., Nigro, N. J., Dufour, I., and Brand, O., "Analytical Modeling of a Novel High-*Q* Disk Resonator for Liquid-Phase Applications," *Journal of Microelectromechanical Systems*, Vol. 24, No. 1, pp. 38-49, 2015.

[90] Heinrich, S. M., and Dufour, I., "Fundamental Theory of Resonant MEMS devices," Ch. 1 of *Resonant MEMS. Fundamentals, Implementation and Application (Advanced Micro and Nanosystems, Vol. 11)*, Brand, O., Dufour, I., Heinrich, S. M., and Josse, F. (eds.), Wiley-VCH Verlag, pp. 3-27, 2015.

[91] Clough, R. W., and Penzien, J., *Dynamics of Structures*, 2nd Ed. New York, NY, USA: McGraw-Hill, 1993.

[92] Lange, D., Hagleitner, C., Hierlemann, A., Brand, O., and Baltes, H., "Complementary Metal Oxide Semiconductor Cantilever Arrays on a Single Chip: Mass-Sensitive Detection of Volatile Organic Compounds," *Analytic Chemistry,* Vol 74, No. 13, pp. 3084–3095, 2002.

[93] Waggoner, P. S., and Craighead, H. G., "Micro- and Nanomechanical Sensors for Environmental, Chemical, and Biological Detection," *Lab on a Chip,* Vol. 7, pp. 1238-1255, 2007.

[94] Hagleitner, C., Lange, D., Hierlemann, A., Brand, O., and Baltes, H., "CMOS Single-Chip Gas Detection System Comprising Capacitive, Calorimetric and Mass-Sensitive Microsensors," *IEEE Journal of Solid-State Circuits,* Vol. 37, No. 12, 2002.

APPENDIX A:

DERIVATION OF β_{cr} AND PEAK $\delta_n/\omega_{n,vac}$ VALUE FOR AXIAL-MODE CANTILEVER (NO-DISK CASE)

Taking the derivative of (4-45) with respect to β and setting it equal to zero yields

$$\frac{d\bar{\delta}_n}{d\beta} = 0 \rightarrow \; (\bar{\varpi}_n)_{cr}{}^{3/2} + \left[\frac{1}{2}\beta_{cr}\sqrt{(\bar{\varpi}_n)_{cr}} + \beta_{cr}{}^{2}\right](\bar{\varpi}_n)_{cr}{}' = 0 \tag{A-1}$$

where $(\bar{\varpi}_n)_{cr}$ is the damped natural frequency of an axial-mode cantilever at the critical value of the fluid resistance parameter, β_{cr}, the latter being defined as the value at which $\bar{\delta}_n$ is stationary. The general expression for $\bar{\varpi}_n{}'$ (the prime denoting differentiation with respect to β) as a function of $\bar{\varpi}_n$ and β may be derived by taking the derivative of (4-46) with respect to β:

$$\bar{\varpi}_n{}' = -\frac{4\bar{\varpi}_n{}^{5/2} + 10\beta\bar{\varpi}_n{}^{2} + 5\beta^2\bar{\varpi}_n{}^{3/2}}{8\bar{\varpi}_n{}^{2} + 22\beta\bar{\varpi}_n{}^{3/2} + 21\beta^2\bar{\varpi}_n + \frac{15}{2}\beta^3\sqrt{\bar{\varpi}_n}} \tag{A-2}$$

Equation (A-2) is true for any β value including β_{cr} ; therefore,

$$(\bar{\varpi}_n)_{cr}{}' = -\frac{4(\bar{\varpi}_n)_{cr}{}^{5/2} + 10\beta_{cr}(\bar{\varpi}_n)_{cr}{}^{2} + 5\beta_{cr}{}^{2}(\bar{\varpi}_n)_{cr}{}^{3/2}}{8(\bar{\varpi}_n)_{cr}{}^{2} + 22\beta_{cr}(\bar{\varpi}_n)_{cr}{}^{3/2} + 21\beta_{cr}{}^{2}(\bar{\varpi}_n)_{cr} + \frac{15}{2}\beta_{cr}{}^{3}\sqrt{(\bar{\varpi}_n)_{cr}}} \tag{A-3}$$

Substituting (A-3) into (A-1) results in the following 4th-degree polynomial equation:

$$8\left(\frac{\sqrt{(\bar{\omega}_n)_{cr}}}{\beta_{cr}}\right)^4+20\left(\frac{\sqrt{(\bar{\omega}_n)_{cr}}}{\beta_{cr}}\right)^3+12\left(\frac{\sqrt{(\bar{\omega}_n)_{cr}}}{\beta_{cr}}\right)^2-5\left(\frac{\sqrt{(\bar{\omega}_n)_{cr}}}{\beta_{cr}}\right)-5=0 \qquad \text{(A-4)}$$

The analytical solution of (A-4) shows that, of all the four roots, one root is real and positive while the other three roots have either negative or complex values. Recalling that the frequency is related to the added fluid mass coefficient (see the derivation of the Stokes-type fluid resistance forces in Sect. 3.3.2) and β has a positive real value, the only valid root is the positive real root given by

$$(\bar{\omega}_n)_{cr}=\left(\sqrt{(\bar{\omega}_n)_{cr}}\right)^2=\left(K-\frac{1}{2}+\frac{1}{4K}\right)^2\beta_{cr}{}^2=0.3046\beta_{cr}{}^2 \qquad \text{(A-5)}$$

in which $K=\left(\frac{\sqrt{5}+3}{16}\right)^{1/3}=0.6891$. Finally, substituting (A-5) into (4-46) yields the critical value of β for an arbitrary mode *n*:

$$\left(\beta_{cr}\right)_n=\frac{4K}{4K^2-2K+1}\left[\frac{\left(4K^2+1\right)^2-4K^2}{\left(4K^2+2K+1\right)^2+4K^2}\right]^{1/4}\sqrt{2n-1}=1.3651\sqrt{2n-1} \qquad \text{(A-6)}$$

The corresponding value (peak value) of $\frac{\delta_n}{\omega_{n,vac}}$ can then be calculated by substituting (A-5) and (A-6) into (4-45) to yield

$$\left.\frac{\delta_n}{\omega_{n,vac}}\right|_{max}=\frac{2K}{4K^2+2K+1}\sqrt{\frac{\left(4K^2+1\right)^2-4K^2}{\left(4K^2+2K+1\right)^2+4K^2}}=0.1829 \qquad \text{(A-7)}$$

Since the quality factor is (inversely) related to the damping ratio of the system which itself is a function of the δ_n/ω_n ratio, the functional dependence of the fluid resistance parameter upon this ratio will enable us to evaluate the quality factor of the cantilever as β theoretically approaches infinity. From (4-45) and (4-46) one may derive the following relationship between β and the ratio of the decay parameter to the damped natural frequency, δ_n/ω_n:

$$\beta = \sqrt{2n-1}\,\frac{2\delta_n/\omega_n}{\left(1-2\delta_n/\omega_n\right)^{3/4}\left[1+\left(\delta_n/\omega_n\right)^2\right]^{1/4}} \tag{A-8}$$

This equation implies that when $\beta \to \infty$, the value of δ_n/ω_n ratio is ½ ; thus, it follows from (4-18) that Q for the axial-mode cantilever has a constant, non-zero, minimum value given by $\sqrt{5}/2 = 1.118$ corresponding to the $\beta \to \infty$ limit for an arbitrary mode n. (See Fig. 5-10.)

By using (A-8), one may determine the peak value of $\dfrac{\delta_n}{\omega_{n,vac}}$ by an alternative way in which the damped natural frequency and the decay parameter are expressed in terms of δ_n/ω_n:

$$\frac{\omega_n}{\omega_{n,vac}} = \sqrt{\frac{1-2\delta_n/\omega_n}{1+\left(\delta_n/\omega_n\right)^2}} \tag{A-9}$$

$$\frac{\delta_n}{\omega_{n,vac}} = \frac{\delta_n}{\omega_n}\frac{\omega_n}{\omega_{n,vac}} = \frac{\delta_n}{\omega_n}\sqrt{\frac{1-2\delta_n/\omega_n}{1+\left(\delta_n/\omega_n\right)^2}} \tag{A-10}$$

Taking the derivative of (A-10) with respect to β and setting it equal to zero leads to the following cubic equation:

$$\frac{d}{d\beta}\left(\frac{\delta_n}{\omega_{n,vac}}\right)=0 \quad \rightarrow \quad \left(\delta_n/\omega_n\right)^3+3\left(\delta_n/\omega_n\right)-1=0 \qquad \text{(A-11)}$$

The only real root of (A-11) is

$$(\delta_n/\omega_n)_{cr}=\left(\frac{\sqrt{5}+1}{2}\right)^{1/3}-\frac{1}{\left(\frac{\sqrt{5}+1}{2}\right)^{\frac{1}{3}}}=0.3222 \qquad \text{(A-12)}$$

Substituting (A-12) into (A-8) and (A-10) will give the same results for the critical values of β and the peak value of $\frac{\delta_n}{\omega_{n,vac}}$.